

A STUDY OF LONG-OFFSET SEISMIC IMAGING  
WITH AN UPGRADED PHYSICAL MODELING SYSTEM

.....  
A Thesis  
Presented to  
the Faculty of the Department of Geosciences  
University of Houston

.....  
In Partial Fulfillment  
of the Requirements for the Degree  
Master of Science

.....  
By  
Qingliang Lin  
May 2003

A STUDY OF LONG-OFFSET SEISMIC IMAGING  
WITH AN UPGRADED PHYSICAL MODELING SYSTEM

-----  
Qingliang Lin

APPROVED:

-----  
Dr. Hua-wei Zhou, Chairman

-----  
Dr. Kurt J. Marfurt

-----  
Dr. Hongwei Wang

-----  
Dean, College of Natural Sciences and Mathematics

## ACKNOWLEDGMENTS

It is a great pleasure for me to express my sincere gratitude to the faculty, students and sponsors of AGL. I am immensely privileged to have the supervision of Dr. Kurt J. Marfurt and direct guidance of Dr. Hua-wei Zhou. I am greatly indebted to them for their encouragement, guidance, help, and friendship throughout this endeavor. I am grateful to Dr. Robert Wiley for his enlightening suggestions and guidance in LabVIEW software development; Dr. Hongwei Wang who is always available for help beyond the call of duty. My special thanks and appreciations go to Dr. Kwangjin Yoon and Anning Hou for providing imaging algorithms and assistance. I would like to thank all my colleagues and friends at the University of Houston for their friendship and support. I am also grateful to my wife and my daughter for their love and support in my attainment of this goal.

A STUDY OF LONG-OFFSET SEISMIC IMAGING  
WITH AN UPGRADED PHYSICAL MODELING SYSTEM

.....

An Abstract of a Thesis  
Presented to  
the Faculty of the Department of Geosciences  
University of Houston

.....

In Partial Fulfillment  
of the Requirements for the Degree  
Master of Science

.....

By  
Qingliang Lin  
May 2003

## ABSTRACT

Long-offset seismic data are those acquired with source-receiver offset greater than the depth to the imaging targets. Such data illuminate the subsurface differently from conventional short-offset data and therefore contain additional information about the earth. However, the usage of long-offset data also brings additional challenges for processing and imaging. The main objective of my thesis is to analyze issues associated with long-offset seismic imaging. Specifically it is recognized that a satisfactory imaging of the long-offset data requires the use of pre-stack depth migration, where the accurate velocity model estimation becomes particularly important.

Seismic physical modeling is useful for studying basic imaging problems with a known answer. To address my thesis objective, I designed and implemented a new LabVIEW seismic physical modeling system, and used it to simulate Vibroseis data acquisition and acquire some long-offset physical modeling data. Different seismic modeling techniques were also applied to generate the synthetic data for comparison and imaging processing. I found that it is possible to obtain turning wave data from both horizontal and vertical boundaries in a layered physical model. Clearly, the new physical modeling system that I build will be useful to many other applications beyond my thesis work.

Estimation of the velocity model for long-offset data is still a challenge issue in many applications. I tested a deformable layer tomography algorithm with a field long-offset data and obtained a reasonable result. To compare the migrations of the long-offset and near-offset data, I applied a reverse-time pre-stack depth migration to the physical model dataset. The images from the far-offset and near-offset traces show some interesting differences. Though the long-offset image is noisier and has poorer resolution of the horizontal boundaries, it provides improved illumination of the vertical boundaries. With some pre-conditioning of the raw data, reverse-time pre-stack depth migration with full-offset data gave a better image.

## CONTENTS

1. INTRODUCTION.....	1
1.1 Long-offset seismic data .....	1
1.1.1 Non-hyperbolic moveout.....	3
1.1.2 NMO induced artifacts .....	4
1.1.3 High sensitivity to velocity model .....	5
1.1.4 Mode-converted waves.....	6
1.1.5 Amplitude issue.....	7
1.2 Objectives of the thesis .....	8
1.3 Review of imaging methods for long-offset data .....	9
1.4 Organization of the chapters.....	16
2. MODELING OF LONG-OFFSET SEISMIC DATA.....	18
2.1 A new LabVIEW-based physical modeling system .....	18
2.1.1 Hardware configuration.....	18
2.1.2 Flow charts of the major programs .....	20
2.1.3 Subroutine hierarchy .....	24
2.1.4 Interfaces.....	26
2.1.5 Functions.....	28
2.1.6 Performance test.....	28
2.1.6.1 Effect of the transducers movement on data quality .....	28

2.1.6.2 Timing test .....	30
2.2 Modeling of long-offset seismic data .....	31
2.1.1 Turning wave physical modeling .....	31
2.2.2 Wide-aperture physical modeling .....	36
2.2.3 Crosswell physical modeling .....	39
2.3 ‘Vibroseis’ source simulation.....	42
2.4 Comparison of physical modeling with ray theoretical modeling.....	46
3. FIRST ARRIVAL TOMOGRAPHY WITH DEFORMABLE LAYERS .....	49
3.1 Methodology.....	49
3.2 Apply to 2-D crooked line field data .....	58
3.2.1 Data set .....	58
3.2.2 First arrival picks.....	60
3.2.3 Crooked line geometry rebinning.....	60
3.2.4 Reference velocity model .....	61
3.2.5 Data QC for accuracy and consistency.....	62
3.2.6 DLT .....	63
4. MIGRATION OF PHYSICAL MODELING DATA .....	67
4.1 Data pre-processing .....	67
4.1.1 Deterministic deconvolution.....	67
4.1.2 T-p filtering.....	70
4.2 Kirchhoff pre-stack depth migration.....	72

4.3 Reverse-time pre-stack depth migration .....	75
5 CONCLUSIONS .....	83
REFERENCES .....	86
Appendix A AGL NEW LABVIEW-BASED PHYSICAL MODELING SYSTEM	
— USER MANUAL .....	92
A.1 The ‘Start here’ panel.....	92
A.2 The ‘Select survey’ panel .....	97
A.3 The ‘Define Signal ’ panel .....	97
A.4 The modeling operation .....	98
A.5 The acquired data.....	99
Appendix B SOURCE SIGNATURE AND ACOUSTIC FIELD OF PHYSICAL	
MODELING .....	100
B.1 The transducer .....	100
B.2 The signature.....	101
B.3 Transducers directivity.....	104
B.4 Minimize ambient noise .....	105
Appendix C METHODS TO IMPROVE DATA ACQUISITION QUALITY.....	
C.1 ‘Mouse pad’ to degrade the direct energy .....	107
C.2 Effect of source depth on spherical transducer .....	109

## INTRODUCTION

### 1.1 Long-offset seismic data

Long-offset seismic data are typically considered to be those acquired with source-receiver offset greater than the depth to the targets. Many modern seismic acquisition strategies with fixed receiver positions, such as Ocean Bottom Cable (OBC), vertical cable and reverse VSP, all have considerable long-offset components. Unfortunately, in the common mid-point (CMP) framework, due to factors such as excessive normal moveout (NMO) stretch, non-hyperbolic moveout, and waveform distortion around and beyond the critical angle, much of the long-offset data have to be deleted during the conventional NMO stretch mute process. For OBC data, for instance, as much as two thirds of the data is long-offset and therefore could be thrown away.

Nevertheless, long-offset data illuminate the earth differently from the near-offset data and therefore contain additional information about the earth's subsurface. In imaging steeply dipping geologic features such as salt flanks, fault planes and over-turned layers, useful reflections may arrive at relatively large offset. Imaging the sub-salt and sub-basalt reflectors demands long-offset data. Obtaining sufficient offset coverage for the AVO analysis also requires long-offset data. For land data, the near-offset portion

of seismic data is often strongly contaminated by ground-rolls, while the long-offset reflections could arrive beyond the ground-rolls (Figure 1.1). In addition, the near-surface contamination is greater at near-offset than at far-offset because seismic rays are nearly vertical at far-offset.

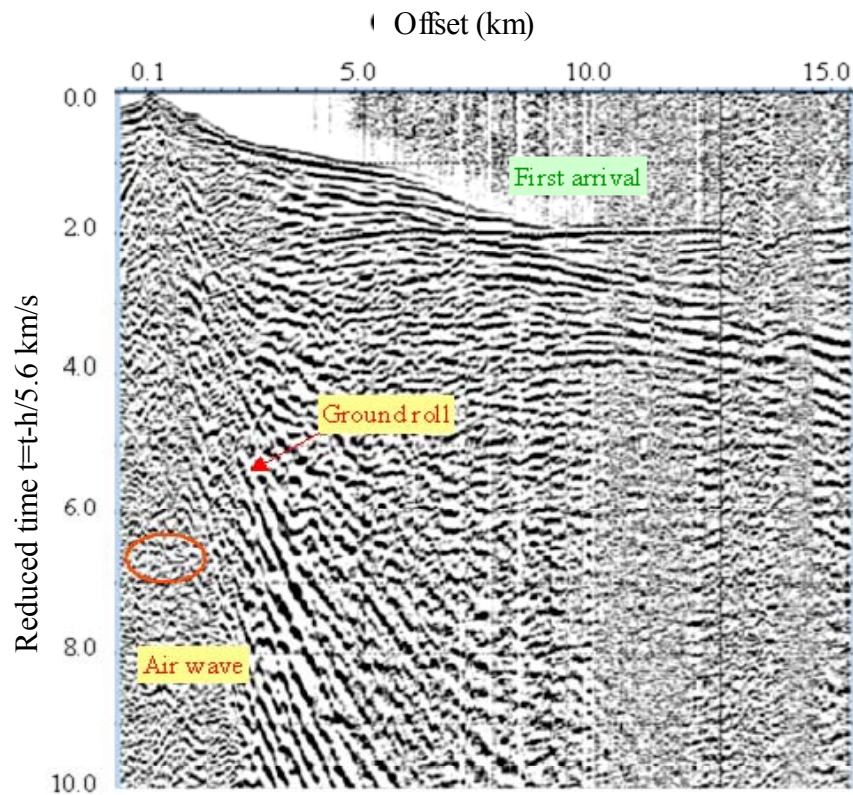


FIG. 1.1. Shot gather from Tarim basin, China. Traveltime is reduced at 5.6 km/s. The near-offsets are contaminated with ground roll and air wave, but at the far-offset the first arrival events are clearly shown.

While the long-offset data are capable of solving for special exploration problems, they also bring in additional challenges to the processing and imaging efforts.

### 1.1.1 Non-hyperbolic moveout

In the CMP framework, the stacking velocities are obtained from analyzing the CMP gathers, based on an expanded series of the traveltimes equation (Taner *et al*, 1969):

$$T^2(x) = c_0 + c_1x^2 + c_2x^4 + \dots \quad , \quad (1.1)$$

where  $T(x)$  is traveltimes at offset  $x$ ,  $c_0$  is the zero-offset traveltimes,  $c_1 = 1/v_{rms}^2$  (root-mean-square velocity),  $c_2$  and  $c_3$  are complicated functions of the layers thickness and interval velocity. When offset is small with respect to the depth to the targets, the data may be fit well with the first two terms.

$$T^2(x) = t^2(0) + x^2 / v_{rms}^2 \quad (1.2)$$

This is the so-called hyperbolic equation that is commonly used in semblance velocity analysis. However, as offset increases, the higher order terms of equation (1) become significant and need to be included in the velocity analysis. Several different schemes have been proposed to improve the accuracy of velocity analysis, such as corrections using higher order terms of equation (1), corrections for raypaths bending effect and

for transverse anisotropy (Figure 1. 2). Nevertheless, the limited offset remains to be an issue in providing accurate velocity analysis.

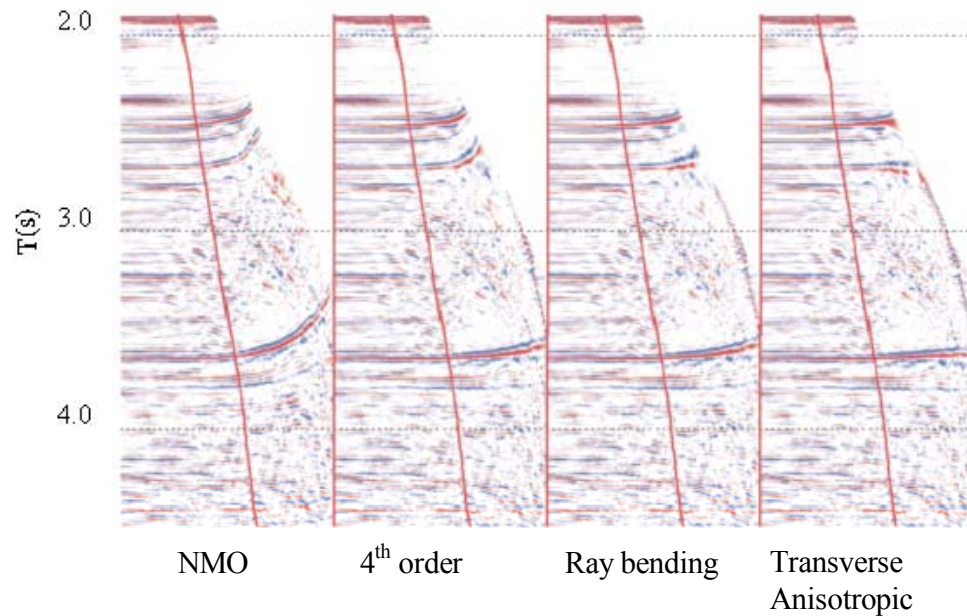


FIG. 1.2. Comparison of moveout collection methods (Dutta, 2002). The differences are only noticeable at the far-offsets. Transverse anisotropic correction results in a model that is closest to the correct one.

### 1.1.2 NMO induced artifacts

The NMO induced artifacts, such as stretches of the shallow and far-offset events and frequency distortion, crossover with deeper events in far-offset data (Figure 1.3), will degrade the subsequent imaging and stacking processing. Inaccuracy in shallow parts

of the model will result in deviation of the raypaths and introduce larger errors in both raypath and traveltimes calculations. It is a common practice to apply an “outer mute” to delete the shallow far-offset data in conventional data processing, thereby eliminating the long-offset data.

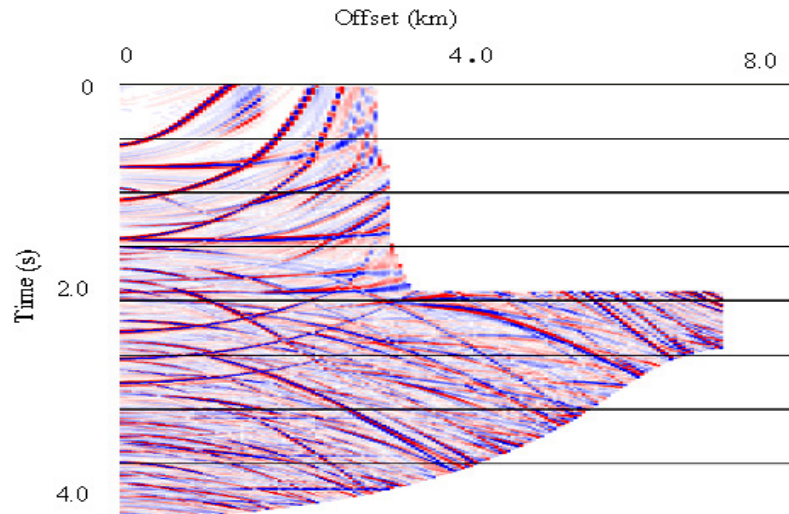


FIG. 1.3. A CMP gather from elastic modeling. The PS-wave NMO and muting was applied due to NMO induced artifacts (after Sun *et al*, 2002).

### 1.1.3 High sensitivity to velocity model

The waves of the long-offset data traverse more sub-horizontally as compared with that of the near-offset data. Hence for a target of the same depth, raypaths of long-offset data are longer than that of the near-offset data. If the velocity field varies both

horizontally and vertically, as in most real cases, the long-offset data will be more dependent on the velocity model. This means that, with respect to the near-offset data, the long-offset data are more sensitive to the errors in the velocity model. Therefore, the accurate velocity model estimation becomes particularly important.

### 1.1.4 Mode-converted waves

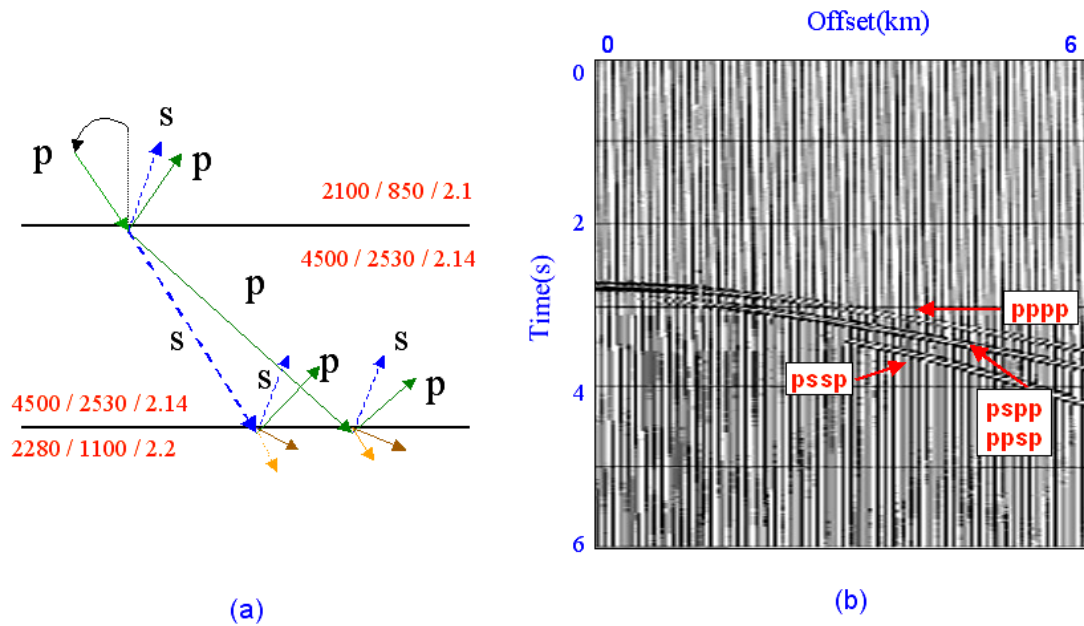


FIG. 1.4. A 3-layer model (a) and reflections from the 2<sup>nd</sup> interface (b) ( $V_{p2}=4.5$  km/s,  $V_{s2}=2.53$  km/s,  $\rho_2=2.14$  g/cm<sup>3</sup> and  $V_{p3}=2.28$  km/s,  $V_{s3}=1.1$  km/s,  $\rho_3=2.2$  g/cm<sup>3</sup>) (Ogilvie, 1996). Note that the mode-converted waves (PSSP, PSPP or PPSP) become significant as offset increases.

As offset increases, waves of different modes come into play, and the mode-converted waves that are generally considered negligible in conventional data processing become significant (Figure 1.4). It may hinder the correct imaging when neglected.

**1.1.5 Amplitude issue**

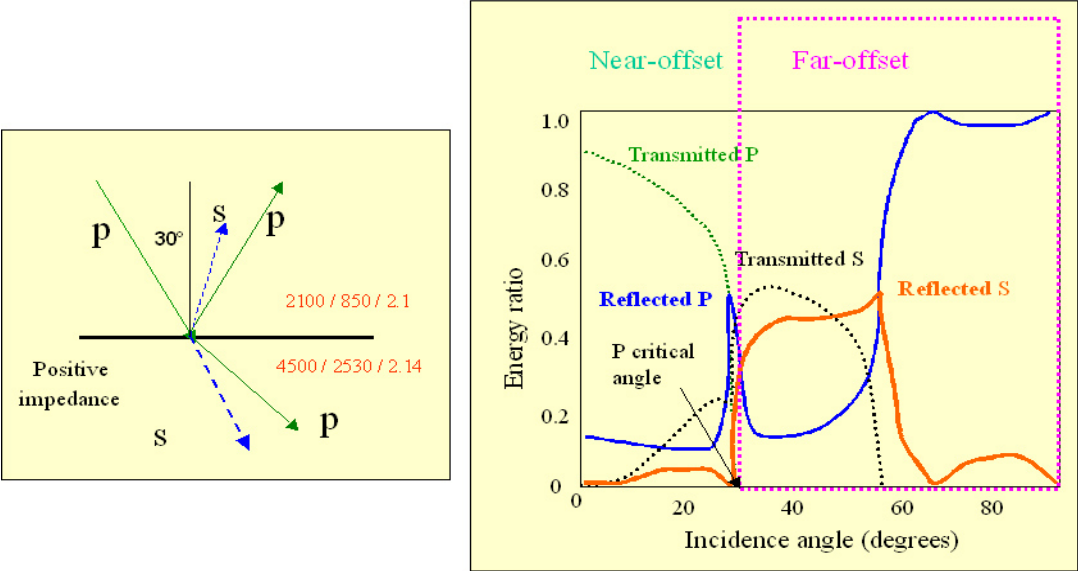


FIG. 1.5. Energy partition for *P*-wave incidence on a positive impedance interface (after Ogilvie, 1996). ( $V_{p1}=2100$  km/s,  $V_{s1}=850$  km/s,  $\rho_1=2.1$  g/cm<sup>3</sup> and  $V_{p2}=4.5$  km/s,  $V_{s2}=2530$  km/s,  $\rho_2=2.14$  g/cm<sup>3</sup>). Left panel shows raypath diagram. Right panel shows reflective energy versus incidence angles for the reflected and transmitted *P* and *S* waves.

According to the energy partition prediction on a interface using the Zoeppritz equation, around and beyond the critical angle, the amplitude versus offset relation becomes much more complicated. The percentage of energy (Figure 1.5) reflected from a positive impedance interface increases compared to the energy transmitted through the interface, and a substantial amount of the *P-S* conversion occurs. Hence it would be more difficult to apply semblance velocity analysis to far-offset data.

## **1.2 Objectives of the thesis**

The major objective of my thesis is to analyze long-offset data for seismic imaging. Specifically I intended to verify in concept some processing and imaging methods, which are useful for long-offset data, including the deformable layer tomography (DLT) for velocity estimation and pre-stack depth migration. A unique aspect of my work is the use of physical modeling for acquiring long-offset data. Another objective of this work is to design and implement a new LabVIEW-based physical modeling system, and use it to acquire long-offset data and improve the data quality.

### 1.3 Review of imaging methods for long-offset data

Seismic imaging generally consists of two steps: estimation of velocity model depicting the slowly varying earth properties, and migration of reflections from the interfaces corresponding to high-frequency variation of impedance. As the offset increases the moveout becomes increasingly non-hyperbolic. Hence the NMO approximation, which is the core of traditional reflection imaging, is no longer suitable. Many authors have proposed other schemes to improve the conventional NMO. For instance, Taner and Koehler (1969) and Al-Chalabi (1973) made a fourth order correction by using a three terms Taylor series expansion. Using more than two terms in the Taylor series can improve velocity analysis and CMP stacking. To have a traveltimes approximation with good accuracy at large offsets, Sun *et al* (2002) developed an optimized 6<sup>th</sup> order long-offset NMO correction. The definition and the coefficients for the first three terms are the same as that given by Taner and Koehler (1969). But the coefficient for the fourth term is modified to make the traveltimes error smaller (Figure 1.6).

Attempts to improve the accuracy of non-hyperbolic equation have also introduced anisotropy. Thomsen (1986) showed that the observed moveout velocity for a homogeneous, vertical transverse isotropic (VTI) anisotropy medium would be the vertical velocity of seismic waves in the medium scaled with an anisotropic factor:

$$V_{nmo} = V_{po} \sqrt{1 + 2\delta} \quad , \quad (1.3)$$

where the short-spread NMO velocity (interval velocity for imaging)  $V_{nmo}$  can be

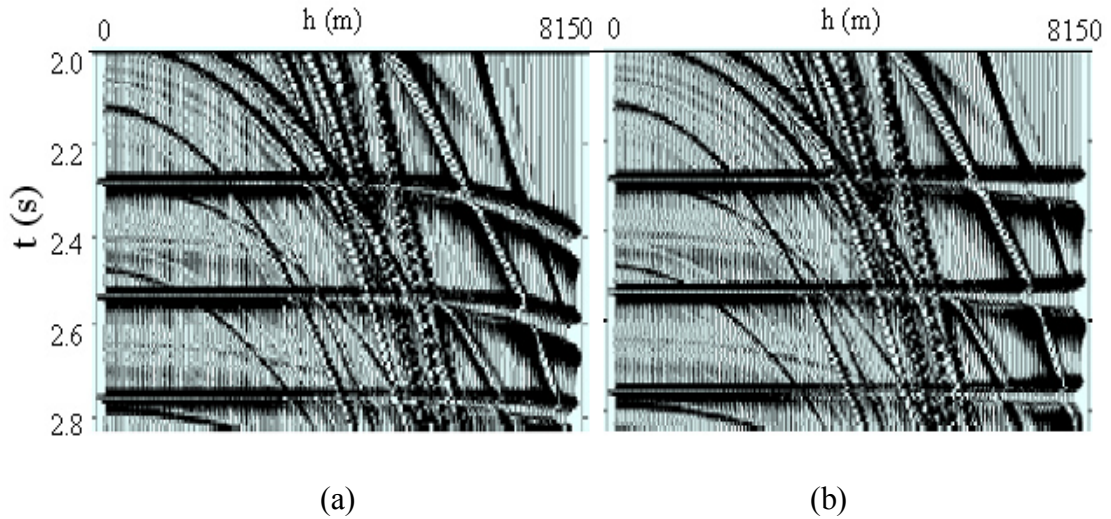


FIG. 1.6. A CMP gather after (a) 4<sup>th</sup> order and (b) optimized 6<sup>th</sup> order NMO correction. Note the improvement at the far-offsets (after Sun *et al*, 2002).

obtained from the hyperbolic NMO equation and has been related to  $\delta$  ( $\delta$  is one of Thomsen's dimensionless anisotropy parameters, and another one is  $\epsilon$ ),  $V_{po}$  is P wave vertical velocity. Al-Khalifa (1995) demonstrated that the fourth order moveout coefficients contain information about the velocities and anisotropic parameter  $\eta$  of the media. The value for  $\eta$  relates the moveout velocity to the horizontal velocity:

$$\eta = 0.5 \left( \frac{V_h^2}{V_{nmo}^2} - 1 \right) = \frac{\varepsilon - \delta}{1 + 2\delta} \quad , \quad (1.4)$$

where  $V_h$  is the  $P$ -wave velocity in the horizontal direction. The parameter  $\eta$ , in conjunction with the isotropic elements due to vertical velocity variation, is a controlling factor in the non-hyperbolic portion of the moveout curve. Knowledge of this anisotropic parameter is sufficient for time processing of anisotropic seismic data. Grechka and Tsvankin (1997) have shown that high order moveout can be expressed directly in terms of the moveout velocity and horizontal velocity. However, neither the anisotropic parameter  $\eta$  nor the horizontal velocity is sufficient for correct depth processing of seismic data. In general a velocity and two anisotropic parameters define the  $P$ -wave VTI anisotropy. Velocity anisotropy may significantly enhance the deviations from the hyperbolic moveout. With a growing understanding of the behavior of the traveltimes, various researchers have shown that the anisotropy further complicates the orderly behavior of the reflected traveltimes. Means have been developed to extract information on rock properties from long-offset data by inversion of non-hyperbolic moveout from the data.

The current trend in seismic imaging with the long-offset data is to tackle difficult geologic settings, such as to illuminate low velocity zones beneath high velocity overburdens. According to energy partition predicted by the Zoeppritz equation (Figure 1.5), the percentage of energy reflected from a seismic interface increases

compared to the energy transmitted through the interface. Taking this advantage, some published works used wide-angle wave field to image problematic areas below high acoustic impedance layers (such as sub-basalt, sub-salt). The impedance contrasts of those formations are typically undistinguishable by conventional methods. Fliedner and White (2001) demonstrated that low velocity sediment beneath the basalt causes a step-back in the first arrival. Its amplitude is controlled by the thickness and the velocity of the low velocity zone, and the offset at which the basalt refraction dies out is controlled by the thickness of the basalt and by the vertical velocity gradient within it.

In far-offset the successful imaging using refraction (head wave) and specific wide-angle reflection has been achieved. Especially at crustal scale, seismic tomography is a popular tool for mapping velocity structure from earthquake data (Zhou, 1997). Seismic tomography is able to solve for laterally varying velocity models. Among different tomography methods, first arrival particularly effective because ray paths associated with further offset penetrate greater depth, first arrivals at far-offsets are often of high quality and can be easily detected and picked.

In order to obtain a velocity-depth model from refraction data, Clayton and McMechan (1981) presented a wave field continuation approach to estimate a 1-D

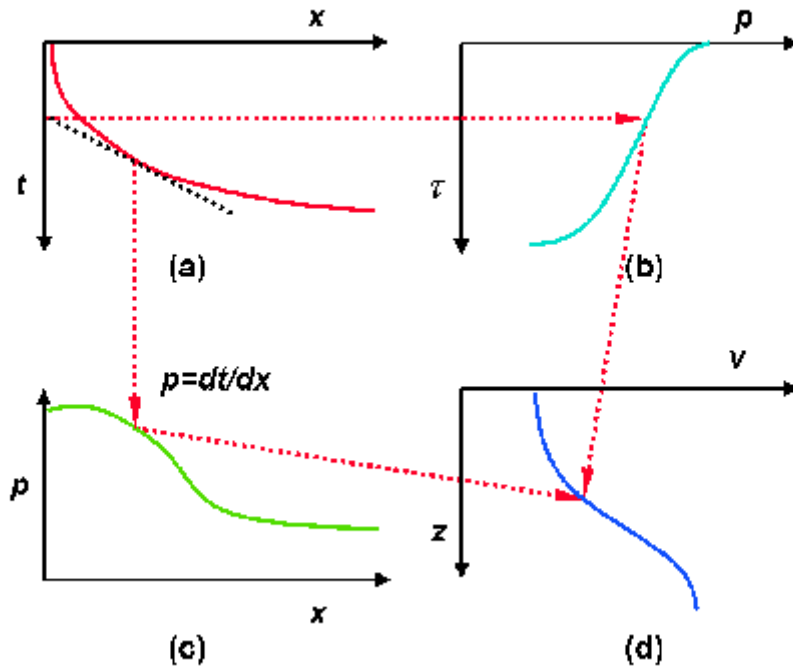


FIG. 1.7. Schematic diagram of 1-D traveltimes inversion. (a) Traveltime versus offset, (b) Traveltime in  $\tau$ - $p$  domain, (c) Traveltime in  $x$ - $p$  domain, (d) the final velocity-depth model (Osypov, 1996).

velocity model. Instead of extracting traveltime information and performing a Herglotz-Wiechert (H-W) integration to produce a velocity-depth profile, they adopted a refraction inversion by double transformation of the entire data. A slant stack transforms the wave field from the  $(x-t)$  domain to ray parameter-time intercept ( $\tau$ - $p$ ) domain. Then a downward continuation transforms linearly from the  $\tau$ - $p$  domain

directly into the slowness-depth domain. The main advantage of the method is to remove the initial mode dependency. Since the entire data (wave field) is present throughout the inversion, no traveltimes pick is necessary. Reiter *et al.* (1993) extended the technique to the estimation of 2-D velocity model by performing downward continuation along numerically computed raypaths. Osypov (1998, 2000) used a  $\tau$ -p refraction tomography method that decomposes the observed first arrival traveltimes into an equivalent  $\tau$ -p representation and estimates the velocity-depth model from the derived  $\tau$ -p representation using hybrid H-W approach (Figure 1.7). A desirable way for first arrival tomography is to reformulate it as a linear problem.

Kosloff *et al* (1996) presented a method for velocity and interface depth determination based on tomography of migrated common reflection point (CRP) gathers. By converting depth errors in migrated CRP gathers to time errors along CRP rays, they were able to use traveltimes tomography on depth migrated CRP gathers.

As the offset increases beyond the critical distance, a rich suite of events comes into play. In addition to PP reflections, PP and PS refractions as well as PS (converted wave) reflections are more pronounced. Early papers tended to focus on the imaging method of the reverse-time migration. For the special case of linearly increasing velocity with depth, Sabnis and Gardner (1989) proposed phase-shift method; Ratcliff *et al.* (1992) demonstrated a turning wave migration using a Kirchhoff integral

method. Youn and Zhou (1998) demonstrated a full-wave reverse-time depth migration, which uses all types of waves (reflection, refraction, diffraction, transmission and multiples) in both forward and backward propagation, showing significant promise in mapping long-offset data (Figure 1.8).

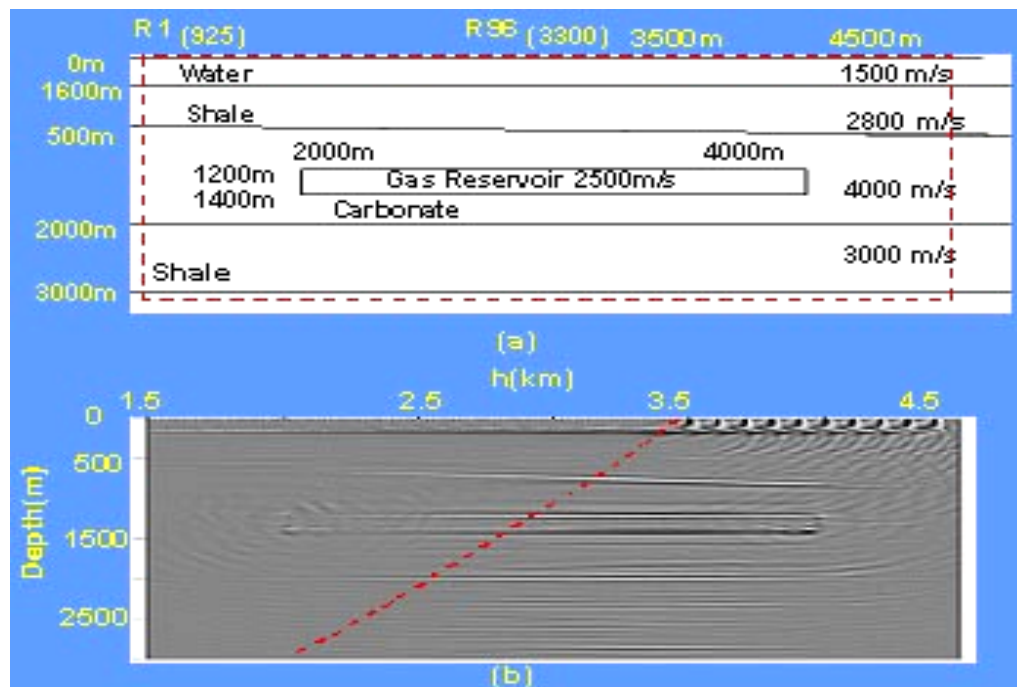


FIG. 1.8. A synthetic example of full-wave migration (Youn and Zhou, 2001). (a) Model and acquisition parameters. (b) Migrated image of the dashed area in (a). Only ten shot gathers were used, with shot locations shown in the right corner of the image between 3500 m to 4500 m, The dashed line corresponds to  $h = z$ , where the NMO mute is normally applied.

## **1.4 Organization of the chapters**

In Chapter 1, I addressed the advantages and challenges of using long-offset data, outlined the objectives of the thesis, and reviewed some imaging methods for long-offset data.

In Chapter 2, I will present the design and implementing of a new AGL LabVIEW-based physical modeling system, including flowchart, subroutine hierarchy, and performance test. I will also describe physical modeling of long-offset data, including turning wave and wide aperture data collection. Discussion will also be given on attempts to improve the acquired data quality and comparison with numerical modeling.

Chapter 3 is devoted to the estimation of velocity model using a newly developed deformable layer tomography (DLT) algorithm. It is applied to crooked line long-offset field data.

In Chapter 4, Kirchhoff integral and reverse-time migrations are used to migrate long-offset data. Comparison of the migration over different offset ranges of physical modeling and numerical modeling data will also be given.

Chapter 5 covers the conclusions of the thesis.

In Appendix A, a user manual of the AGL new LabVIEW-based physical modeling system is provided.

In Appendix B, source signature and acoustic field of physical modeling are discussed, including the transducer, the source signature, the directivity of a source field, and the noise.

In Appendix C, two methods that are used to address “birth defect” of seismic physical modeling are discussed.

## **MODELING OF LONG-OFFSET SEISMIC DATA**

### **2.1 A new LabVIEW-based physical modeling system**

While the skeleton of the physical modeling system is the hardware, the brain of the operations is a custom designed software package. I have designed this software package in LabVIEW for AGL's new physical modeling system under the guidance of Dr. Kurt J Marfurt and Dr. Robert Wiley. The system consists of signal generation, data acquisition, and acquisition automation to simulate the general seismic survey. It features a flexible geometry capability, a simple user interface (x, y, z tables in which the movement of transducer is controlled), cross correlation, vertical stack, spectrum analysis, shot gather display, data annotation, and transducer position display.

#### **2.1.1 Hardware configuration**

The system consists of the following components (Figure 2.1):

1. PCI-6110E DAQ board; BNC-2090 BNC Adapter;
2. NuDrive-4sx-411 NI NuDrive (multi-axis power Amplifier interface);
3. M091-FD06E (step 200, 2.6 v) stepping Motor (made by Superior electric Inc.);

4. PCI-7344 NI motion control board (mounted in DEL 21152 PCI to PCI bridge);
5. 5055 PR serial 373 pulses receiver (made by Panametrics Inc.); and
6. 5660B (serial 1117) Ultrasonic pre-amplifier.

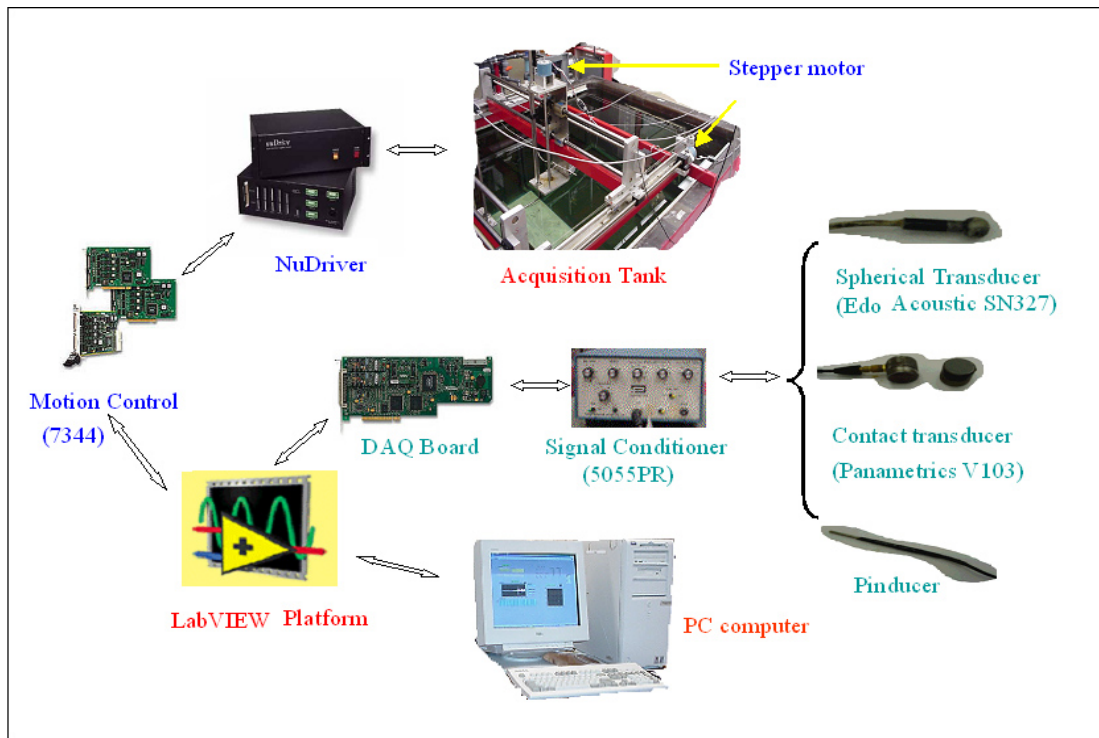


FIG. 2.1. Components of AGL's new physical modeling system. The Plug-In data acquisition (DAQ) board replaces traditional benchtop instrumentation; two 7344-motion control boards and nuDrivers control the motion of the source and receiver; stepper motors are mounted on the top of the tank.

## 2.1.2 Flow charts of the major programs

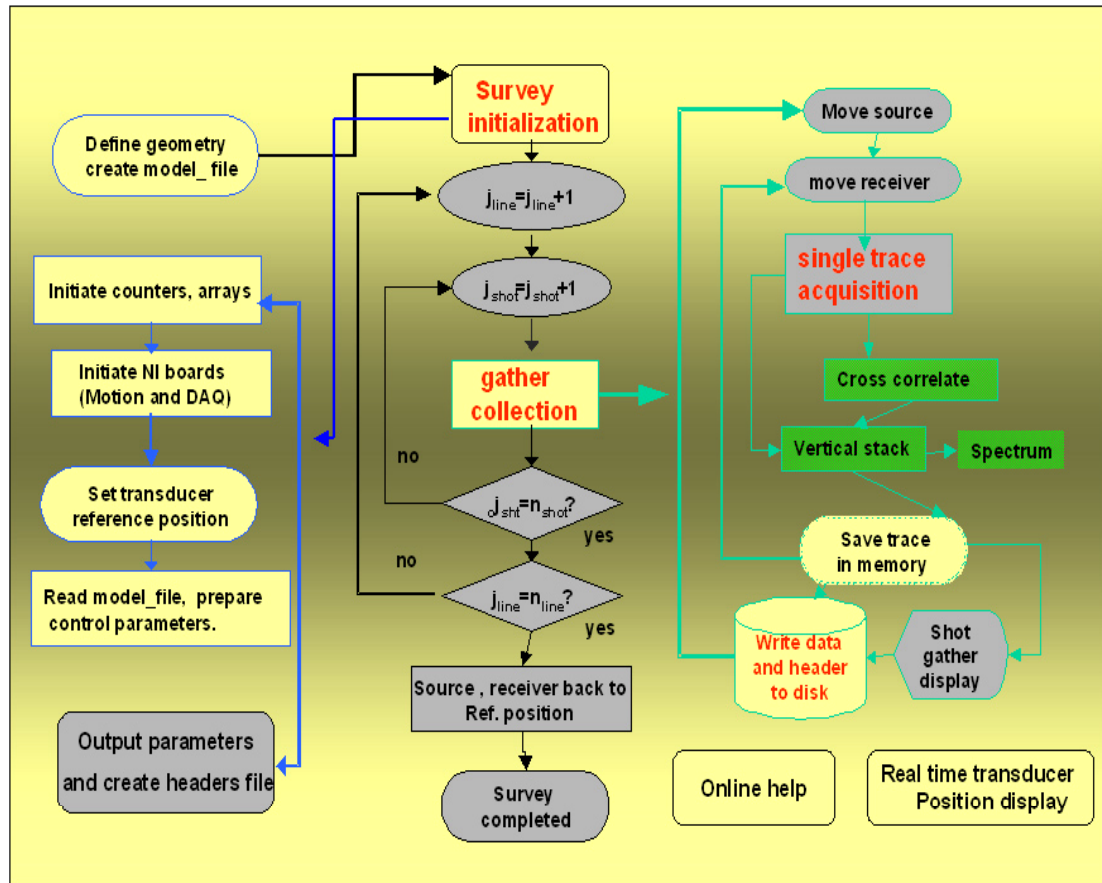


FIG. 2.2. Flow diagram of the main program showing collection of a common-shot gather on multiple streamers. Details of the survey initialization, gather collection and trace acquisition blocks are shown in Figure 2.3-2.5.

The program mainly consists of signal generation, data acquisition and acquisition automation. Figure 2.2 shows a flow diagram of the main program. Figure 2.3 shows the detail of the survey initialization block flow chart. Figure 2.4 shows a detailed gather collection block flow chart, and Figure 2.5 shows the detail of a single-trace acquisition block flow chart.

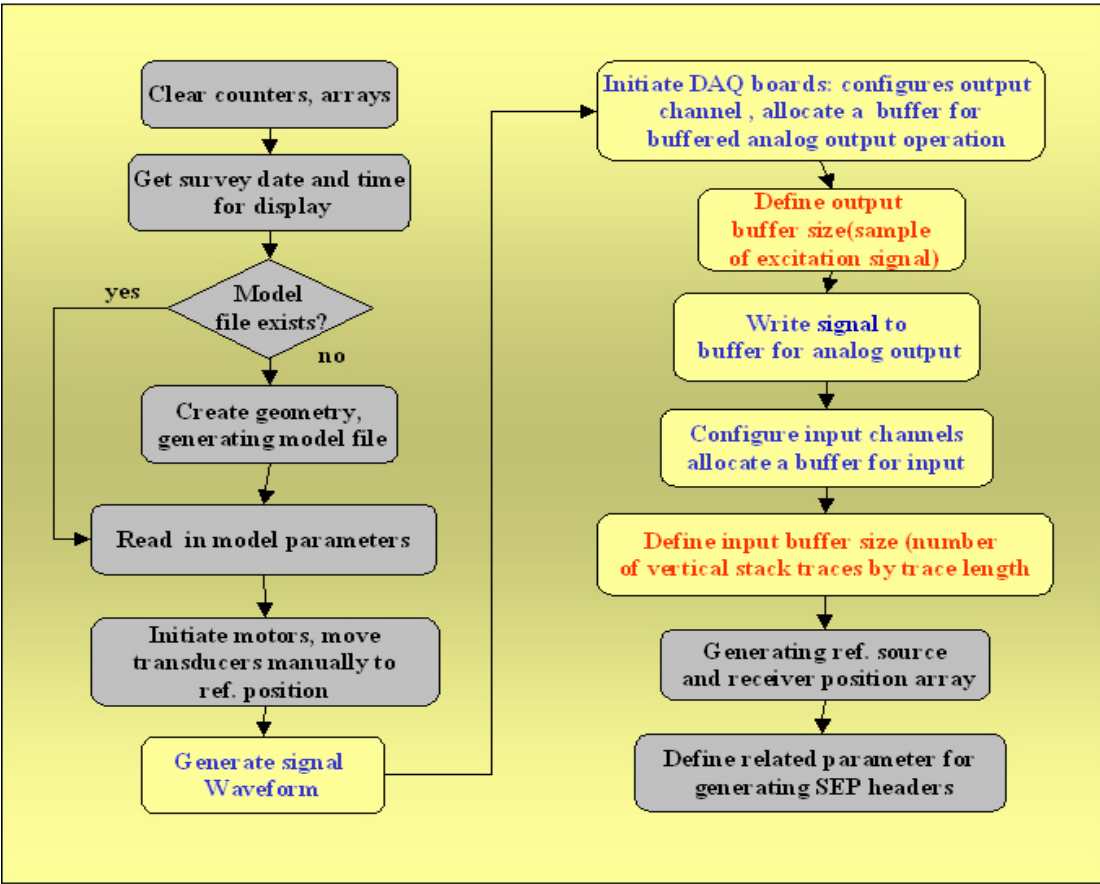


FIG. 2.3. Detail of survey initialization block shown in Figure 2.2.

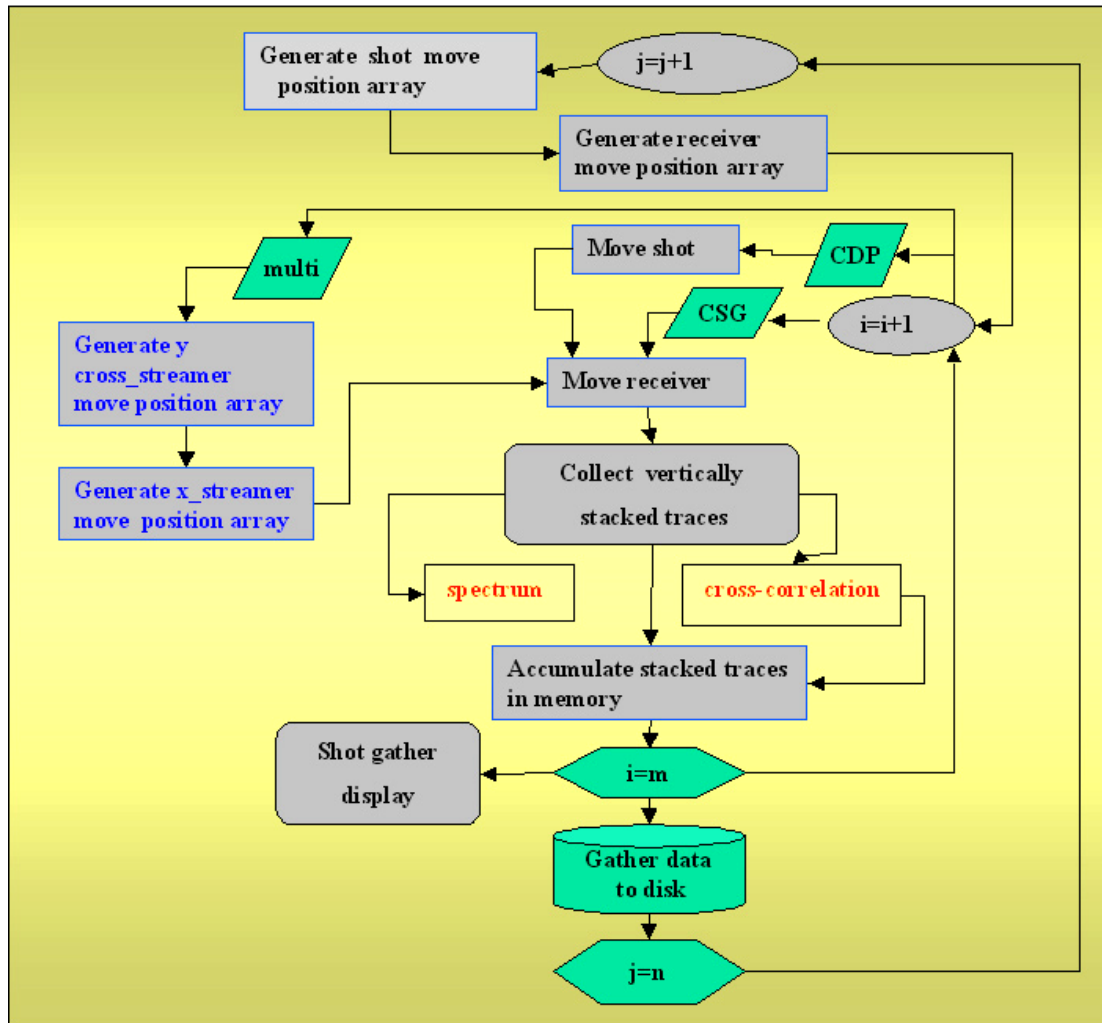


FIG. 2.4. Detail of gather collection block shown in Figure 2.2.

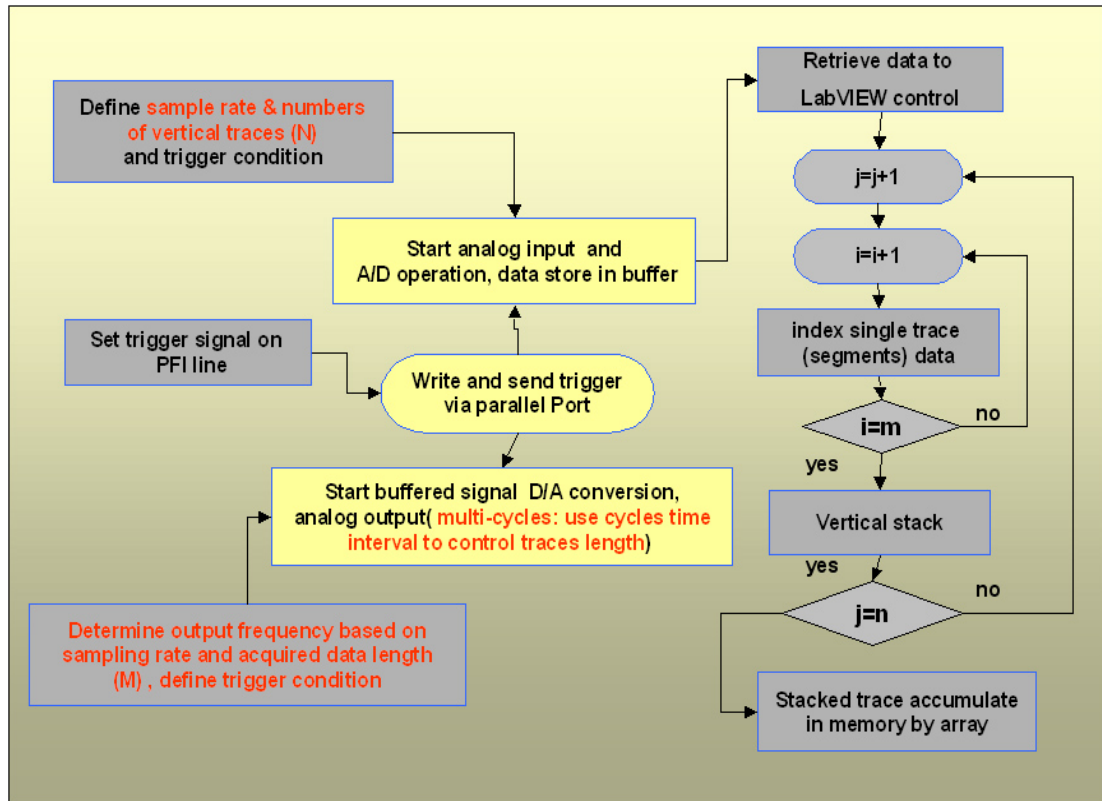


FIG. 2.5. Details of a single-trace acquisition block shown in Figure 2.2, where  $i$ ,  $j$ ,  $m$  and  $n$  are sample index, trace index, number of samples per trace and number of traces for vertical stack, respectively.

### 2.1.3 Subroutine hierarchy

The LabVIEW physical modeling system consists of 29 subroutines (subVIs), their names and functions can be found in Table 2.1. The corresponding subroutine hierarchy is shown in Figure 2.6.

*Table 2.1. Subroutines of the LabVIEW physical modeling system*

Name of VI (or subVI)	Function
AGL_Pmod	Main program
More info.	Help generation
3ax.abs M	3-axis move control
SEPHis	SEP header file generation
SEP HF	SEP header format generation
SEP HF	Multi-streamer receiver position array generation
RecPos	Single streamer receiver position array generation
Spect	Trace spectrum analysis
DAQ	Signal generation and data acquisition
Conn Chk	Signal connection check and velocity measurement
Shot	Source position array generation
VSP Rec-z	VSP receiver moving position array generation
Text	Help information
Initi motor	Motion board initialization
END	Survey completed reminder
Acq_Start	Start A/D operation
InPut_Conf	DAQ input configuration
DeoEdit	Geometry definition
DAQ conf	DAQ initialization

Table 2.2. Subroutines of the LabVIEW physical modeling system (continued)

Dig_Trig	Digital trigger signal generation
Signal	Source signal generation
OutP Conf	DAQ output configuration
OutP Start	Start buffered signal D/A conversion
Gath Disp	Gather display
Prep data graph	For instantly transducer position display
Move Contr	Manually movement control
Writ buffer	A/D data stored in buffer
Ref. pos	Set reference position
One Axem	Single axis movement control

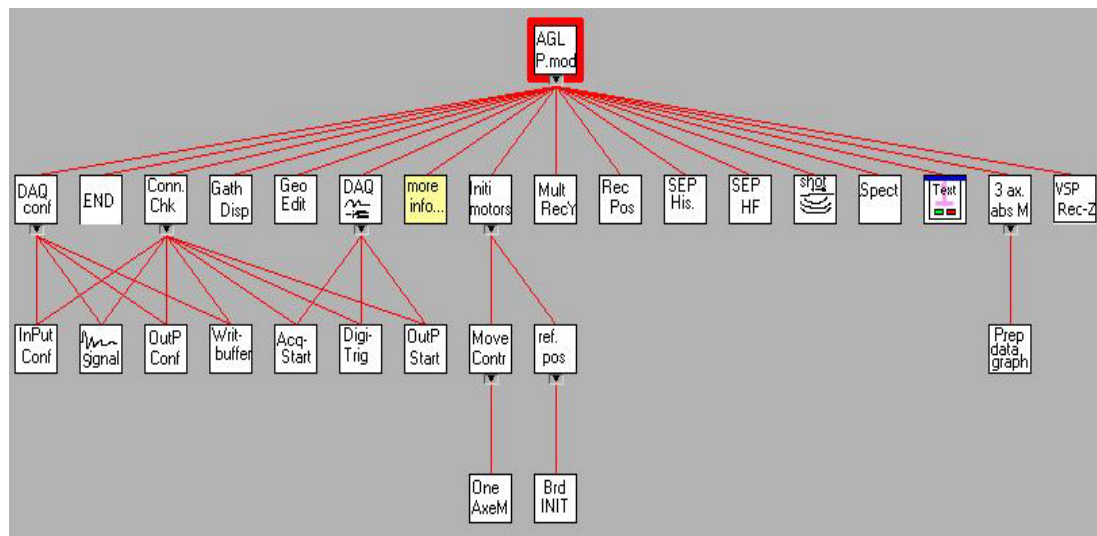


FIG. 2.6. Subroutine hierarchy of the programs corresponding to Table 2.1.

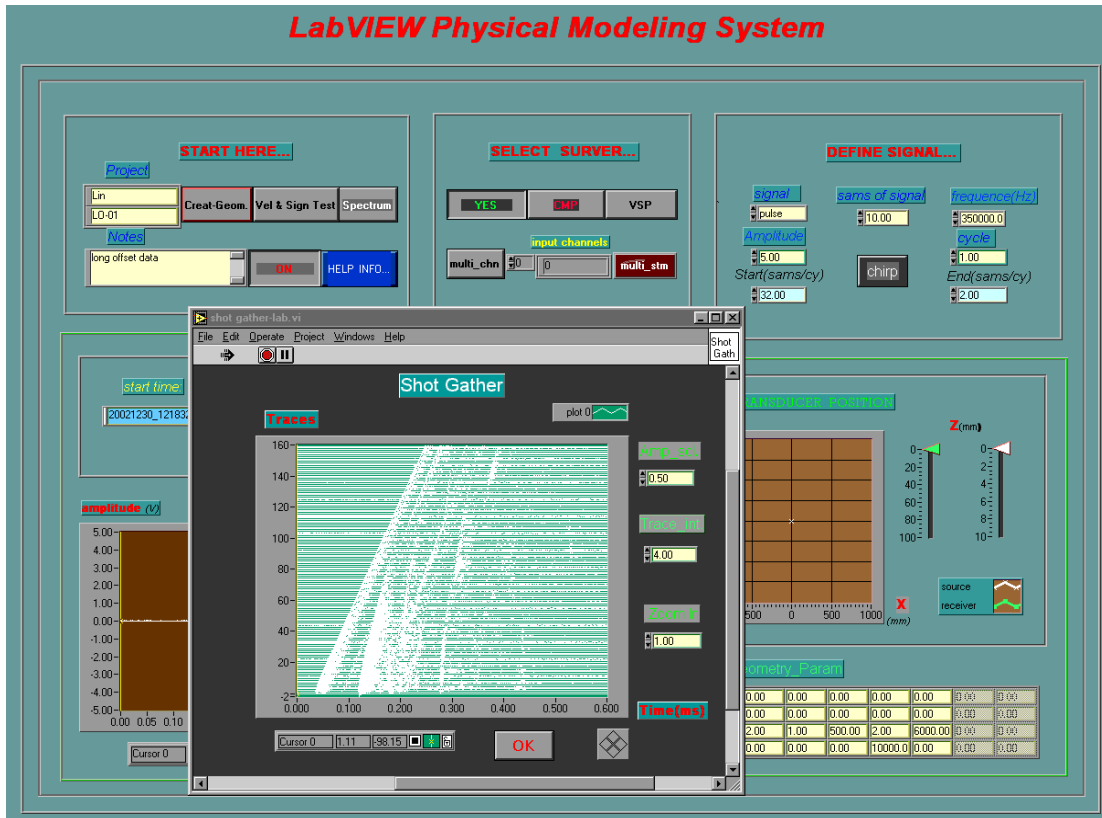


FIG. 2.7. Front panel of the main program. A modeling experiment was in progress.

### 2.1.4 Interfaces

The interface (front panel) of the main program (Figure 2.7) includes a control panel, which provides survey type selection and signal definition, and acquisition status display that includes the current positions of the transducers, the progress of the data acquisition, and the more recently acquired trace's data. Figure 2.8 shows the user interface of geometry definition, a simple X, Y, Z table being used to control the

movement of the transducers. The system can also incorporate non-standard acquisition geometry.

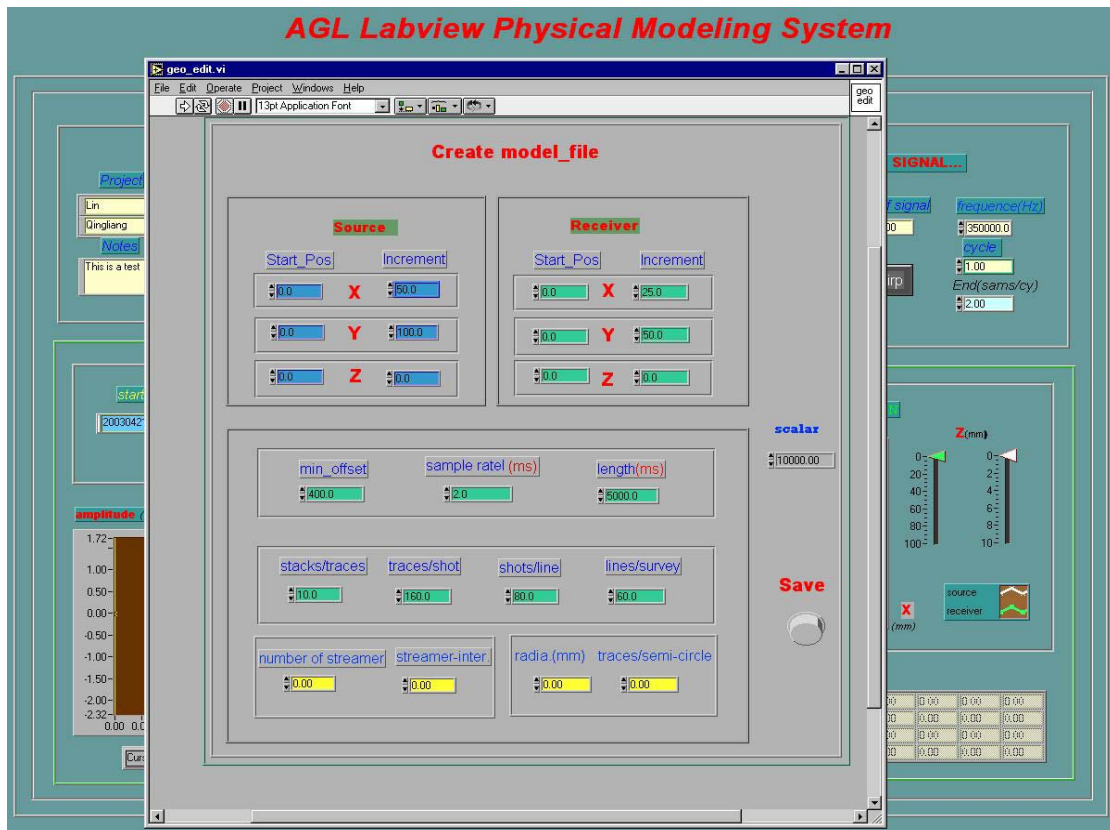


FIG. 2.8. Interface of geometry definition. A simple X, Y, Z table was used to control the movement of the source and receiver transducers.

### **2.1.5 Functions**

The system integrates acoustic and elastic modeling in one program. Geometry capability includes common-shot, common mid-point (CMP), vertical seismic profiling (VSP), single channel simulating multi-streamer and multi-channel simulating multi-streamer (maximum 4 channels). Signals used to excite the transducer include pulse, impulse, sine wave and chirp. Trace display can be switched between channels. A *Spectrum* subVI for single-trace spectrum analysis based on FFT provides different windows and graphs in different units (V, db). *Help info* provides a simple user manual for convenient operation. *Vel & Signal Test* provides a quick check of signal connection status, amplitude level of the received signal and a means for model material property measurement. The *gather display* (Figure 2.9) is helpful in quality control during the acquisition experiment. The *elastic* function drives both the source and receiver transducers along the model surface by picking them up, moving them forward, and setting them down like human footsteps.

### **2.1.6 Performance test**

#### ***2.1.6.1 Effect of the movement of transducers on data quality***

The movement of the transducers to each location involves both acceleration and deceleration. In order to check the effect of the movement of transducers on recorded

data quality, a single-measured trace of data was repeatedly recorded twenty times at each location (Figure 2.10). Since the traces for vertical stack are well aligned and no waveform distortion is observed, the movement of transducers does not affect the quality of the acquired data.

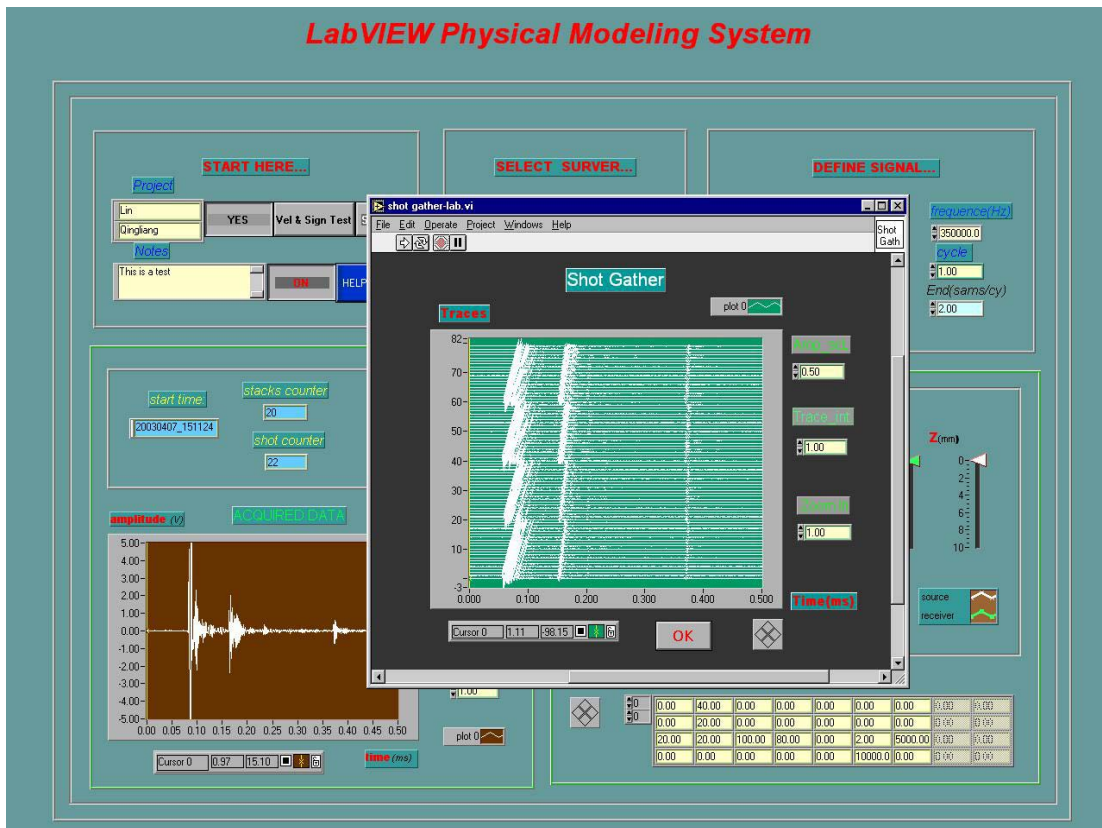


FIG. 2.9. Gather display shows a 4-steamer common-shot gather. The operator can select the trace interval, scale the amplitude, and zoom in to a time interval of interest.

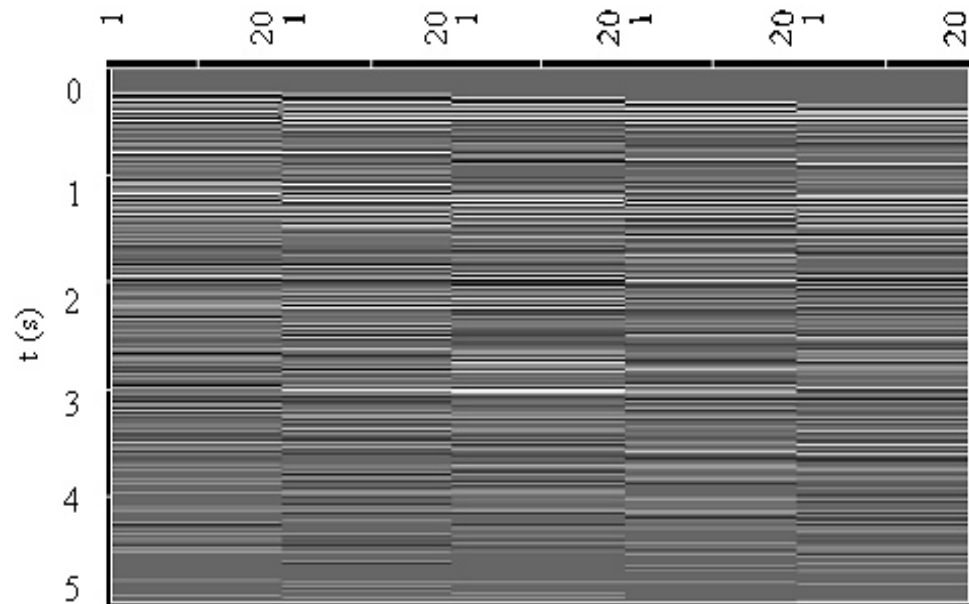


FIG. 2.10. A single-measured trace (before vertical stack) acquisition was repeated twenty times at five different receiver locations during the progress of common-shot gather acquisition. The rod holding the transducer appears to vibrate after moving to a new position, and the recorded waveform appears to be highly repeatable.

### ***2.1.6.2 Timing test***

After making the system (hardware and software) work, it is important to improve its performance. Determining where the applications spend their time and how they use the memory is helpful in searching the running bottlenecks of the programs. After profiling the performance of the program and modifying some of the slower subVIs, I

obtained the timing test results: (a) for a single channel operation, with 2 ms sample rate, 5 s data recording length, 25 m receiver interval, 50 m source interval, and a 20 times of vertical stack, the data acquisition speed is about 20 single-measured traces per second; (b) for a 4 channels multi-streamer acquisition that uses the same parameters as in (a), the modeling speed is 80 single-measured traces per second. There is still room to improve the efficiency of the codes, especially in coding the drivers.

## **2.2 Modeling of long-offset seismic data**

### **2.1.1 Turning wave physical modeling**

I used a twenty layers “gradient” model to examine the feasibility of physical modeling of long-offset data. The model was built using aluminum powder and clear resin (Table. 2.3) (Zhang, 1994). The velocity gradient was achieved by mixing aluminum powder with clear resin in different proportions (Table. 2.4). The resin has a velocity of 2525 m/s. After adding aluminum powder, the maximum velocity can reach to 3320 m/s. The velocity gradient was controlled at 0.406 according to the proportion of aluminum and clear resin. Velocity would be constant within each layer, but changes from layer to layer. Thus, a relative smooth velocity gradient is established. The dimensions of the model are 60 by 60 by 20.5 cm (Figure 2.12 b).

*Table. 2.3. The properties of clear resin and aluminum powder*

Parameter	Clear resin	Aluminum powder
Density $\rho$ (g/cm <sup>3</sup> )	1.25	2.68
Compression velocity $\alpha$ (m/s)	2488	6420
Shear velocity $\beta$ (m/s)	1207	3040
Bulk modulus $\kappa$ (10 <sup>10</sup> dynes/cm <sup>2</sup> )	5.310	77.44
Shear modulus $\mu$ (10 <sup>10</sup> dynes/cm <sup>2</sup> )	1.821	24.78

The data was shooting using AGL's new LabVIEW physical modeling system. In order to simplify the event identification, the transducer was deployed sufficiently deep to avoid surface multiples. The source and receiver were placed at an offset of 3.8 cm (corresponding to 380 m in field, after a 10000 scaling up) and at a distance of 5 cm above the top of the model. The source spacing was 1 cm, and the receiver spacing was 0.25 cm. It was estimated that a trace length of 0.6 ms (corresponding to 6 seconds in field) would be able to cover the entire pertinent event from the model, so 0.6 ms data was recorded with 0.2  $\mu$ s sampling interval.

To enhance the signal to noise ratio, a 15 times vertical stacking was applied. The critical distance on the top of the model is about 6.54 cm, corresponding to a critical angle of 36 degrees.

*Table. 2.4. Velocities as a function of mass ratio of aluminum powder to clear resin*

Mass ratio (Aluminum/resin)	Volume of aluminum powder (%)	Density (g/cm <sup>3</sup> )	$\alpha$ (m /s)	$\beta$ (m /s)
0.0	0	1.25	2488	1207
0.2	8.5	1.37	2531	1259
0.3	12.3	1.42	2570	1282
0.4	15.7	1.47	2609	1316
0.5	18.9	1.52	1662	1353
0.6	21.9	1.56	2711	1387
0.7	24.6	1.61	2735	1409
0.8	27.2	1.64	2783	1439
0.9	29.6	1.67	2817	1464
1.0	31.8	1.71	2863	1495
1.1	33.9	1.75	2912	1531
1.2	35.9	1.76	2935	1545
1.3	37.8	1.79	2983	1570
1.4	39.5	1.83	3032	1592
1.5	41.2	1.85	3055	1617
1.6	42.7	1.87	3096	1636
1.7	44.2	1.90	3137	1675
1.8	45.7	1.93	3164	1687
1.9	47.0	1.93	3182	1698

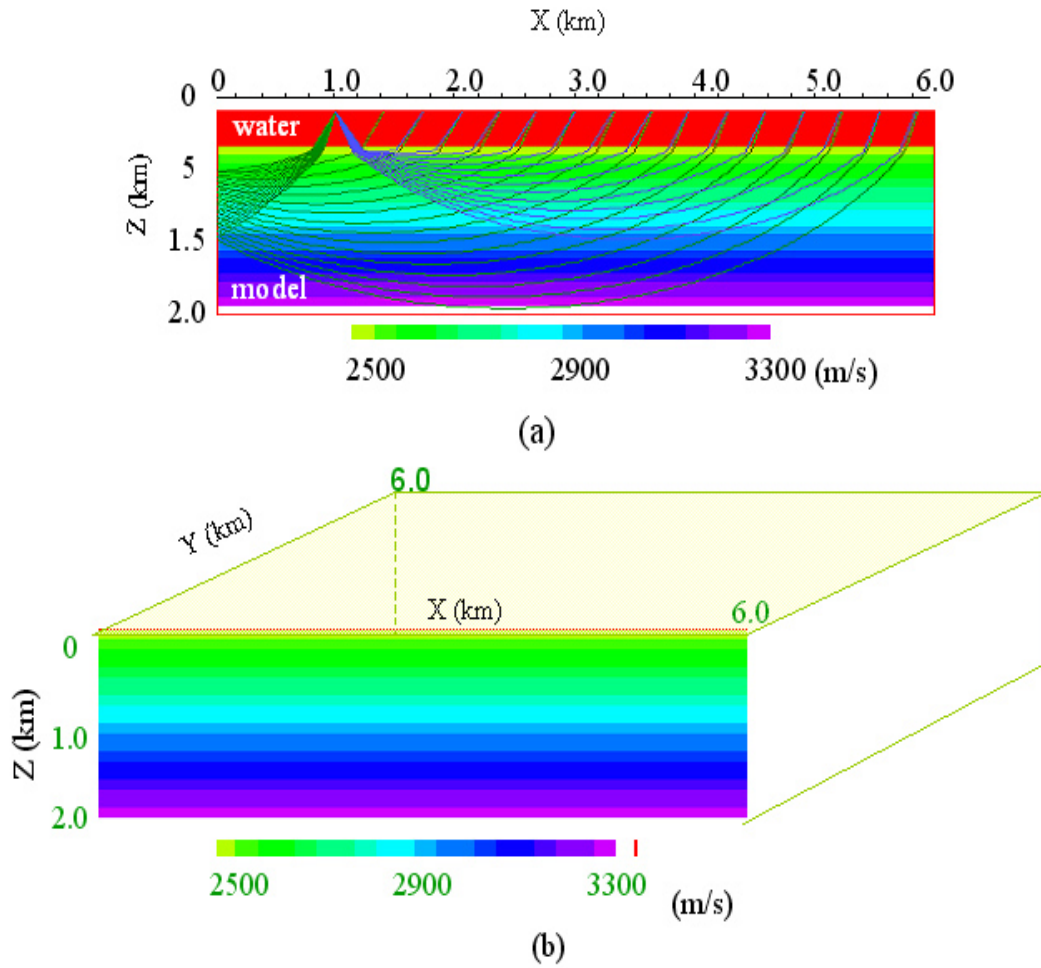


FIG. 2.12. (a) A 2-D view of physical model submerged in water and its velocity gradient, expected turning wave raypaths being shown. (b) Dimensions of the model.

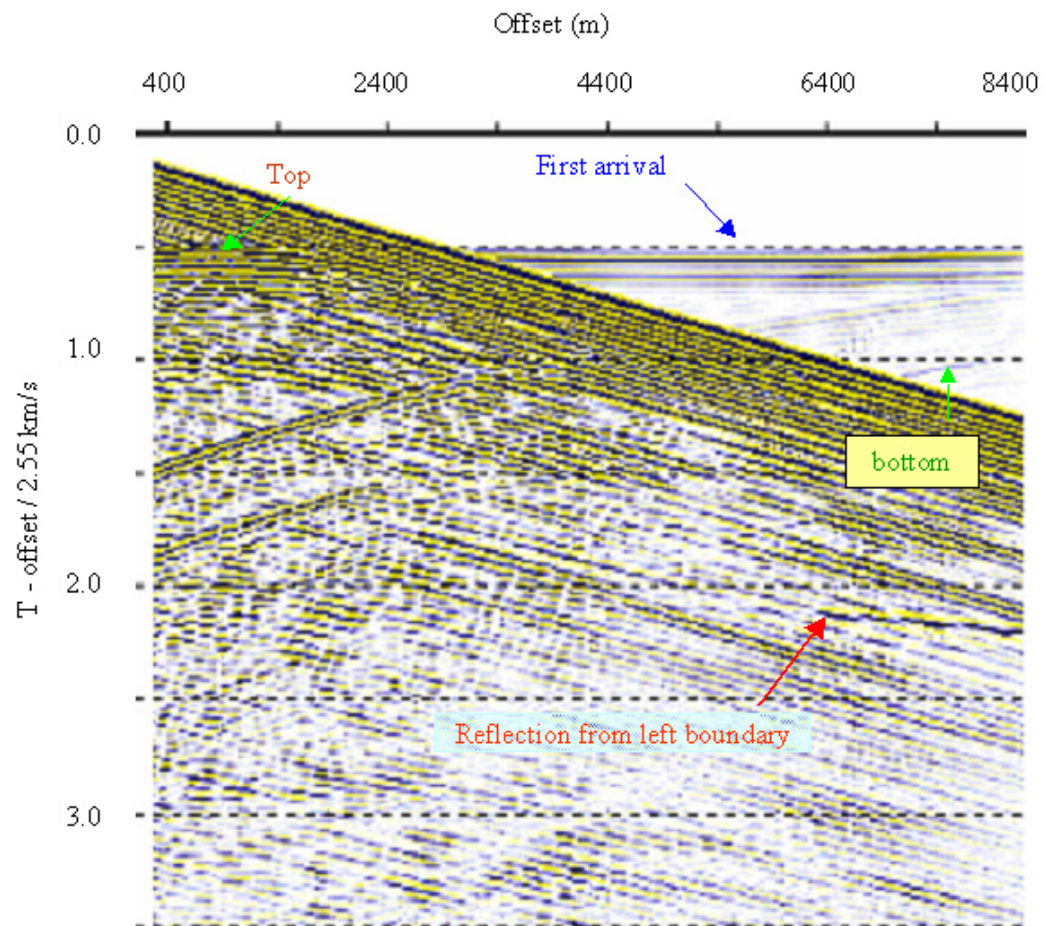


FIG. 2.13. A common-shot gather of physical modeling data, traveltime was reduced at 2.55 km/s, turning wave and post-critical reflection can be identified.

The acquired data (Figure 2.13) show that the first arrival was contaminated by strong direct wave. To cope with this problem in the modeling stage, I used a Mouse-pad to degrade the direct energy (Appendix C). There are some events that are notable in the acquired shot gathers: first arrival that turns from the horizontal model interfaces and wider-aperture reflections from the top, bottom and the subsurfaces of the model. By analyzing different events based on traveltimes varying along shot line, two relative dip reflection events whose traveltimes vary along the shot line were identified. When one of them increases in one direction, the other decreases in the same direction (Figure 2.14). Ray path in ray tracing modeling of vertical interface also shows a consistent result, they are likely reflections from the two vertical model boundaries (Figure 2.14 b). CMP gathers also show abnormal moveout of the corresponding events.

### **2.2.2 Wide-aperture physical modeling**

The model is a piece of Plexiglas with a flat surface on the top and a curved surface on the bottom (Figure 2.15). The lateral dimensions are 38 by 38 cm, while the thickness ranges from 5.6 to 7.8 cm. It was supported by 4 pieces of metal on the corners. The model was placed on the top of a stainless steel platform. Two Parametric HTI-96-300 spherical transducers were used as the source and the receiver. The transducers were deployed deep into the water to avoid surface multiples. The acquisition geometry is

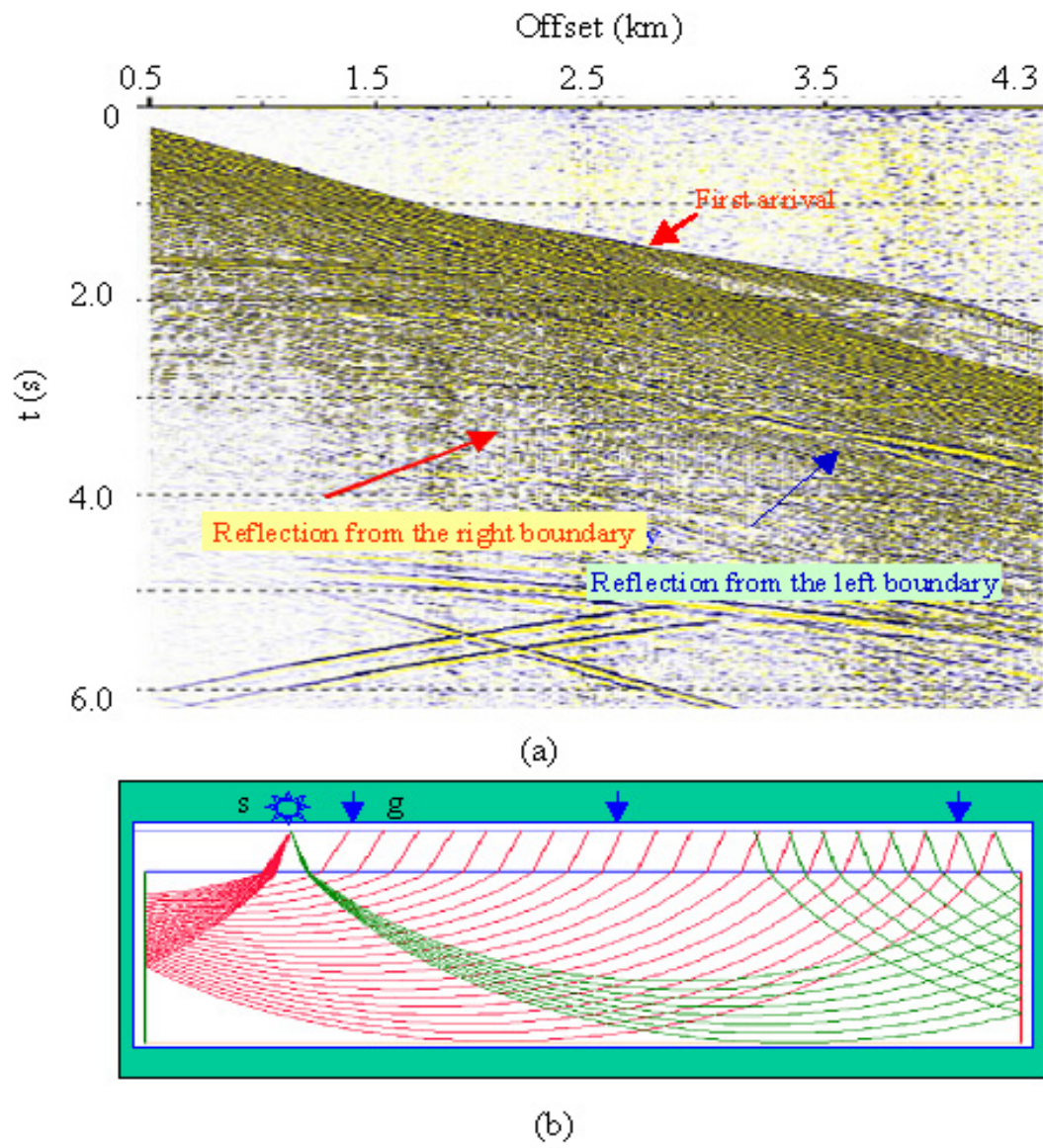


FIG. 2.14. (a) A shot gather showing the reflections from the vertical boundaries. (b) The raypaths from ray theoretical modeling inferring the corresponding reflections.

an off-end roll along geometry. The acquisition was proceeding from the right to the left. Since the model is a typical 2.5-D model, I collected a 2-D line only. The source and receiver were placed at an offset of 2.5 cm and at a distance of 11cm above the top of the model. The source spacing was 0.5 cm, and trace length was 0.6 ms, and the voltage of the excitation signal was a 5-volt pulse. The input analog signal was pre-amplified via an ultrasonic pre-amplifier and was adjusted to 10-volt peak to peak. I vertically stacked the data 15 times to enhance the signal to noise ratio. The critical distance on the top of the model is about 14.3 cm. The corresponding critical angle is 33 degrees.

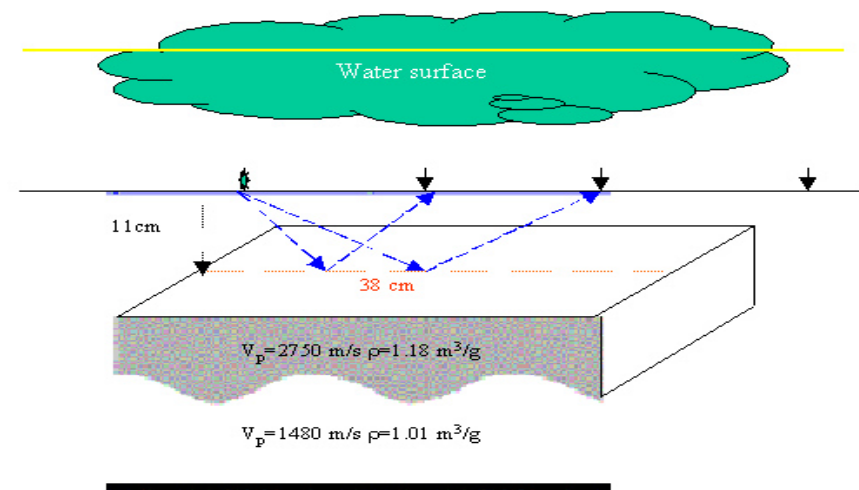


FIG. 2.15. Schematic diagram of the physical modeling set up for wide-aperture acquisition.

Acquired data (Figure 2.16) show that beyond the critical distance the reflection amplitude on the top of the model was attenuated faster than the refraction amplitude. Some features of long-offset data were hard to predict, such as amplitude variation with offset and phase reversal.

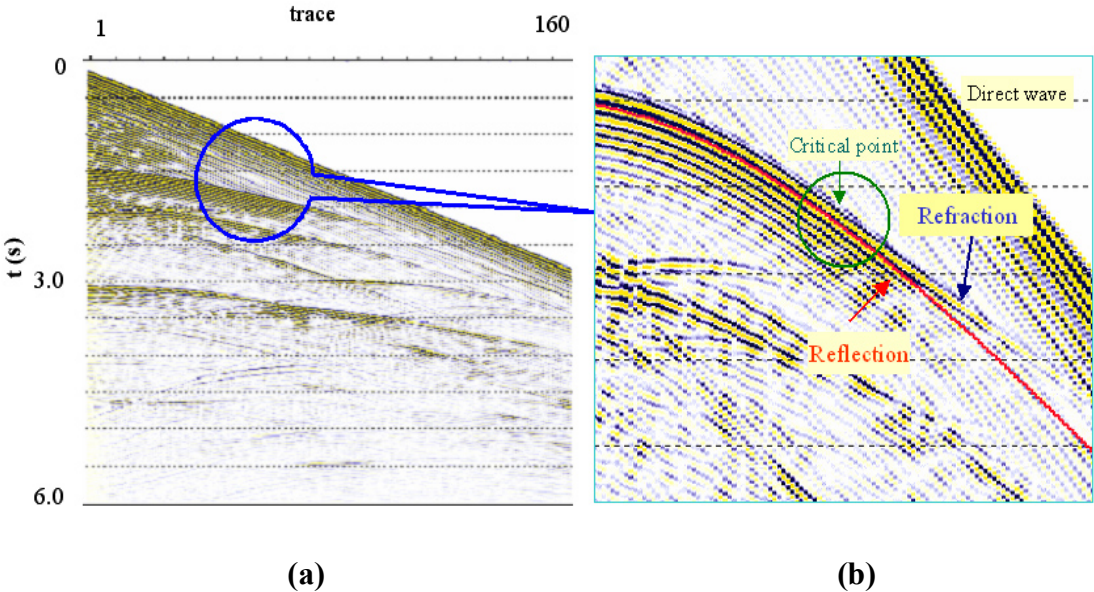


FIG. 2.16. A shot gather (a) and its close up zooms (b).

### 2.2.3 Crosswell physical modeling

In order to measure the velocity of the “gradient” model by crosswell tomography, a “crosswell” data acquisition was designed. Two Piezoelectric flat-faced cylindrical contact transducers were used as the source and the receiver in the experiment. The contact transducer has an active element of 12.8 mm in diameter with the maximum

sensitivity normal to the contact surface. During the operation the contact faces are coupled to a selected flat surface by using Grandma's molasses. A 5-volt pulse was used to excite the source transducer with a frequency of 350 kHz. Pre-amplified data were sampled using a sampling interval of 0.2  $\mu$ s. The acquisition setup is shown in Figure 2.17. The first source is positioned at a distance of 1.65 cm from the top surface of the model. The others are rolled down at an increment of 1.0 cm, for a total of 18 shots. The first receiver is positioned in a distance of 0.85 cm from the top surface of the model; the others are rolled down at a 0.5 cm interval for a total of 36 traces per shot. The length of the data is 0.6 ms (equivalent to 6.0 seconds n field).

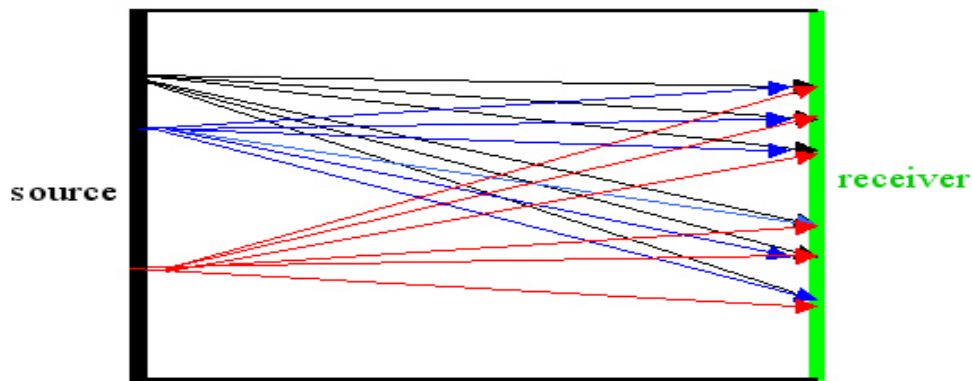


FIG. 2.17. Schematic diagram of the crosswell data collection.

Figure 2.18 shows one shot gather of the acquired data. As expected, the down going direct arrival is the strongest event. There are some other up going events (reflections) and down going events (multiples) as well. The reflections from each layer should be

more pronounced but they can not be readily distinguished in the raw data. The reason for the lack of reflection events can be attributed to the fact that most of them have a relatively small incidence angle. The incidence angle at the sides of the model, at many points, is far greater than the critical angle, resulting in little, if any, reflected energy reaching the receiver.

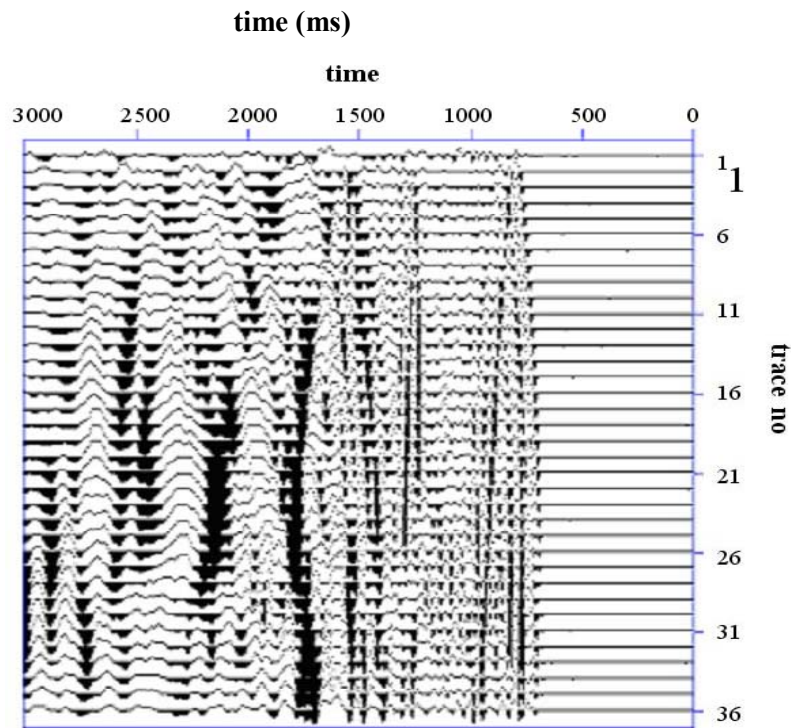


FIG. 2.18. A common-shot gather extracted from the crosswell experiment.

### 2.3 “Vibroseis” source simulation

Pulsing a transducer results in severe ringing and narrow bandwidth. In order to reduce ringing and improve signature bandwidth, as well as the signal to noise ratio, I used a chirp signal as the source, and performed the cross-correlation with the source signal. I conducted a series of experiments to determine the effect of different sweep lengths, bandwidths, and sample rates on the final cross-correlated output. I also investigated the correlating gain and vertical stacking folds. I choose a simple model (Figure 2.15) and a selection of sources and receivers for the data acquisition. I started using a chirp with 5-second sweep length (Figure 2.19 a) and a sweep frequency from 50 kHz to 1250kHz. I acquired 5 seconds of data (Figure 2.19 b), took the signal waveform, cross-correlated it with the acquired data, and obtained cross-correlated output signal (Figure 2.19 c). The results show some “precursor” ambient noise. In this test the acquired data (4 ms sample rate) was scaled to maintain the same amplitude as the source signal.

I increased the sweep length to 10 seconds (Figure 2.20 a) and acquired 10 seconds length of data with a sweep frequency from 50 kHz to 1250kHz (Figure 2.20 b). The cross-correlated output (Figure 2.20 c) results in more spiky data. The pulse compression is obvious. The “precursor” noise was attenuated and the energy of the signal was nearly double that of the previous test. Figure 2.21 shows a common-shot

gather that was recorded in single-measured trace with a sample rate of 4 ms using 1-volt source signal.

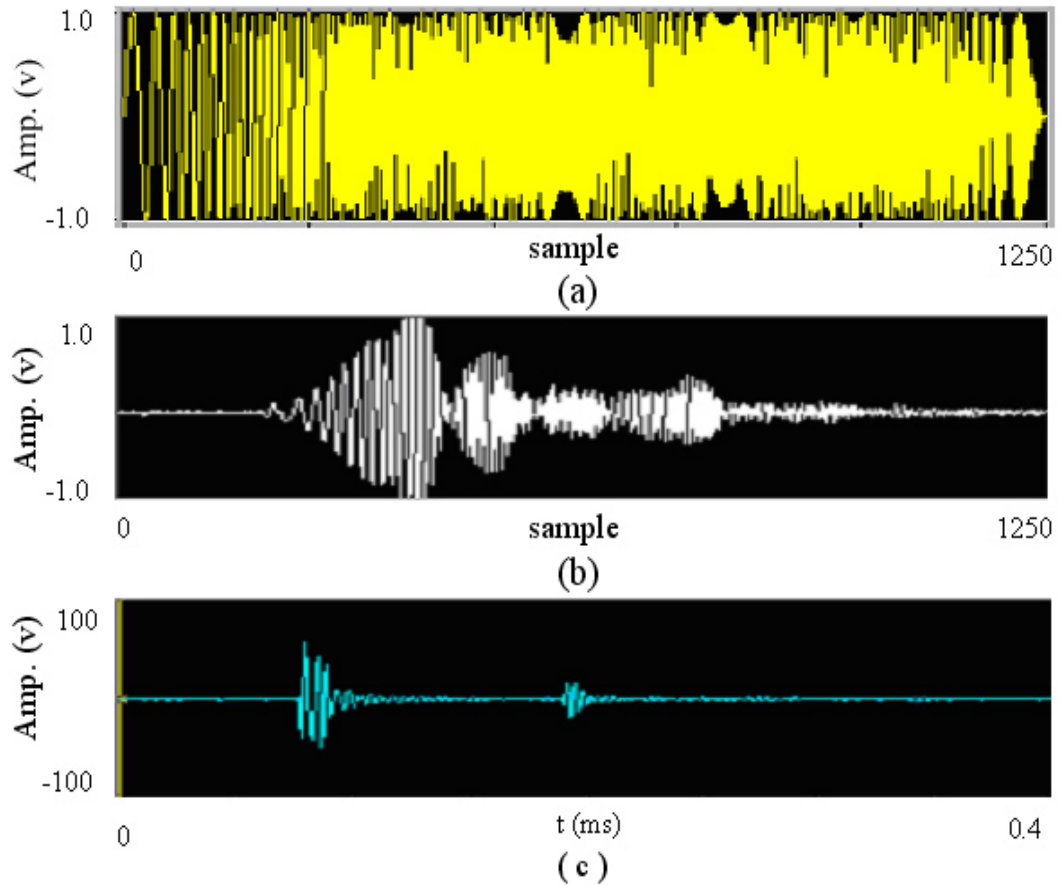


FIG. 2.19. The source chirp pilot (a) was cross-correlated with acquired data (b) to obtain the output trace (c). Length of trace 0.4 ms in model coordinates scales to 4 seconds in field coordinates. Noise arriving before strong first arrival in (c) is representative of ambient noise in our laboratory. No vertical stack was applied. The length of 1250 samples corresponds to a 0.5 ms recording length.

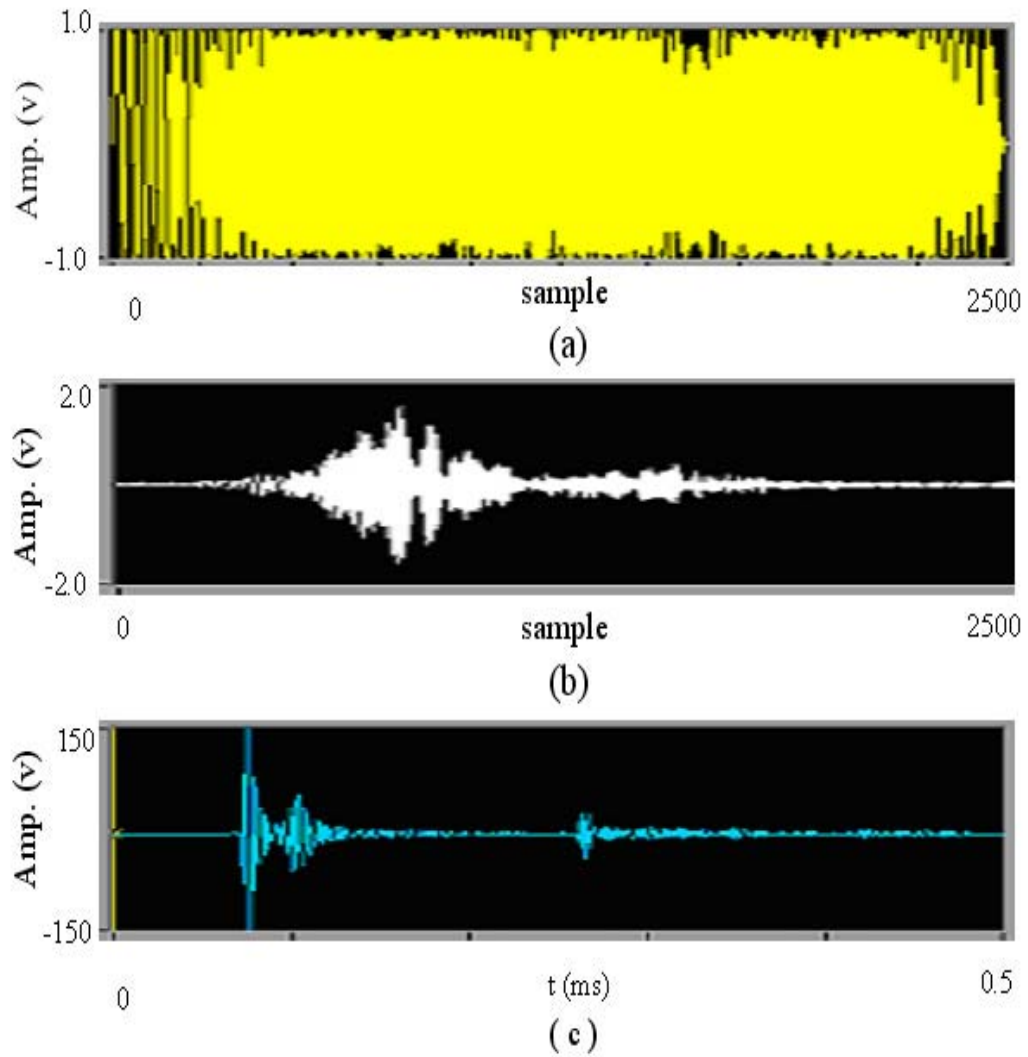


FIG. 2.20. A 20 seconds length of sweep chirp pilot (a) cross-correlated with 10 seconds of acquired data (b) gives the cross-correlated output (c). Note that the ambient noise before the strong first arrival is reduced.

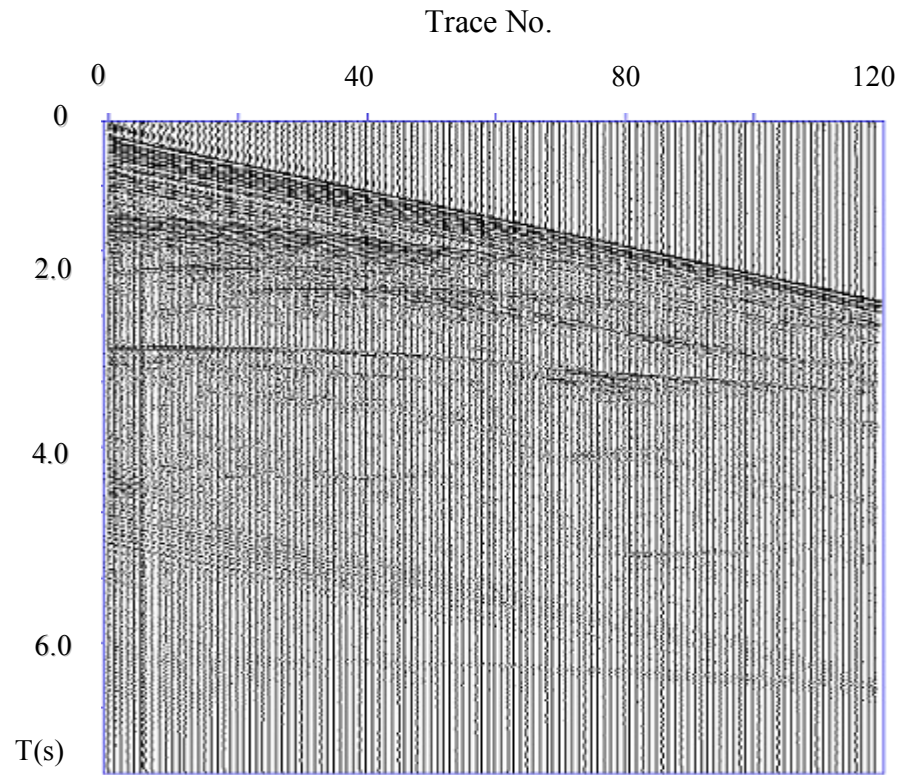


FIG. 2.21. An acquired common-shot gather using chirp signal as the source. The sampling interval was 4 ms in field coordinates. Only single-measured trace data are shown.

Even though there are some artifacts and noise, the reflection waveforms of the subsurface are clearly spikier.

The chirp signal has its advantages. In theory, the cross-correlation between input and output of a linear system is proportional to the impulse response of the system. Using a chirp can improve the final output data resolution. The resolution of the system with the chirp is not a function of transmitted burst length, but is a function of the FM pulse. This provides the opportunity to use the chirp source with low peak power, long sweep, low carrier frequency and wide FM bandwidth. The wider the bandwidth, the narrower the correlated output pulse. Furthermore, the ambient noise is easily rejected since the correlation is with a wide band, low peak power source.

**2.4 Comparison of physical modeling with ray theoretical modeling**

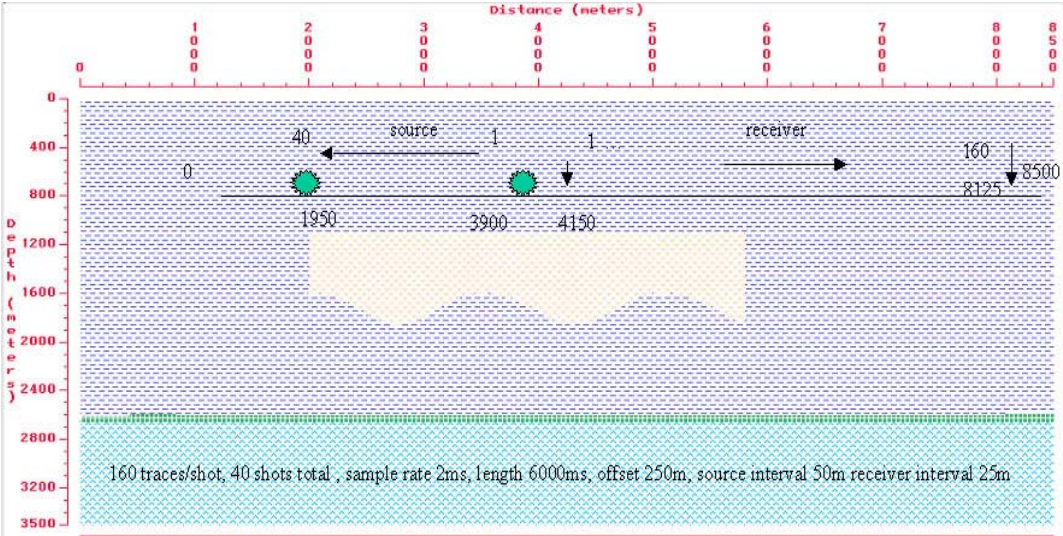


FIG. 2.22. Model and geometry of ray tracing modeling

Figure 2.22 shows a model with acquisition geometry, which is the same as Figure 2.15. A ray tracing shot gather is shown in (Figure 2.23 b). It is very similar to those observed in the physical modeling (Figure 2.23 a). Since we can control the events in ray tracing, it is helpful to identify the events in physical modeling data.

Even though ray tracing cannot produce the amplitude as accurate as physical modeling, it still can provide good amplitude for visual analysis. Some larger amplitudes beyond the critic angle are shown on Figure 2.23 (b).

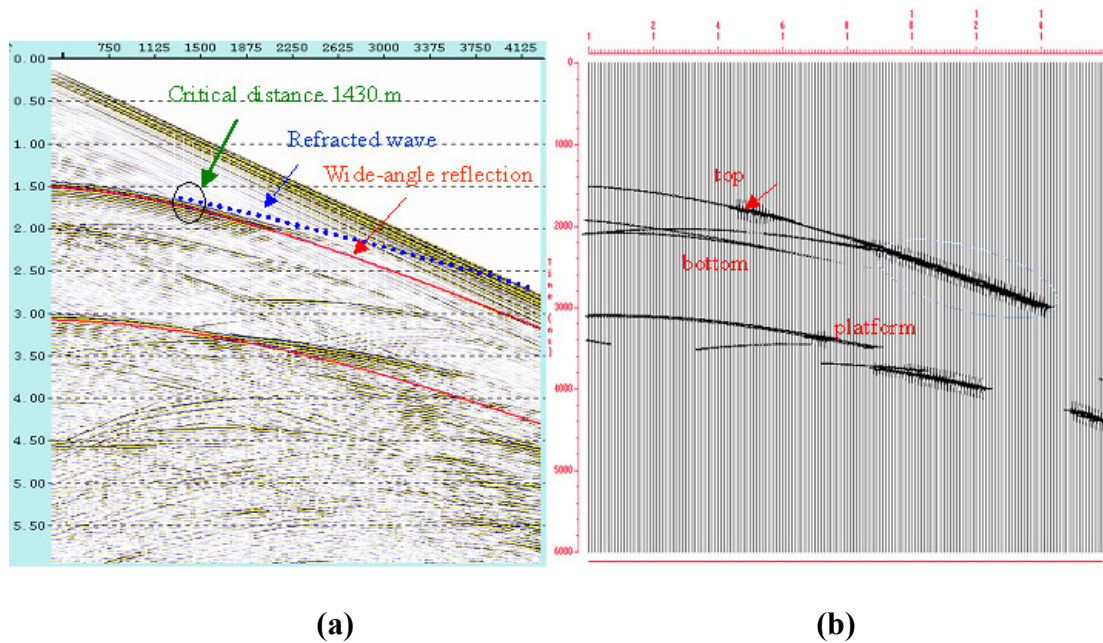


FIG. 2.23. Wide-aperture physical modeling data (a) compared to ray theoretical modeling data (b).

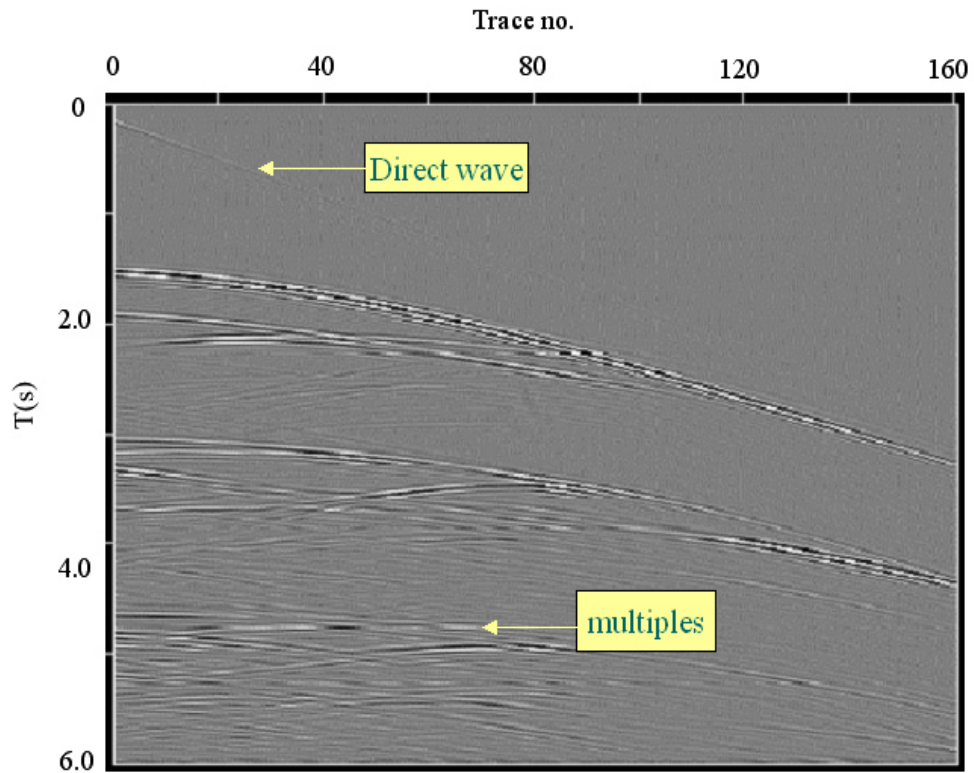


FIG. 2.24. Wave equation (finite difference) modeling. Direct wave and multiples are present.

I also used finite difference modeling (numerical simulation of acoustic wave propagation) to visualize the propagation of acoustic wave fronts and obtained some acoustic synthetic seismographs. A shot gather of modeling data is shown in Figure 2.24. The direct wave and multiples show up as expected. Physical modeling data did not show surface multiples because the transducers were deeply deployed into the water to avoid them.

## **FIRST ARRIVAL TOMOGRAPHY WITH DEFORMABLE LAYERS**

Seismic tomography is an inversion process where a velocity model is built based on seismic traveltimes or waveform data. It has been widely used in solving for near-surface static correction and deriving migration velocity model. It is a promising way of handling velocity gradient and lateral variation. For long-offset data, in order to avoid NMO induced artifacts, a newly developed Deformable Layer Tomography (DLT) algorithm was applied in this thesis to estimate the velocity model. Compared to grid-based first arrival tomography that inverts velocity distribution, DLT determines each interface's position by assuming that the layer velocity range is known. The results show that DLT is able to obtain reasonable velocity model based on the long-offset data.

### **3.1 Methodology**

First arrival traveltimes tomography uses traveltimes of the first-break to estimate the velocity model. Depending on the actual velocity structure, the first-break of seismic records may correspond to direct arrival, head wave, or turning wave. Conventionally, the model is parameterized by velocity grids. The tomography may be carried out by the following two main steps.

The first step is forward modeling. Traveltimes and corresponding raypaths are calculated for each source-receiver (s/r) pair. The traveltime measurements are connected to the model via the well-known traveltime integral

$$t(x, z) = \int_{raypath} 1/c(x, z) ds, \quad (3.1)$$

where  $c(x, z)$  is the velocity of the model. The raypaths that connect the source and receiver are related to the spatial distribution of the velocity field. The model is discretized by grid cells (Figure 3.1). The discrete form of equation (3.1) is

$$t_i = \sum_j l_{ij} s_j, \quad (3.2)$$

where  $l_{ij}$  is raypath length and  $s_j$  is slowness of the  $i^{\text{th}}$  ray segment within the  $j^{\text{th}}$  cell. The summation is over the cell visited by the  $i^{\text{th}}$  ray. Equation (3.2) is the practical forward modeling part of the first arrival tomography. Generally, traveltime is a non-linear function of velocity. It is difficult to directly invert the velocity field from equation 3.2.

Recasting equation (3.2) in matrix-vector notation

$$T' = L'S', \quad (3.3)$$

where  $T'$  is the observed data vector,  $L'$  is the  $M \times N$  raypath matrix (with element values equal to  $l_{ij}$ ),  $S'$  is the actual slowness model vector,  $M$  is the number of data, and  $N$  is the number of model variables.

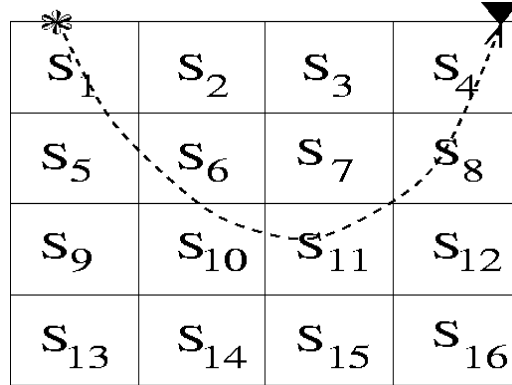


FIG. 3.1. Schematic diagram of a grid cells model (discretized into 16 cells).

For an initial guess model  $S$ , the predicted traveltimes vector  $T = LS$  can be used to form the perturbed traveltimes equation

$$T - T' = LS - L'S', \quad (3.4)$$

where  $L$  is the raypath matrix associated with the guessed model  $S$ . According to Fermat's principle, perturbation of traveltimes caused by changes in ray path is of second order or less. The first order perturbation of traveltimes is only caused by the

fluctuation of slowness along an undisturbed stationary raypath. The first order perturbation becomes

$$dt = Lds, \quad (3.5)$$

where  $dt = T' - T$ , and  $ds = S' - S$ . This equation is the linearization step where the higher order terms are omitted. This implicitly assumes that the segment lengths do not change much when the slowness model is slightly perturbed from the actual slowness model.

The second step is tomography inversion. The velocity is iteratively updated to generate a velocity model that provides an improved match with actual arrival times. Traveltime residuals are the input information for the second step. By adding perturbations to the initial model we obtain the refined model. One of the main principles in first arrival tomography is to find an inverse to the raypath matrix  $L$  in equation (3.5). There are many published works that discuss different solutions to such inverse problems.

For example, equation (3.5) can be solved by minimizing the sum of the square-errors subject to a length constraint on the slowness perturbation

$$\varepsilon = (Lds - dt)^T (Lds - dt) + \alpha ds^T ds \quad (3.6)$$

Minimizing equation (3.6) yields the damped least-square solution

$$ds = (L^T L + \alpha I)^{-1} L^T dt , \quad (3.7)$$

where  $I$  is the  $N * N$  identity matrix. Using the solution  $ds$ , the slowness model is updated by

$$S = S + \beta ds , \quad (3.8)$$

where  $\beta$  is the step length. If the initial model is very close to the actual model so that the traveltimes are truly linear, then  $\beta=1$  and equation (3.5) is the final answer. One can use equation (3.5) for a new starting model and repeat the same steps toward a new updated model. This procedure is repeated until convergence of the model and the traveltimes residual (Figure 3.2) is achieved.

Compared to grid-based first arrival traveltimes tomography, the DLT combines the effect of interface position change with velocity variation on the traveltimes perturbation. The perturbation equation is

$$\delta t_i = \sum_j^J a_{ij} \delta s_j + \sum_k^K b_{ik} \delta x_k , \quad (3.9)$$

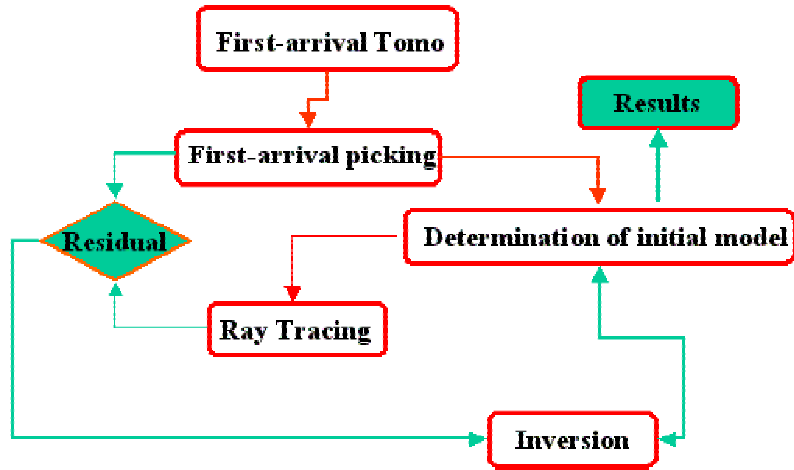


FIG. 3.2. A flow diagram of first arrival tomography.

where  $J$  is the number of slowness blocks,  $K$  is the number of interface nodes,  $\delta t_i$  is the travelttime residual of the  $i^{\text{th}}$  ray,  $\delta s_j$  is the slowness perturbation of the  $j^{\text{th}}$  block,  $\delta z_k$  is the perturbation of coordinates of the interface position nodes of the  $k^{\text{th}}$  interface;  $a_{ij}$  is the slowness kernel, which is the length of the  $i^{\text{th}}$  ray in the  $j^{\text{th}}$  block, and  $b_{ik}$  is the depth kernel.

The DLT model is parameterized by many layers with variable thickness, each of which consists of many constant-velocity blocks (Figure 3.3). The geometry of the model blocks is a trapezoid in 2-D and triangular lens in 3-D. Using the known

velocity, the DLT seeks to determine the depth of the top and bottom surfaces of the blocks by minimizing traveltimes residuals of all traversing rays.

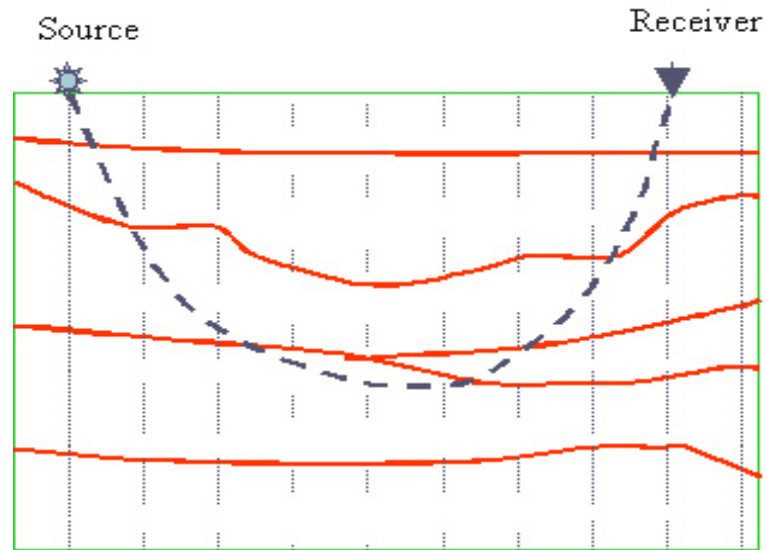


FIG. 3.3. Schematic diagram of a DLT model. Dashed line is a ray path.

Zhou (2003) has shown that the inverted velocity model by DLT is more geologically plausible than the conventional method using a grid-cell model (Figure 3.4). It significantly reduces the along-raypath smearing artifact.

Figure 3.4 shows a comparison of the results of applying conventional grid-based tomography and the DLT on a 2-D synthetic model based on a previous model of real data (Zhou, 2003 a). The true model contains 12 seismograph stations (green

triangles) and 12 earthquakes (red stars). The top boundary of the bottom layer is the Moho. Treating the first arrival traveltimes in the true model as data, each tomographic method attempts to recover the true model using raypaths in the reference model and traveltime residuals between the true model traveltimes and reference model traveltimes. Starting from the same initial reference model with flat layers as shown in Figure 3.4 (c), the DLT resulted in Figure 3.4 (d), and the grid-based tomography resulted in Figure 3.4 (e). The DLT solution is very similar to the true model as depicted by the dashed curves, though only 12 events are used here. The DLT model differs from the true model at places of poor ray coverage, such as the right side of the fourth interface from the top. In contrast, the grid-based tomography model in Figure 3.4 (e) contains some serious artifacts. The irregular surface of the Moho in the true model appears as a strong horizontal velocity discontinuity because grid-block geometries are fixed in space. As a result, the Moho depth estimates are too shallow, and a horizontal low-velocity layer artifact has been created in the lower crust on the right side of the panel. Also, many high-velocity, column-like anomalies in the middle and upper crust are parallel to the raypaths, which suggests that they are smearing artifacts along raypaths. The DLT algorithm suppresses such smearing artifacts.

Figure 3.5 shows a synthetic test using 12 shots with 30 receivers for each shot. The left top of the figure is the true model; the initial model (in the middle of left) was

parameterized by five flat layers with 18 blocks (nodes) in each layer. The layer velocities used are 1500, 2500, 3500, 4000, and 4500 m/s, respectively. After the 4<sup>th</sup> iteration the inverted result (Figure 3.5 right bottom) is very close to the true model within the ray coverage range.

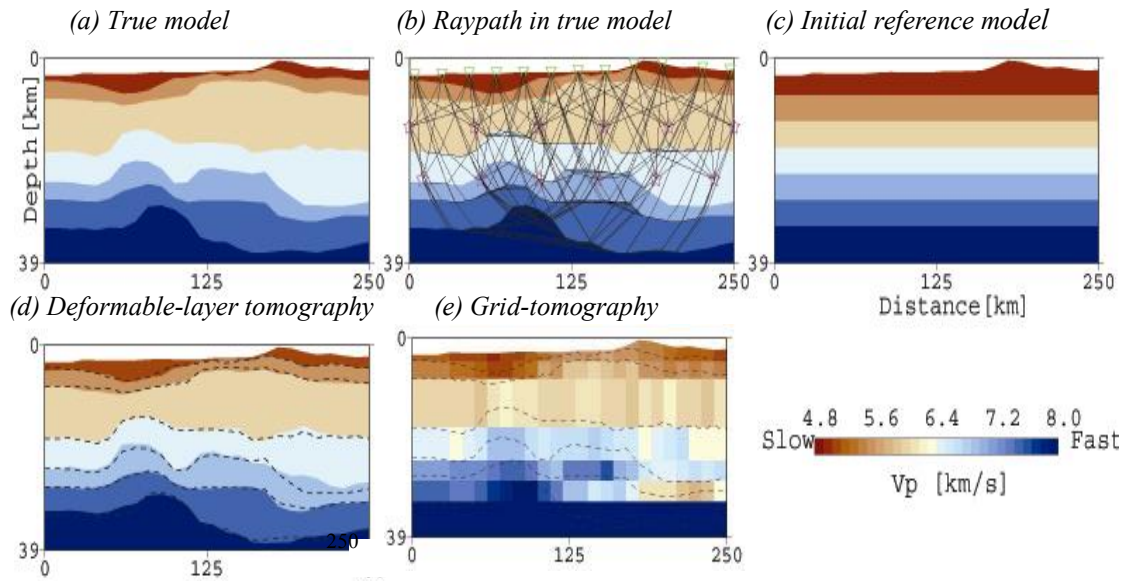


FIG. 3.4. A 2-D synthetic comparison between the new deformable-layer tomography (DLT) and the conventional grid-based tomography. (a) True velocity model in the DLT system. (b) Raypaths in the true model from 12 hypocenters (purple stars) to 12 seismographic stations (green triangles). (c) Initial reference model. (d) Solution of the new DLT. (e) Solution of a grid-based tomography. The vertical exaggeration is 3 to 1. The dashed curves in (d) and (e) depict the velocity contours of the true model (Zhou, 2003 a).

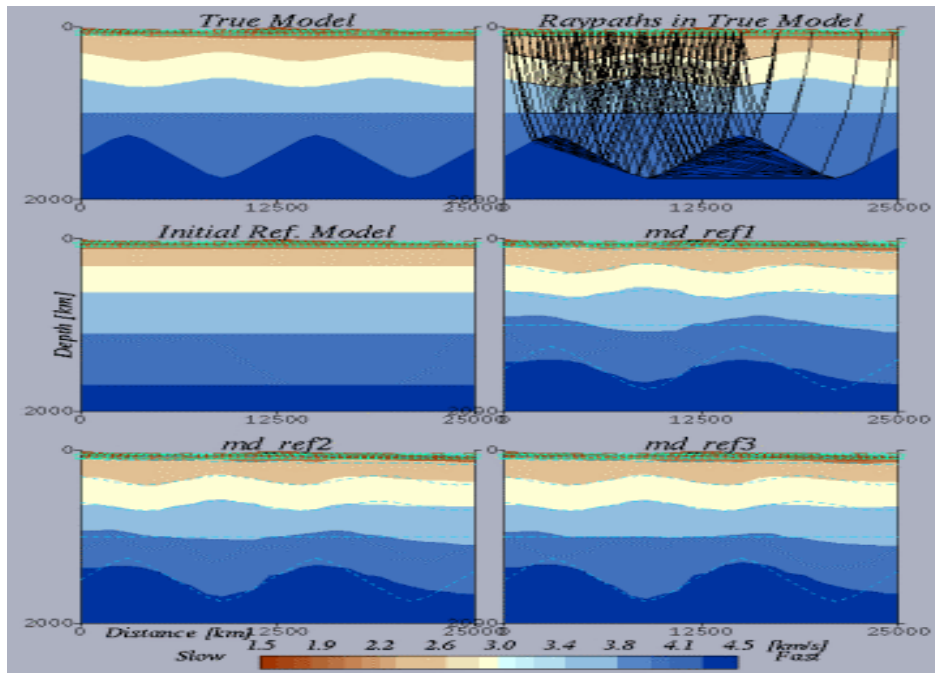


FIG. 3.5. DLT using synthetic data. After the 4<sup>th</sup> iteration the inverted result (bottom of the right panel) is very close to the true model within the ray coverage range (top of the left panel).

### 3.2 Application to 2-D crooked line field data

#### 3.2.1 Data set

The data used is a 2-D crooked line (Figure 3.6) that was acquired a seismic sounding survey near the southern edge of Tarim basin, China. The line has very irregular

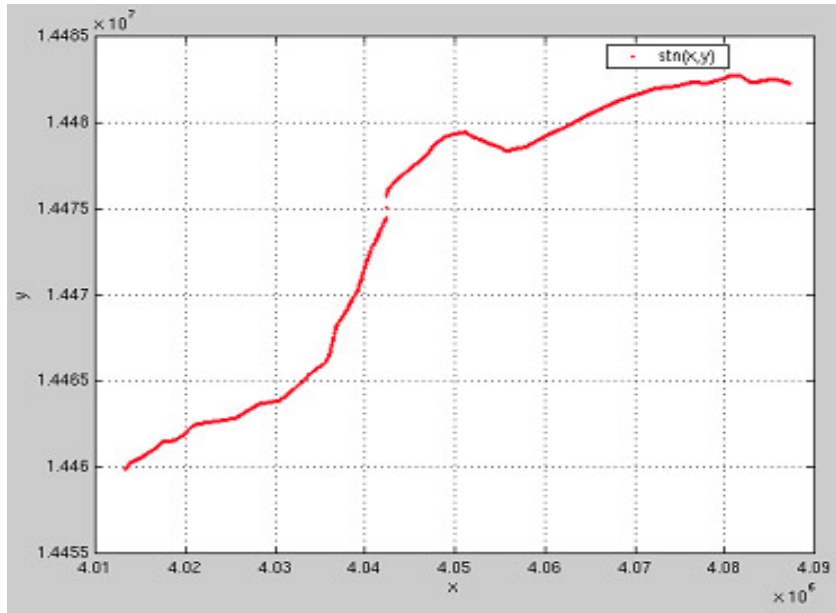


FIG. 3.6. A map view of survey stations.

acquisition geometry in terms of shot and receiver locations and spread types. A dynamite source was used; each shot has 300-432 channels with either split spread or off-end spread. The quality of the raw records varies dramatically. Offset ranges from 8 to 19 km. The length of records is 30 seconds with a sampling interval of 2ms. The crookedness and the long cable lead to the strong multiple refractions and other surface linear events. The surface has a regional slope of 0.02.

### **3.2.2 First arrival picks**

The first trough that immediately follows the true first break of the waveform is defined to be the first arrival for picking. Traveltime was picked interactively in FOCUS/DISCO system by using a neural network algorithm. Between offsets of approximately 2.5 km and 10 km, most first arrivals exhibit a smooth decrease in ray parameter. It implies the presence of a continuous velocity gradient. At certain depths, there are local low-velocity anomalies in some shots near the north end of the line. I exported the traveltime file from the FOCUS/DISCO database and reformatted it to fit the input format of the DLT codes. Data editing was applied to discard some bad picks.

### **3.2.3 Crooked line geometry rebinning**

To enable a better correlation of the seismic rays with the surface geology, shot and receiver coordinates of each pre-stack trace were projected to a straight line (Figure 3.7) by geometry rebinning process.

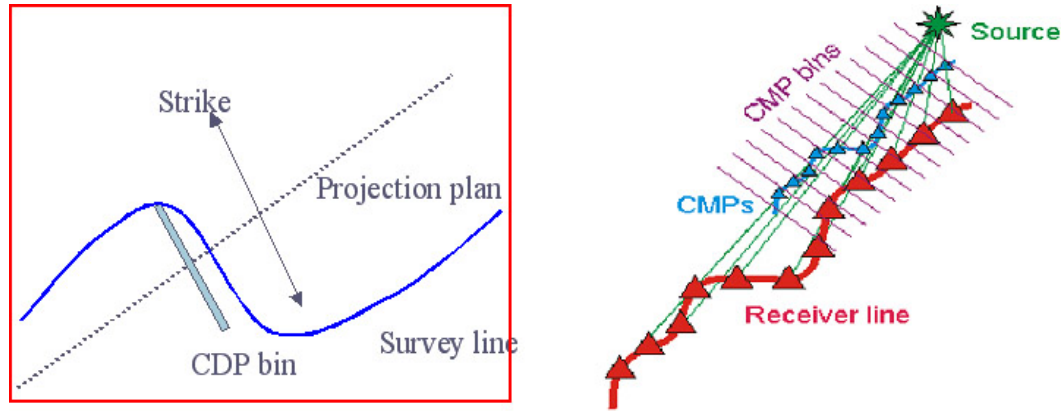


FIG. 3.7. Schematic diagram of CMP rebinning. The shot and receiver coordinates were projected to a straight line.

### 3.2.4 Reference velocity model

Since the DLT is sensitive to the initial model, the building of the reference model plays a major role in the accuracy, convergence and resolution of the final solution. For efficient topography inversion, the initial velocity model should reflect the general structure of the studied area. I constructed a 1 D initial velocity model based on gradient information in traveltimes data.

### 3.2.5 Data QC for accuracy and consistency

Geometry errors could result in instability of the final tomography solution. In order to assure the reformatted geometry is correct, I matched the traveltimes with geometry before and after CMP rebinning (Figure 3.8) for identifying the outliers. Figure 3.8 shows matching plots of traveltimes with location before (Figure 3.8, b) and after (Figure 3.8, a) CMP rebinning process.

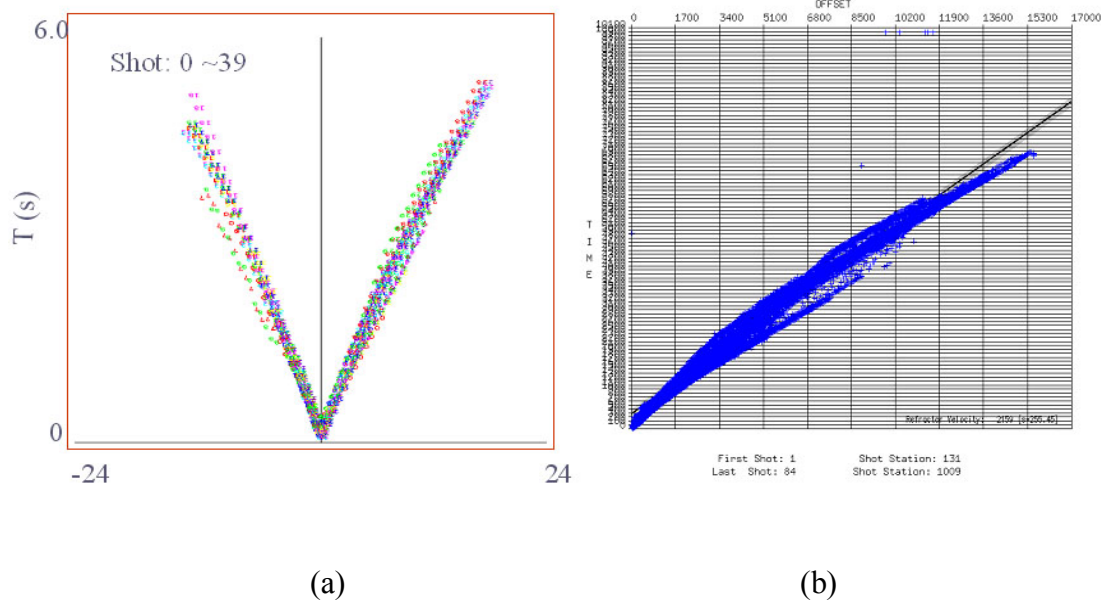


FIG. 3.8. Matching plot of traveltimes with locations before (b) and after (a) CMP rebinning.

### 3.2.6 DLT

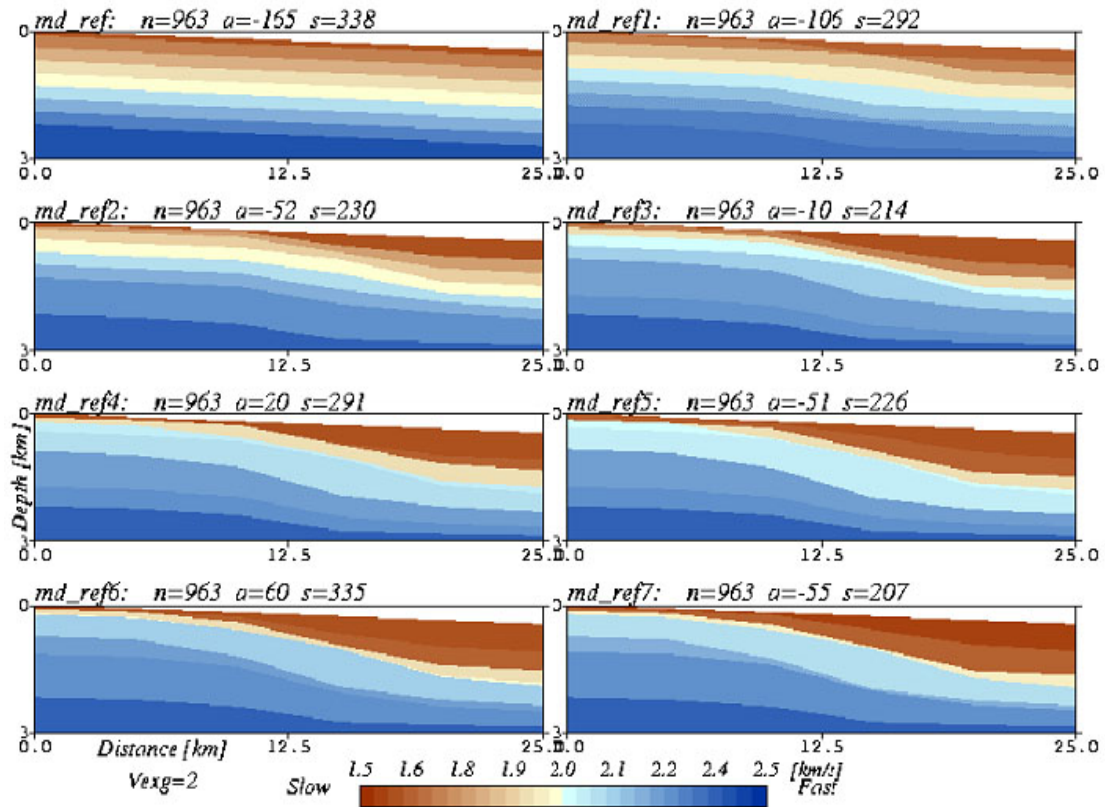


FIG. 3.9. Tomographic inversion of 7 iterations. Here  $n$  is the number of rays,  $a$  is the traveltime residual average, and  $s$  is the standard deviation.

Raytracing and inversion are the two main steps for the DLT. I obtained the computed traveltime and raypath to form the inversion equation. The inversion is an interactive process as described in Section 3.1. Zhou's DLT code was used in this study.

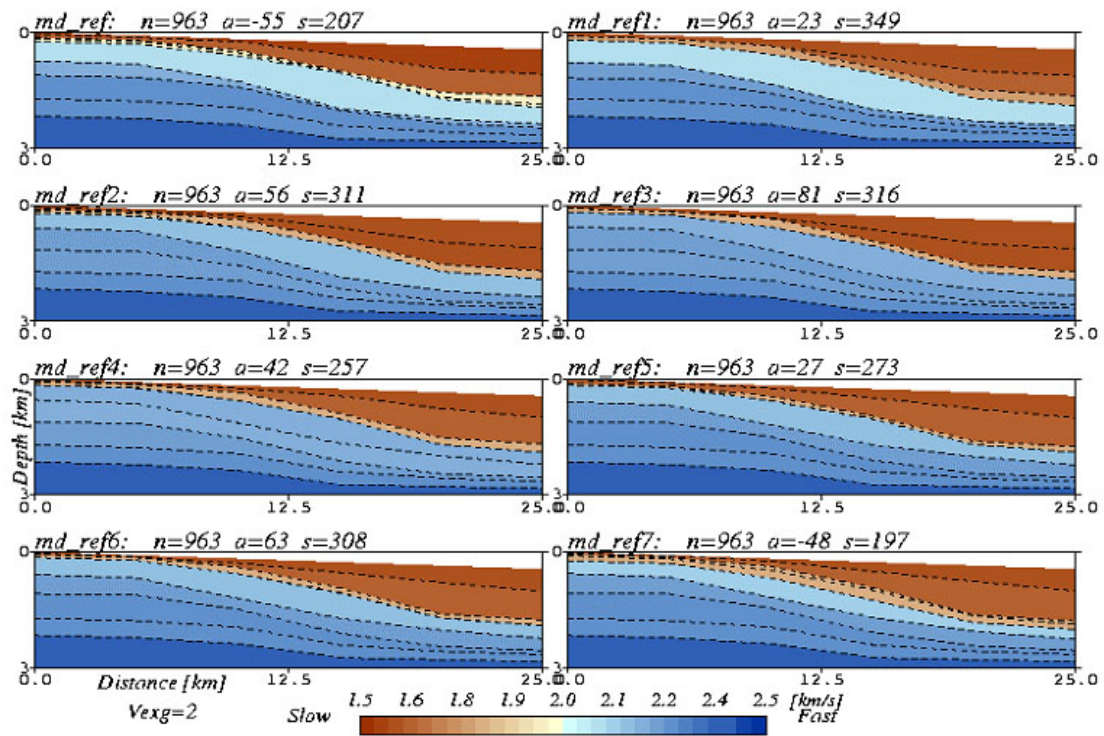


FIG. 3.10. Another 7 iterations using first 7<sup>th</sup> iteration result as a reference model.

I cut the line into two segments and used 48 shots of the southwest segment data to invert the velocity model. The dimensions of the model are 25 by 3 km. Figure 3.9 shows 7 iteration results, where *n* is the number of rays, *a* is the average of the traveltime residuals, and *s* is the standard deviation. A negative traveltime residual indicates that traveltime is delayed relative to the reference model. On the other hand, a positive residual indicates that traveltime is advanced. The standard deviation is a measure of the data fitness. Figure 3.10 gives the results of another 7 iterations using the first 7<sup>th</sup> iteration result as a reference model. After 7 iterations (Figure 3.9) the

traveltime residual average and standard deviation were reduced from  $-165$  and  $338$  ms to  $-55$  and  $207$  ms. Another 7 iterations only improved the residuals slightly (Figure 3.10).

Several factors may lead to unreliable and/or non-unique tomography inversion. The curvature of the line results in scattering of CMPs in both the inline and cross-line directions. Irregular geometry, such as inconsistent fold coverage, uneven offset distribution, or low subsurface CMP coverage (a line of length of 75 km only has 84 shots) could impair the CMP based processing. The inclusion of cross dip in the subsurface will also increase the degree of non-uniqueness of the solution.

The best way to tackle the crooked line tomography problem would be 3-D traveltime calculation that treats shot and receiver coordinates in 3-D or 2.5D. The inversion procedure is done in 2-D, and the velocity field is projected to an inline 2-D section that is chosen along the dip direction of the geological structure.

Despite many uncertainties, the inversion results seem to agree with the regional geology approximately. Figure 3.11 is a layer-based first arrival tomography for the data acquired across the southern edge of the Tarim Basin, China. Starting from an equal-thickness initial reference model shown in the top panel, the result of DLT is

shown in the bottom panel. Thickening of near-surface lower velocity layer toward the basin is clearly shown.

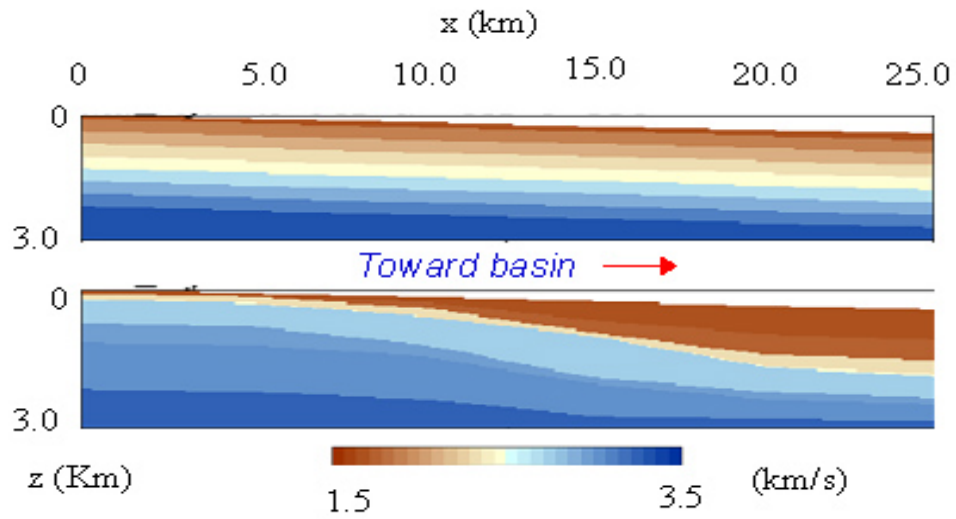


FIG. 3.11. A first arrival tomography with deformable layers for a field dataset across the southern edge of Tarim basin. The top graph shows initial reference model with equal-thickness layers, while the bottom graph shows the inverted velocity model.

## MIGRATION OF PHYSICAL MODELING DATA

This chapter deals with migration of long-offset physical modeling data. Because of the poor data quality, much of the emphasis was placed on pre-processing of the data.

### 4.1 Data pre-processing

#### 4.1.1 Deterministic deconvolution

The source signature of the physical modeling is still very ringy. The ringing severely degrades the resolution of the subsurfaces (Figure 4.1). To reduce the ringing, I applied deterministic deconvolution to the shot gathers as shown in Figure 4.2 and 4.3.

The deterministic deconvolution is generally represented by

$$x[n] * f[n] = d[n] + n[n],$$

where  $x[n]$  is the input data,  $d[n]$  is the desired output,  $f[n]$  is the inverse of the wavelet, and  $n[n]$  is noise. Figure 4.2 (a) shows a decimated input data (every 10<sup>th</sup> trace). Figure 4.2 (b) is the output of the deterministic deconvolution. The effects of

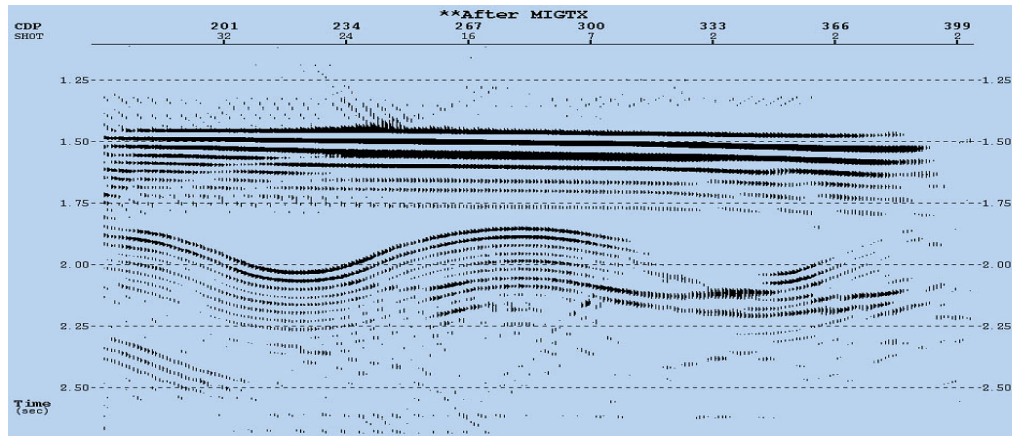


FIG. 4.1. Post-stack migration of a 2-D physical modeling line.

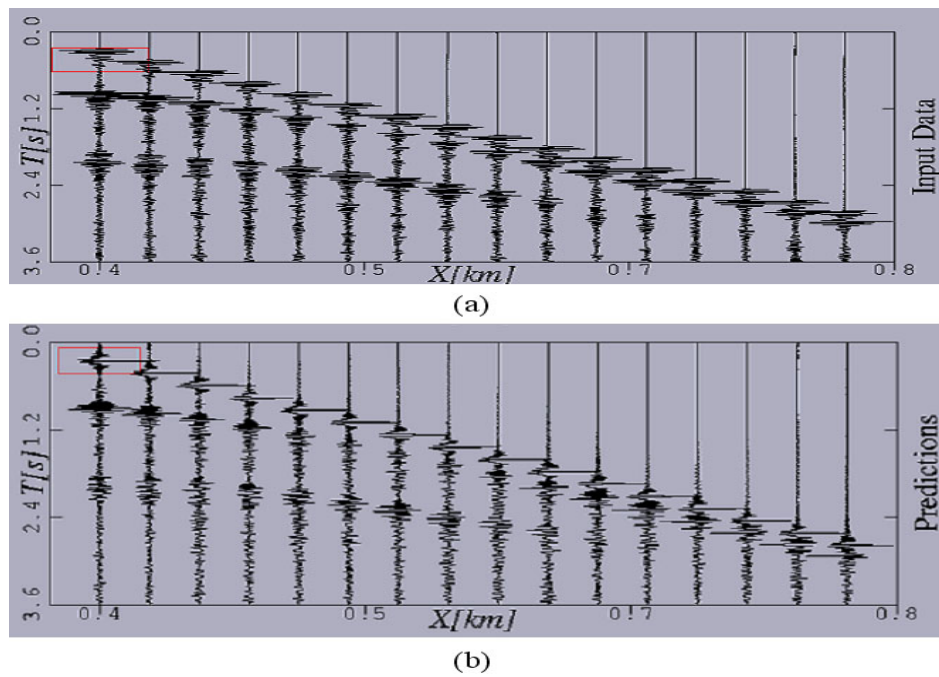


FIG. 4.2. Shot gather (a) before and (b) after deterministic deconvolution. Every  $10^{\text{th}}$  trace is shown.

the deconvolutions are different between different events. The first arrival is obviously spikier than other events. This is because the wavelet is picked from the first arrival. Deconvolution can also be used to compensate for the directivity of the transducer. Krail and Shin (1990) proposed a method to compensate for directivity of transducers. They used deconvolution to remove the directionality of a source signature. Compared to the data before deconvolution (Figure 4.3 a), the resolution of data after deconvolution (Figure 4.3 b) was greatly improved.

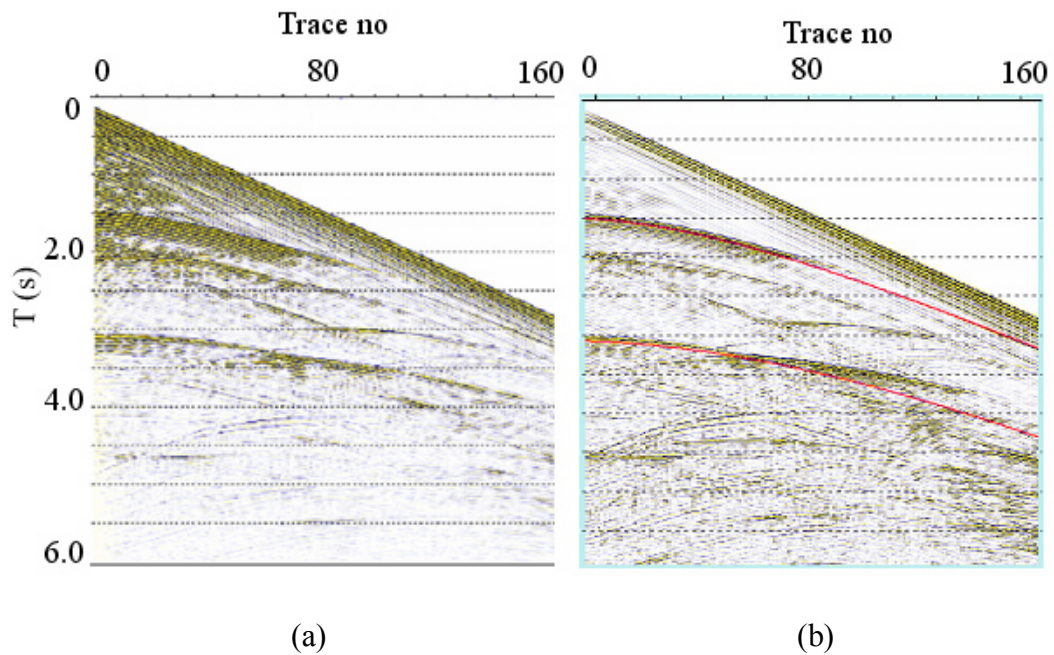


FIG. 4.3. A shot gather (a) before and (b) after deterministic deconvolution, all 160 traces are shown.

### 4.1.2 $\tau$ -p filtering

Physical modeling data are always contaminated by source-generated noise (Figure 4.4), such as direct wave and linear coherence noises. In the x-t domain, due to the interferences between noises and desirable events on the shot gather, it is hard to get satisfactory results by the conventional filtering or a surgical muting procedure.

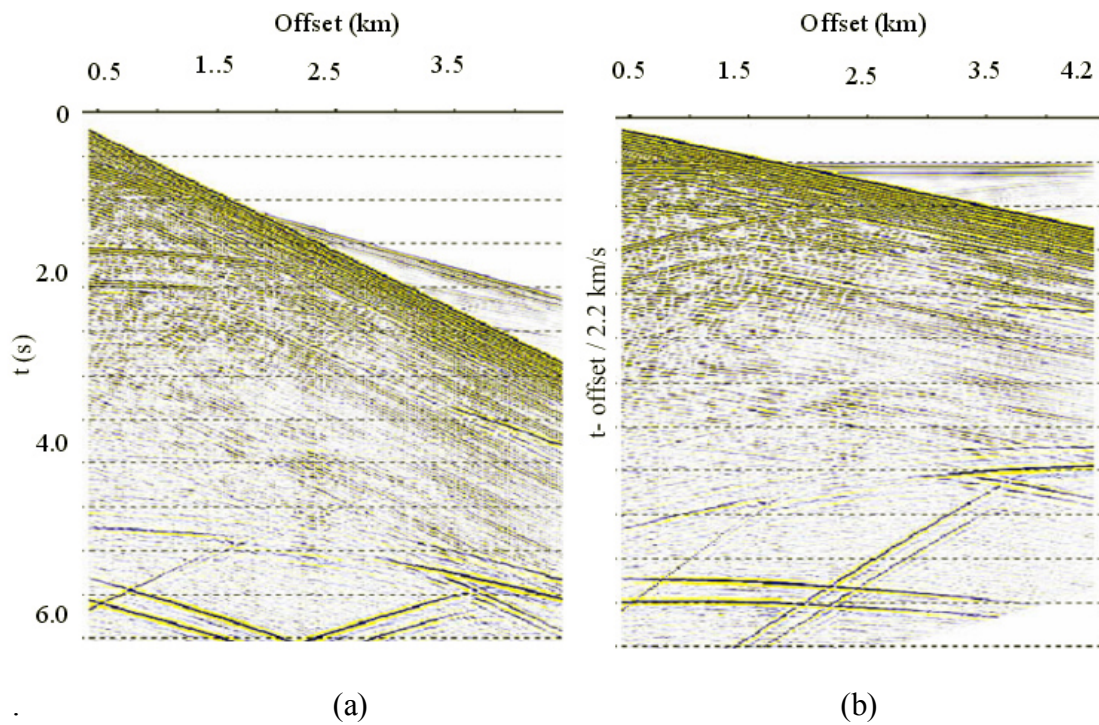


FIG .4.4. Using  $\tau$ -p transformation to remove linear events: (a) Shows raw data after T-gain; (b) shows the data after applying linear moveout correction.

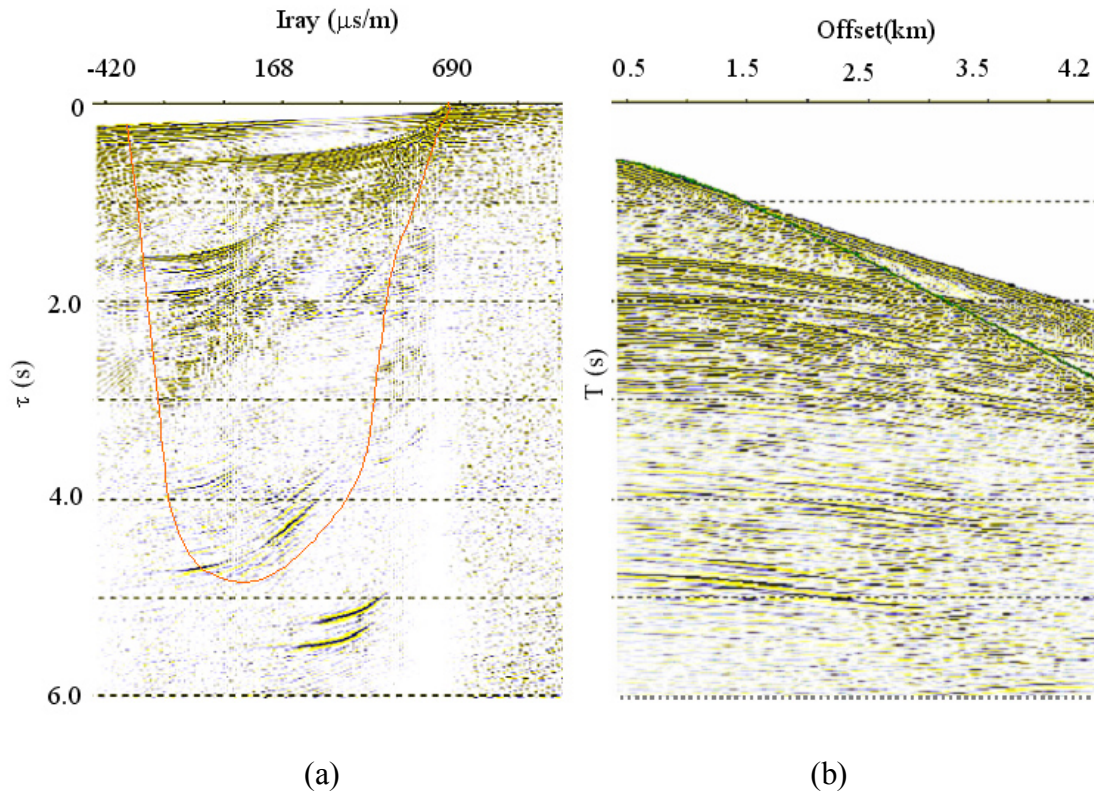


FIG. 4.5. Using  $\tau$ - $p$  transformation to remove linear events (continued): (a) Linear  $\tau$ - $p$  transformation applied to Figure 4.4 (b); (b) reverse  $\tau$ - $p$  transformation of the filtered data (a).

Event though there are some published works dealing with source-generated noises by separating or filtering, such as migration filtering (Nemeth, 2000) in the  $x$ - $t$  domain, they all required heavy computation; however, transformation of data from  $t$ - $x$  to  $\tau$ - $p$  domain offers advantages of event separation. We can easily reject unwanted events in

the  $\tau$ -p domain. Generally only some mutings are required in the  $\tau$ -p domain to reject source-generated events. The procedure is as follows:

First, a linear move out is applied to flatten the events in the x-t domain (Figure 4.4 b). The flattened gather is transformed into the  $\tau$ -p domain (Fig 4.5 a), which maps the direct arrival to the point near  $p=0.67$  ms/m. Most of slow traveling coherent noise and direct arrival energy can be separated in the  $\tau$ -p domain. A mute is applied to remove these noises. Finally, the inverse  $\tau$ -p transform is applied to transfer the noise-reduced data to the x-t domain (Fig 4.5 b).

## **4.2 Kirchhoff pre-stack depth migration**

Kirchhoff migration is the most commonly used migration algorithm in the oil and gas industry for many years. Currently it is still the fastest method of pre-stack depth migration. An essential part of Kirchhoff migration is the computation of traveltimes of seismic waves between every source and receiver. Conventional Kirchhoff migration methods use fast but simple methods to compute traveltimes. These methods provide excellent results in simple structure. But they are not good enough in complex areas, such as subsalt, where ray paths may go through multipathing or other complicated processes. To improve the imaging capability of Kirchhoff methods, various schemes have been developed, such as wavefront constructions and multiple-

arrival Kirchhoff methods. In this work, a most energetic pre-stack Kirchhoff depth migration was used to migrate a 2-D line of physical modeling data (Figure 4.6).

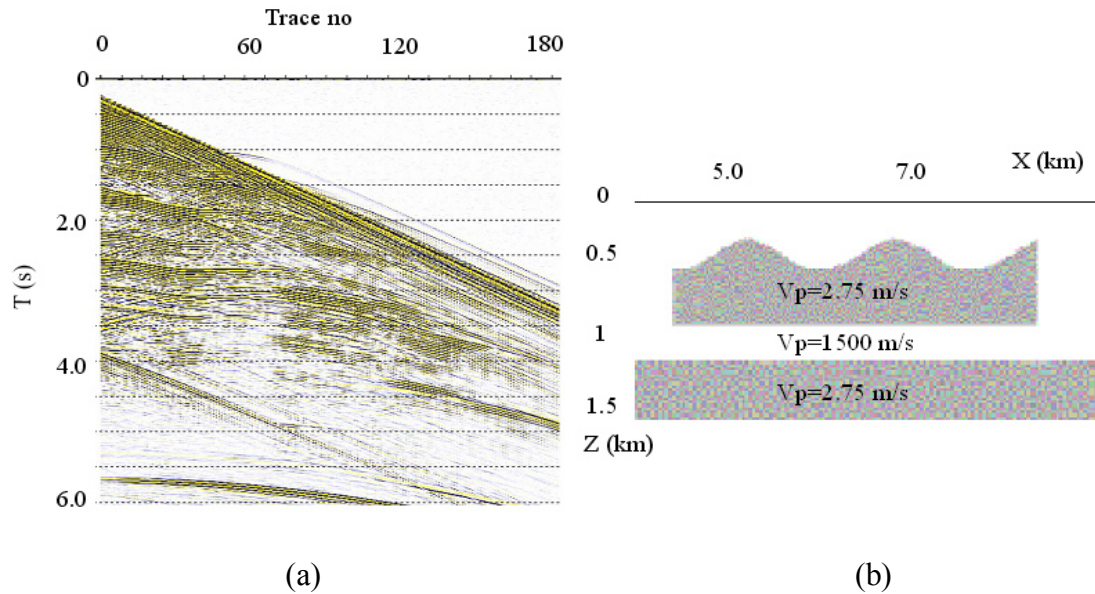


FIG. 4.6. A shot gather (a) and a 2-D view of the model (b) (only part of model is shown).

The model has dimensions of 12 by 4 km in x and z directions. I sampled the model with an interval 10 m, so the grids have 1201 by 401 points. The model contains 4 interfaces, the top one featured two anticlines and two synclines, and the other interfaces are flat. The velocity of the model material (Plexiglas) (black color in Figure 4.6 b) is 2750 m/s. The first shot was located at  $x=3.9 \text{ km}$  and the last shot was at  $x=1.95 \text{ km}$ , with a shot interval of 50 m. I modeled 40 shots. Each shot has 180

traces with a group interval of 25 m. The nearest offset is 250 m. Each trace has 3500 samples with a sample interval of 2 ms.

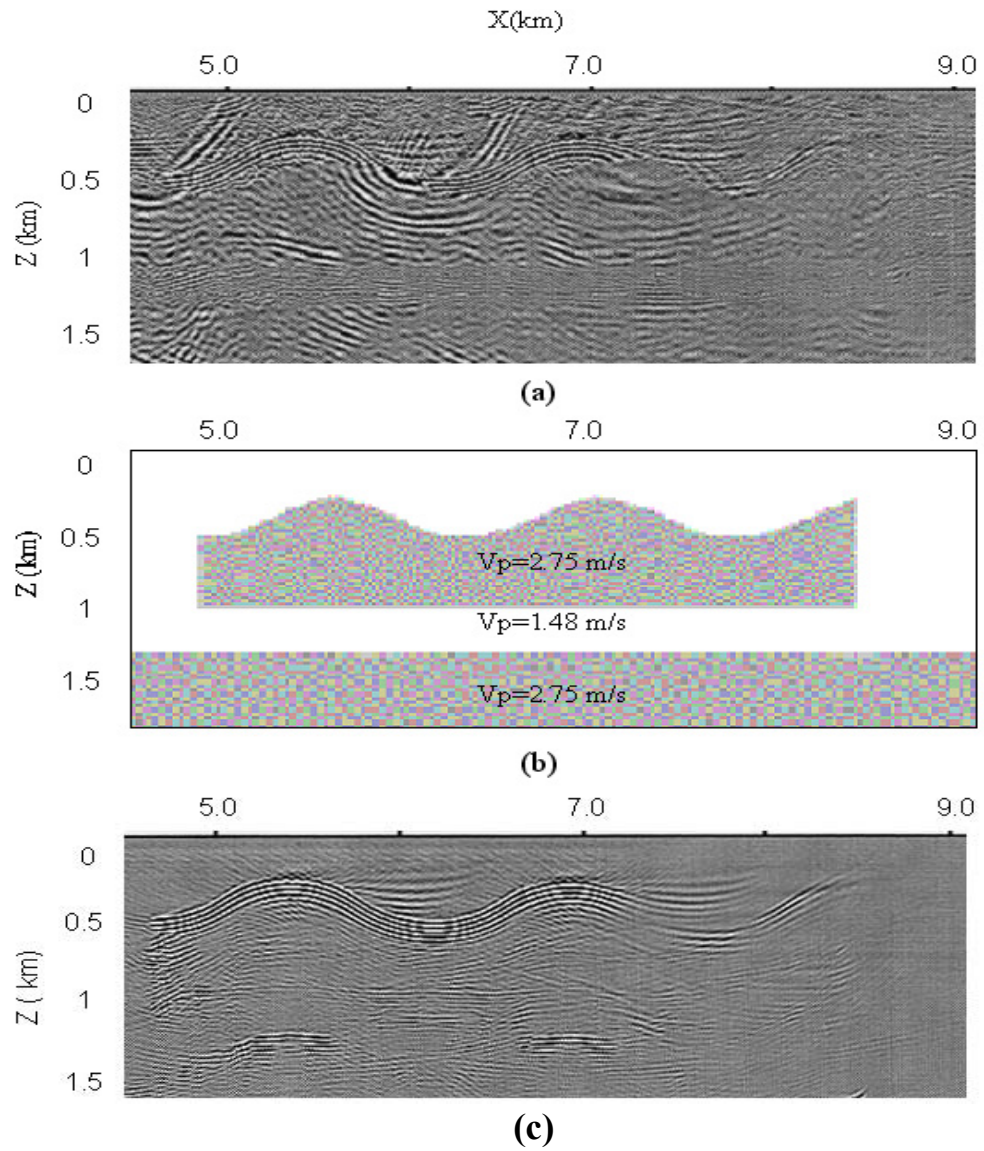


FIG. 4.7. Geometry mis-positioning effect: (a) Image with a measured geometry; (b) 2-D view of the physical model; and (c) image with adjusted geometry.

Figure 4.7 (b) is a 2D view of the velocity model. Figure 4.7 (a) is a brute image with an origin-measured geometry. There are many apparent artifacts around the corner, the trough and the boundaries, where large velocity contrasts are present. After the geometry was adjusted, I obtained the image result shown in Figure 4.7 (c). The image of the top surface was improved but the image of the underlying became worse. I conclude that the mis-positioning error of the source and receiver from the physical modeling experiment, which resulted in a velocity error, may be a major factor that affects the image quality.

### **4.3 Reverse-time pre-stack depth migration**

Reverse-time pre-stack depth migration algorithms were used to migrate 2-D long-offset physical modeling data acquired from a 3D physical model, which is a piece of Plexiglas with flat surface on the top and curve surface on the bottom (Figure 4.8). The reverse-time migration is based on the symmetry of the acoustic wave equation. I used a finite-difference scheme to backward extrapolate the recorded wave fields and to forward model the predicted wavefield. The algorithm consists of the following steps: (1) computation of the forward propagated wave field from the shot to all grid points; (2) computation of the backward propagation of the reverse-time records; (3) construction of the depth image by cross-correlation of all forward-propagated fields with all back-propagated wave fields; (4) application of imaging enhancement. Since

it is based on the two-way elastic wave equation, it can handle multiples and converted waves etc.

The data was collected with 160 traces per shot, and 40 shots per line. The shot spacing was 50 m, and the receiver spacing was 25 m. The offset ranges from 250 to 4225 m. The migration was over the 851 by 396 grid, including the absorbing boundary. Figure 4.8 is a 2-D view of the model. Figure 4.9 (a) shows the migration result using raw physical modeling data. The coordinates of the image are corresponding to the original physical modeling coordinates. Based on the same model, an acoustic finite difference modeling technique was used to generate numerical modeling data. The same migration was conducted on the numerical data (Figure 4.9 b). The Plexiglas was imaged well both in the physical model data and the numerical model data; however, some features of the images are inconsistent, especially the artifacts. In the physical modeling image, the direct energy effect is strong. There are also evidences of multiple-induced artifacts, such as the flat events inside the Plexiglas that are stronger in the physical modeling image than in the numerical modeling image. The right parts of the image from the physical modeling data are not as clear as the numerical data image; the background noises are also different. This is probably because: (1) off-line scattering of 3-D physical modeling data were processed in 2-D; (2) the mis-positioning error in physical modeling

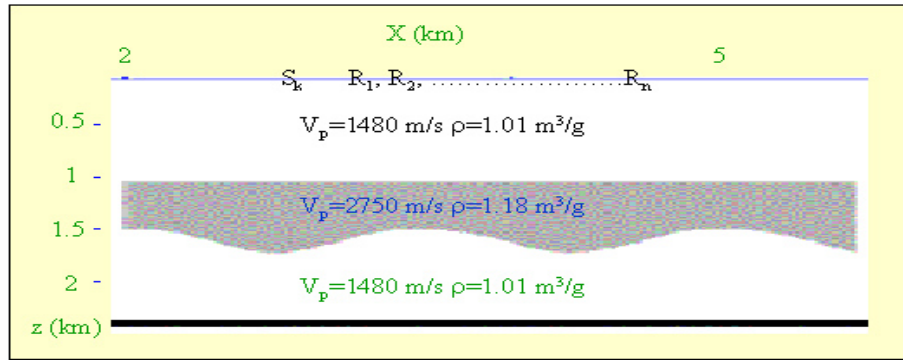


FIG. 4.8. A 2-D view of the physical model.

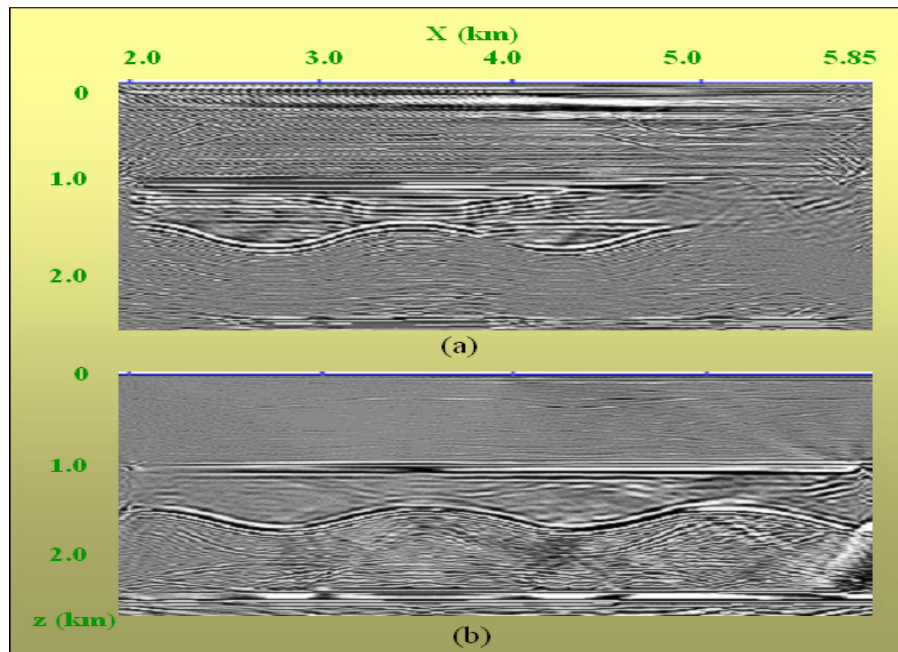


FIG. 4.9. Reverse-time depth migration of the physical modeling data (a) and numerical modeling data (b).

data, since small errors in geometry measurements would exaggerate the positions deviation after 10000 scaling up; (3) the physical modeling data contain colored noises, such as source-generated noise, and direct arrivals; and 4) the mismatch between the source wavelet of the physical modeling data and the Ricker wavelet used in the reverse-time migration. The numerical data image has some high frequency ringing noises that seem to increase with depth. This is probably caused by under-sampling of the numerical data.

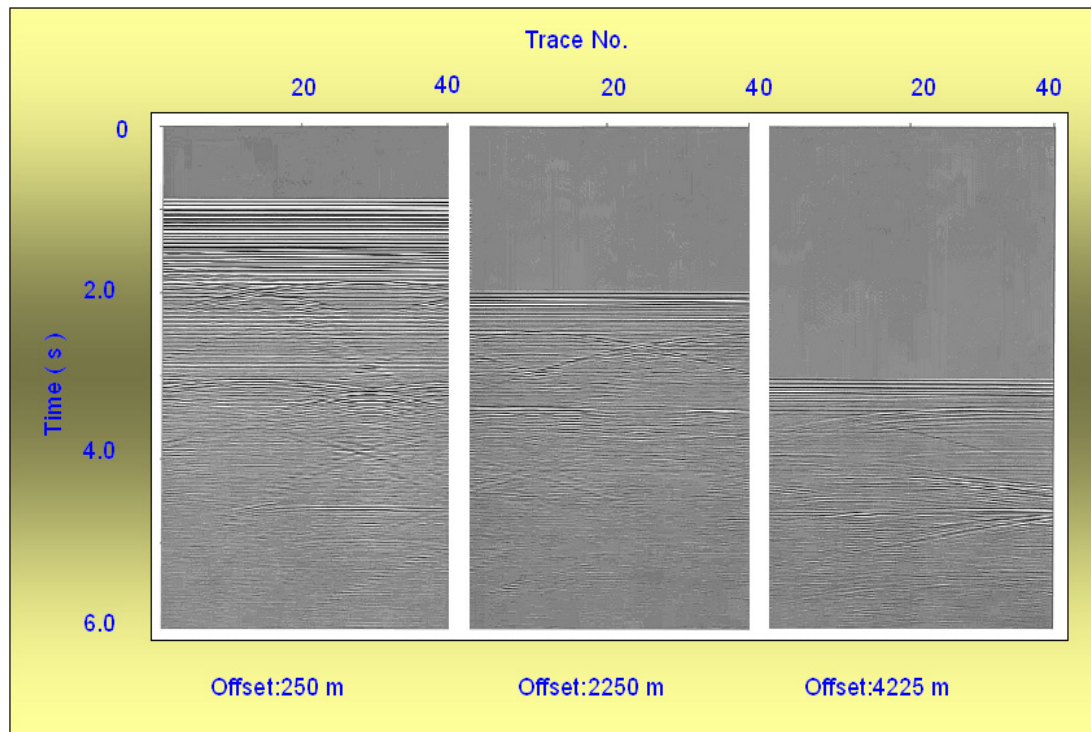


FIG. 4.10. Common-offset sections: (Left) offset=250m; (Middle) offset=2250 m; and (Right) offset=4225 m.

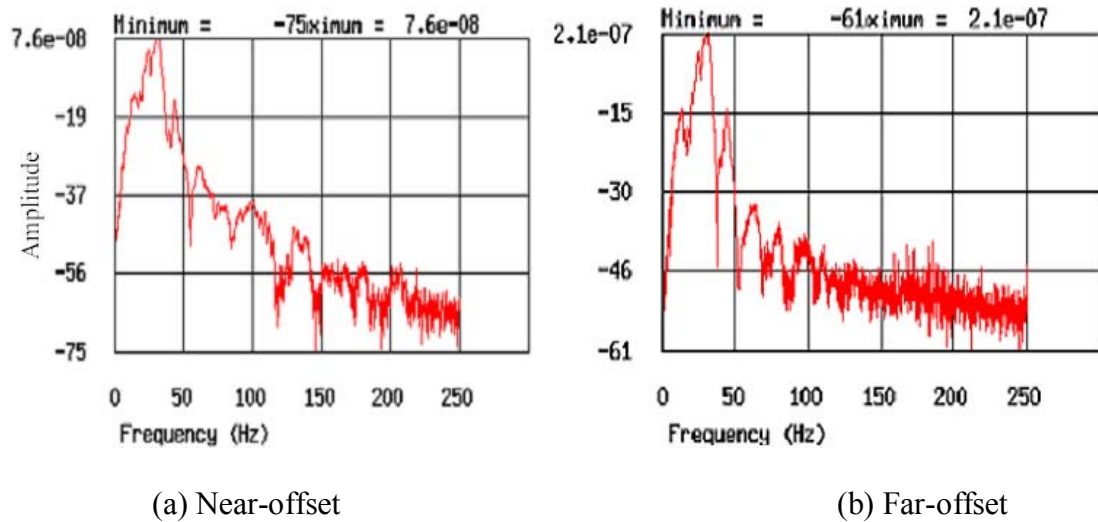


FIG. 4.11. Spectrum comparison of the near and far-offset physical modeling data.

Figure 4.10 shows an example of three common-offset sections. Though the events at farther offset are more squeezed together, the frequency content is not degraded much at far-offset (Figure 4.11). In contrast, the field data would show significant decrease in frequency at far-offset due to attenuation effects.

I have also migrated different offset ranges of the physical model data. Pre-stack depth migration was applied to several subsets of the physical model data with different offset ranges. Figure 4.12 compares two such migration results. One of them has offset ranges from 225 to 2125 m, and the other from 2000 to 4225 m. The images

from the far-offset and near-offset traces show some interesting differences. Although the long-offset image is noisier and has poorer resolution of the horizontal interfaces

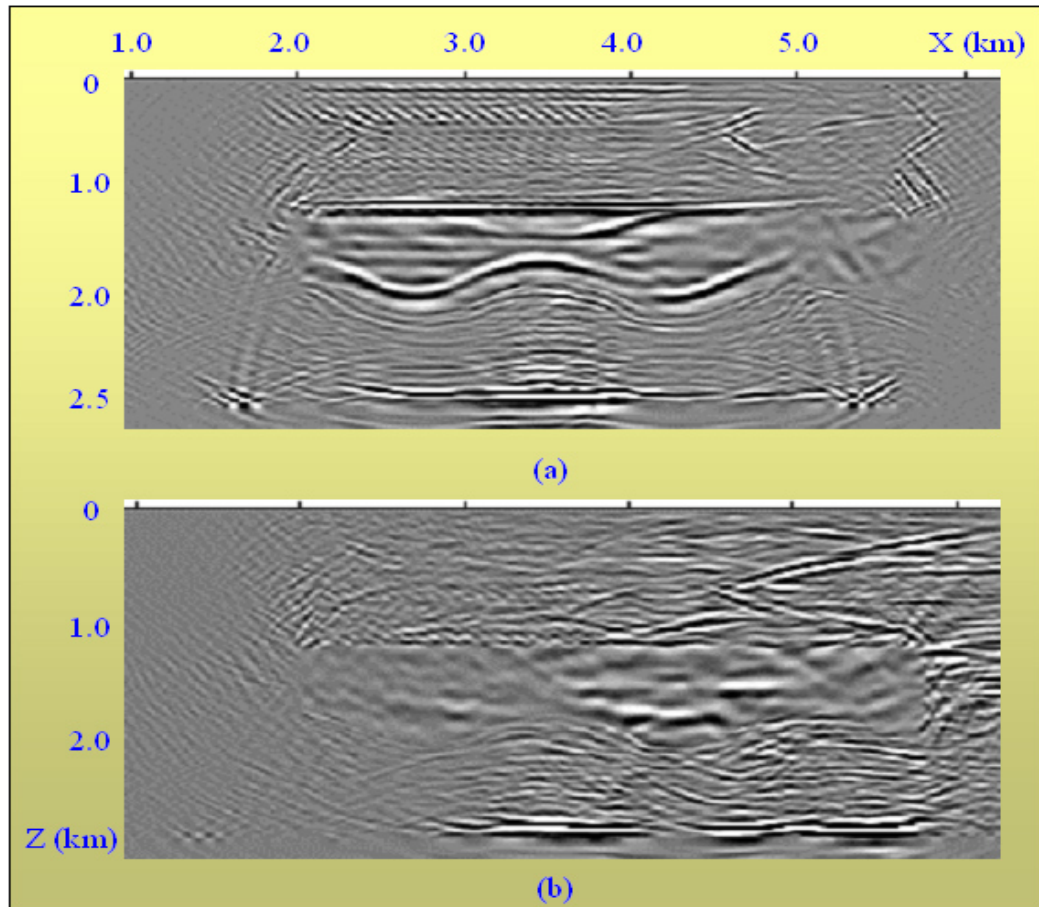


FIG. 4.12. Pre-stack depth migrations of (a) near-offset data and (b) far-offset data.

it provides improved illumination of the vertical boundaries. For the interfaces between water and Plexiglas, which are similar to the property of a salt boundary, the long-offset image has less ringing and is better defined by the difference in the

frequency of the image across the interface. It is also noticed that the reflectivity at the interface of the Plexiglas is considerably weaker in the far-offset image, but the interface is better defined by the difference of frequency between the two sides of the interface.

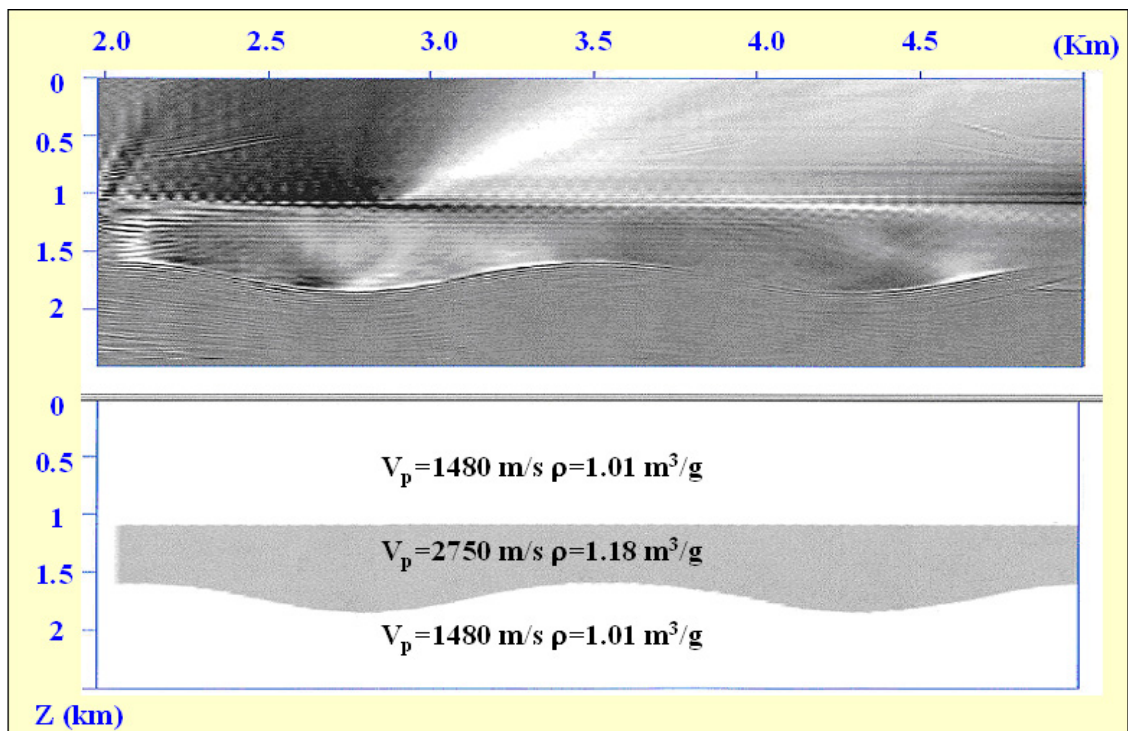


FIG. 4.13. Final image of reverse-time migration using full-offset data with some pre-conditioning processes.

Since we were focusing on comparing the image of near-offset with the image of far-offset, only raw data was used in the migration. More data pre-conditioning and post-

migration processing will certainly enhance the image. As an example, Figure 4.13 shows another pre-stack depth migration test of the same physical model data after removal of the direct wave and other source generated noises, the image quality was greatly improved.

## CONCLUSIONS

I have developed a new LabVIEW-based physical modeling system. The system is designed through a mix of dedicated motion control board, data acquisition board and serial port. The system includes of signal generation and data acquisition. The acquisition is automated, capable of simulating a general seismic survey or with specialized acquisition geometries. The simple graphic user interface is based on an x, y, z table which controls the transducer movement. The new system also has the capability to do cross-correlation, vertical stack, spectrum analysis, shot gather display, data annotation and transducer position display.

ringing and a strong direct wave contaminate physical modeling data. I have used a mouse pad to degrade direct energy and a chirp source to minimize environmental noise. I have also applied deterministic deconvolution and  $\tau$ -p filtering to improve resolution and to remove linear noises on the collected data. While all these methods may be helpful, none of them can eliminate the ringing perfectly; therefore choosing a wider band, low ringing transducer is recommended in the data acquisition.

I have used a twenty-layer “gradient” model to examine the feasibility of modeling long-offset data. I also acquired data on several simple models to investigate far-offset data. The data show that it is possible to acquire turning wave information from a layered model. I compared my 3D physical model to a 2-D numerical model and found that using physical modeling to model long-offset data is more difficult than numerical modeling.

For long-offset imaging, an accurate initial velocity model is more essential than for near-offset. I have applied a layer-based first arrival tomography method to a 2-D crooked line field data set. The layer-based first arrival tomography is able to obtain a reasonable velocity model for long-offset imaging.

I have also migrated different offset ranges of the physical model dataset using reverse-time pre-stack depth migration. The results show that long-offset image provides improved illumination of vertical boundaries, even though it is noisier and has poorer resolution at the horizontal interfaces. For the interface between water and Plexiglas, which is similar to the property of a salt boundary, the long-offset image has less ringing and is somewhat better defined. I also noticed that the reflectivity at the interface of the Plexiglas is much weaker in the far-offset image, but the interface is better defined at the two sides of the interfaces.

I compared the physical modeling image with a numerical image, and found features of the images are apparently different. In the physical modeling image, the direct energy and ringing effect are strong. There are also evidences of multiple-induced artifacts, such as the flat events inside the Plexiglas, which are stronger in the physical modeling image than in the synthetic seismogram image.

With some pre-conditioning of the raw data, the reverse-time pre-stack depth migration with full-offset data gave a better image result. More pre-conditioning techniques plus some post-migration processing could enhance the image further. A follow-up investigation is recommended.

## REFERENCES

Al-Khalifa, T., and Tsvankin, I., 1995, Velocity analysis for transversely isotropic media: *Geophysics*, **60**, 1550 -1566.

Al-Chalabi, M., 1973, Series approximation in velocity and travelttime computations: *Geophysical Prospecting*, **21**, 783-795.

Berkhout, A. J., 1981, Wave field extrapolation techniques in seismic migration, a tutorial: *Geophysics*, **46**,1638-1656.

Bickel, S. H., 2000, Focusing aspects of the hyperbolic Radon transform: *Geophysics*, **65**, 652–655.

Bishop, T. N., and Bube, K. P., 1985, Tomographic determination of velocity and depth in laterally varying media: *Geophysics*, **50**, 903-923.

Chun, J. H., and Jacewitz, C. A., 1981, Fundamentals of frequency domain migration: *Geophysics*, **46**, 717-733.

Clayton, R. W., and McMechan, G. A., 1981, Inversion of refraction data by wavefield continuation: *Geophysics*, **46**, 860-868.

Dutta, N. C., 2002, Geopressure prediction using seismic data: Current status and the road ahead: *Geophysics*, **67**, 2012–2041.

Fliedner, M. M., and White, R. S., 2001, Seismic structure of basalt flows from surface seismic data, borehole measurements, and synthetic seismogram modeling: *Geophysics*, **66**, 1925-1936.

Gazdag, J., and Sguazzero, P., 1984, Migration of seismic data by phase shifts plus interpolation: *Geophysics*, **49**, 124-131.

Grechka, V., Tsvankin, I., 1997. Inversion of non-hyperbolic moveout in transversely isotropic media: 67th Ann. Internat. Mtg., SEG, Exp. Abstracts, 1686-1688.

Hale D., Hill, N. R., and Stefani, J., 1992, Imaging salt with turning seismic waves: *Geophysics*, **57**, 1453-1462.

Isaac, J. H. and Lawton, D. C., 1999, Image mis-positioning due to dipping TI media: A physical seismic modeling study: *Geophysics*, **64**, 1230–1238.

Jensen J. A., and Svendsen, N. B., 1992, Calculation of pressure fields from arbitrarily shaped, apodized, and excited ultrasound transducers: *IEEE Tran. On Ultrasonics Ferroelectrics and Frequency control*, **39**, 262-267.

Kosloff, D. and Sherwood, J., Koren, Z., Machel, E., and Falkovitz, Y., 1996, Velocity and interface depth determination by tomography of depth migrated gathers: *Geophysics*, **61**, 1511-1523.

Krail, P.M., and Shin, Y., 1990, Deconvolution of a directional marine source: *Geophysics*, **55**, 542-1548.

Matsuoka, T., and Taner, M. T., 2000, Imaging of Refracted Waves by Convolution: 70<sup>th</sup> Ann. Internat Mtg., SEG, Exp. Abstract, 1311-1314.

Nemeth, T., Sun, H., 2000, Separation of signal and coherent noise by migration filtering: *Geophysics*, **65**, 574–583.

Ogilvie, J. F., and Purnell, G. W., 1996, Effects of salt-related mode conversions on subsalt prospecting: *Geophysics*, **61**, 331-348.

Osyov k., 1998, A comparative study between 3-D diving-wave tomography and head wave refraction methods: 68<sup>th</sup> Ann. Internat Mtg., SEG, Exp. Abstract, 1222-1225.

Pasasa, L, Wenzel, F. and Zhao, P., 1998, Pre-stack Kirchhoff depth migration of shallow seismic data: *Geophysics*, **63**, 1241–1247.

Ratcliff, D. W., Gray, S. H., and Whitmore, N. D., 1992, Seismic imaging of salt structures in the Gulf of Mexico: The Leading Edge, **11**, no. 4, 15-31.

Reiter, E. C., Purdy, G. M., and Toksoz, M. N., 1993, 2-D velocity inversion/imaging of large offset seismic data via the tau-p domain: Geophysics, **58**, 1002-1016.

Sabnis, U., and Gardner, G. H. F., 1989, Imaging the flanks of the salt dome: 59th Ann. Internat. Mtg., SEG, Exp. Abstract, 526-529.

Sheriff, R.E., and Geldart, L.P., 1995, Exploration Seismology, Cambridge University Press.

Spitzer, R., Nitsche, F. O., and Green, A. G., 2001, Reducing source-generated noise in shallow seismic data using linear and hyperbolic  $\tau - p$  transformations: Geophysics, **66**, 1612–1621.

Stadtlander, R., and Brown, L., 1997, Turning waves and crustal reflection profiling: Geophysics, **62**, 335–341.

Stoffa, P.L. and Ziolkowski, A., 1983, Seismic source decomposition: Geophysics, **48**, 1-11.

Stolt, R. H., 1978, Migration by Fourier transform, Geophysics, **43**, 23-48.

Stolt, R.H., 2000, Seismic data mapping and reconstruction: *Geophysics*, **67**, 890-908.

Sun, C., Wang, H., and Martinez, R., 2002, Optimizes 6<sup>th</sup> order NMO correction for long-offset seismic data: 72th Ann. Internat. Mtg., SEG, Exp. Abstract, 2313- 2316.

Taner, M. T., and Koehler, F., 1969, Velocity spectra-digital computer derivation and applications of velocity functions: *Geophysics*, **34**, 859–881.

Thomsen, L., 1986, Weak elastic anisotropy: *Geophysics*, **51**, 1954-1966.

Tsvankin, I., and Thomsen, L., 1994, Non-hyperbolic reflection moveout in anisotropic media: *Geophysics*, **59**, 1290-1304.

Versteeg, R. J., 1993, Sensitive of pre-stack depth migration to the velocity model: *Geophysics*, **58**, 873-879.

Wang, C., 1999, Dip moveout in the Radon domain: *Geophysics*, **64**, 278–288.

Wardhana, R., 2001, Analysis of Time-Lapse Seismic Technology Using a Physical Model of Porous Channel Sand, M.S. Thesis, University of Houston.

Yilmaz, O., 1987, *Seismic Data Processing*, SEG, Tulsa.

Youn, O. K., and H. Zhou, 2001, Depth imaging with multiples: *Geophysics*, **66**, 246-255.

Zhang, M., Sekharan, K. K., McDonald, J. A., and Tatham, R. H., 1994, A Physical model experiment for turning ray study: 64<sup>th</sup> Ann. Internat. Mtg., SEG, Exp. Abstract, 1601-1604.

Zhou, H., 1997, Determination of velocities and interfaces by multi-scale tomography, 67th Ann. Internat. Mtg., SEG, Exp. Abstracts, 1877-1880.

Zhou, H., 2003, Deformable layer tomography and application to the Vinton Dome, submitted to SEG, Exp. Abstract.

Zhou, H., Multi-scale tomography for crustal P and S velocities in southern California: PAGEOPH, in press, 2003a.

Zhou, J., and Lines, L. R., 1998, Comparison of Kirchhoff and reverse-time migration methods with applications to pre-stack depth imaging of complex structures: Geophysics, **63**, 1166-1176.

# Appendix A

## AGL NEW LABVIEW-BASED PHYSICAL MODELING SYSTEM

### - USER MANUAL

#### A.1 The 'Start here' panel

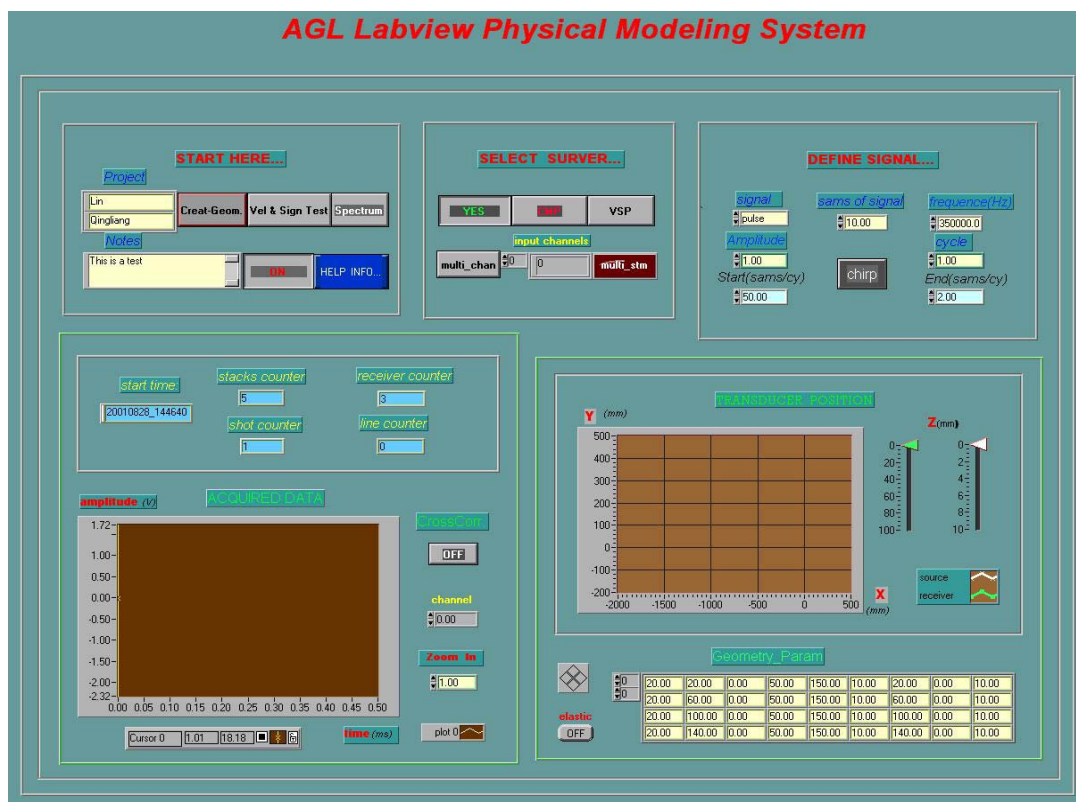


FIG. A.1. Control panel of the main program.

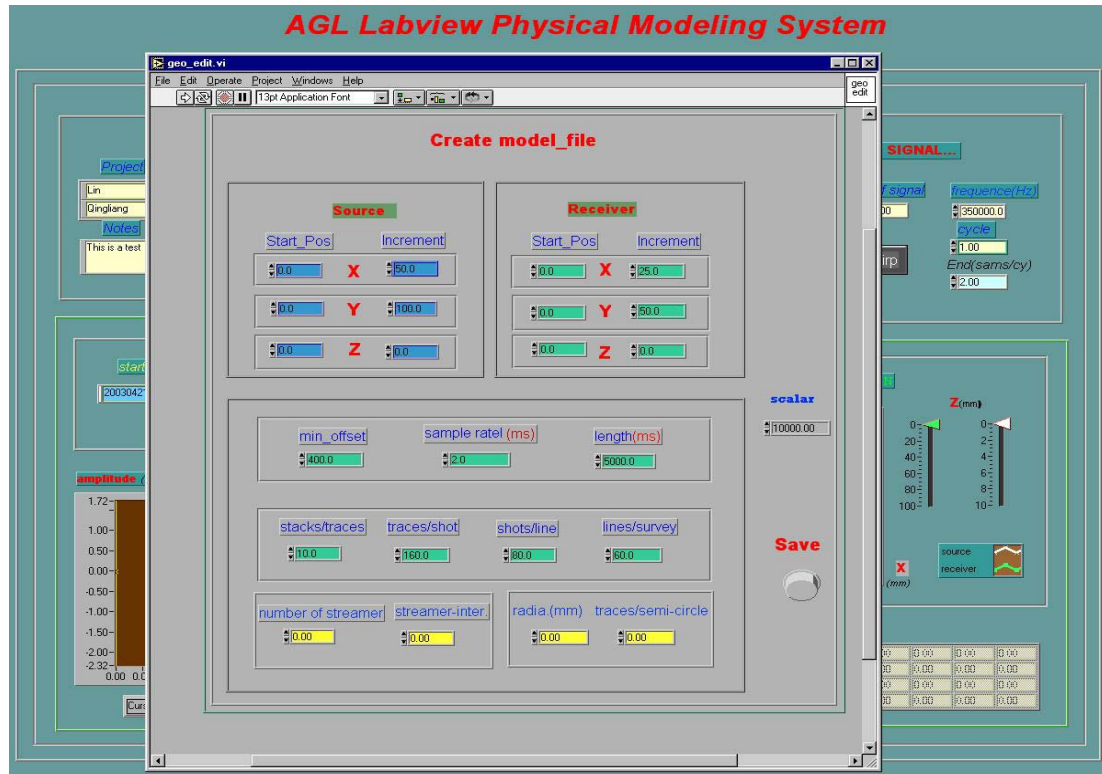


FIG. A.2. Graphic user interface for geometry definition

In the front panel of the main program (Figure A.1), enter the name of the *project* (survey) and some *Notes* to describe the model and data to be collected. If this is a new acquisition, you need to define the geometry to create a model file that controls the modeling operation for later use. Push the *Creat-Geom* Button. When the program executes, a *Create model\_file* window will pop up (Figure A.2) where you can define the origin or a reference point for the source and receiver transducers. You also can

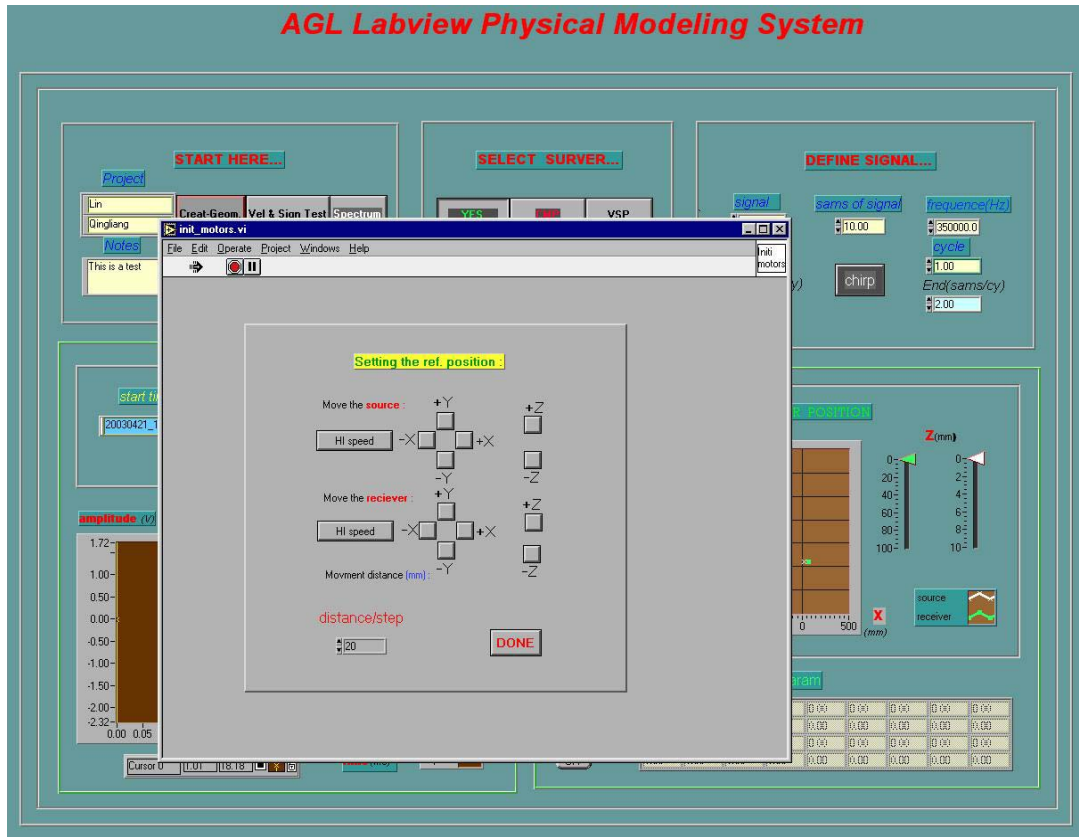


FIG. A.3. After initialization, a panel labeled 'setting ref. position' will pop up. A user then needs to manually set the transducers to a reference position.

define the starting position, source and receiver increment in x, y, z and other acquisition parameters, such as minimum offset, sample rate, the total recording length, the number of vertical stacks per trace, the number of traces per shot, the number of shots per line, the number of lines per survey and the physical model scale. The default scale is 1:10,000 such that 10 cm in the model tank corresponds to 1 km in

the field. Similarly,  $0.4 \mu\text{s}$  in the model tank corresponds to 4 ms in the real world, while a 300 kHz transducer in the model tank corresponds to 30 Hz in the real world. If you are interested in acquiring multi-streamer data, you also need to define the number of streamers and streamer spacing.

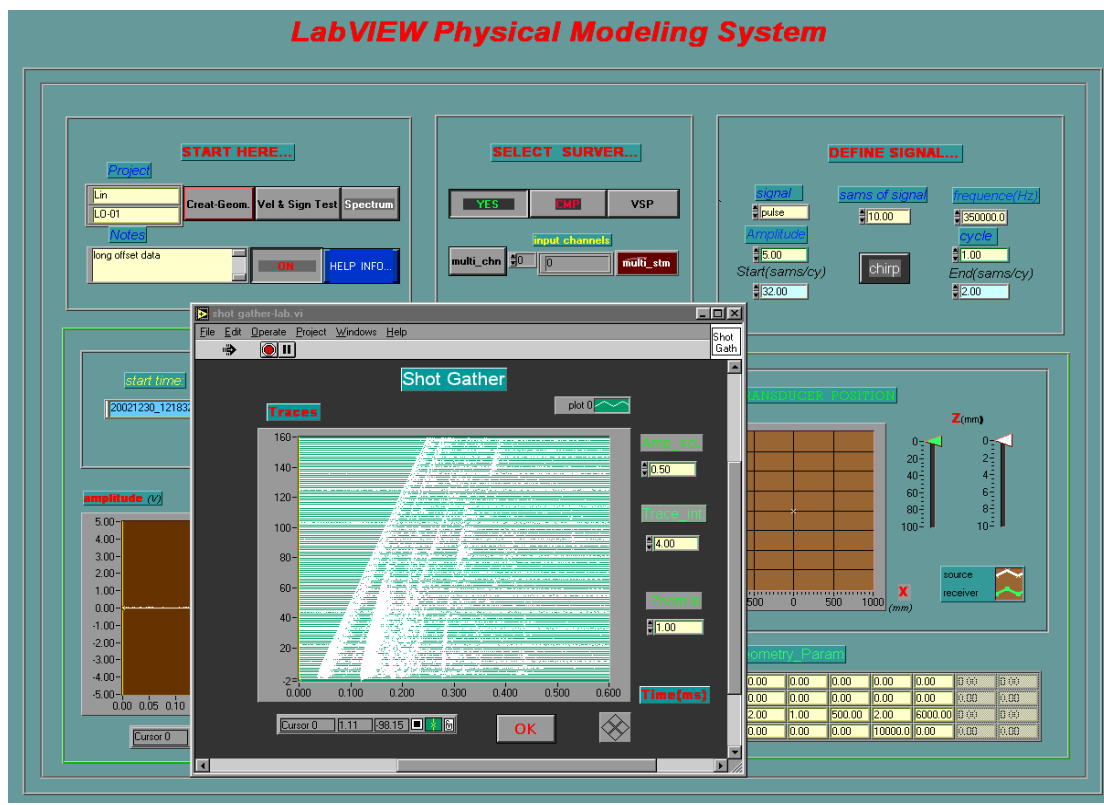


FIG. A.4. Push the 'Gather Display' button. When the gather collection is completed, a gather display window will pop up.

The *Spectrum* button on the control panel is provided for single-trace spectrum analysis and display; the *Gather Display* button is provided to display a gather (Figure A.4). You can also look at the help information (*HELP INFO*. Button) whenever the program is running (Figure A.5).

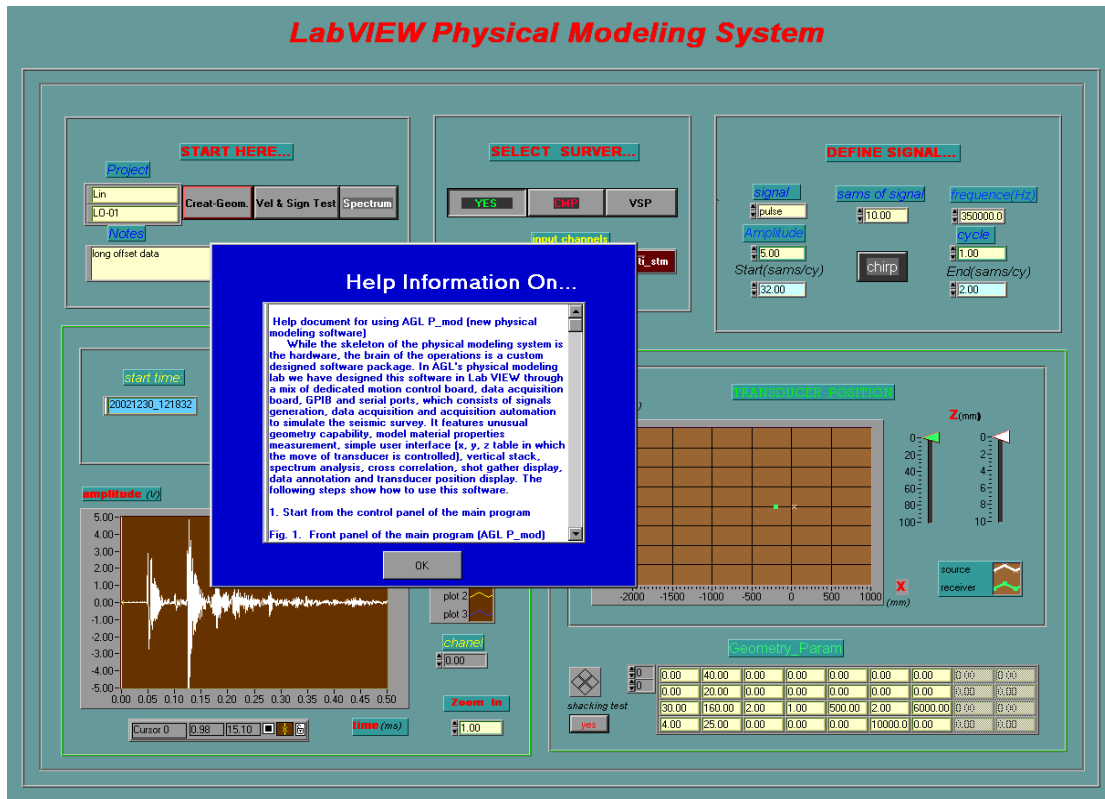


FIG. A.5. Example of the help information.

## A.2 The 'Select survey' panel

Current choices include common-shot, common midpoint (CMP), VSP, single channel simulating multi-streamer and multi-channel (maximum 4 channel) simulating multi-streamer acquisition patterns.

## A.3 The 'Define Signal' panel

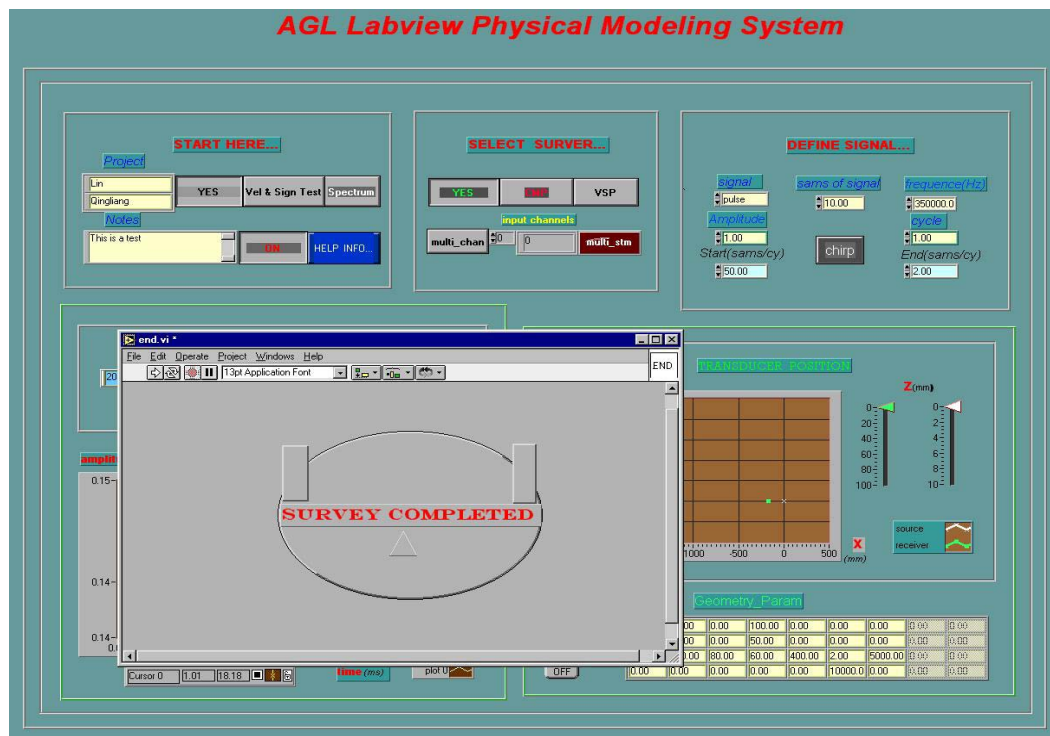


FIG. A.6. Once the survey is completed, the transducers move back to their original positions and a "survey completed" window pops up.

In this panel, the user defines the source signal waveform, amplitude in voltage, frequency in Hz, and the signal length in samples. Currently the system provides pulse, sine, square, triangle, saw tooth and chirp signals with and without attenuation. For the chirp, you need to define the sweep length, the start frequency and end frequency in samples per cycle. The default is an up sweep with a start frequency of 64 samples/cycle, and an ending frequency of 2 samples/cycle. For example, a reference frequency 800 KHz will result in an end frequency of 800 KHz and a start frequency of 50K, which simulate the real word acquisition in 5-80 Hz.

#### **A.4 The modeling operation**

After defining the geometry, survey type and source signature (steps 1, 2 and 3 above), start the modeling operation. It will display the data collection status (including the *start time*, *stacks*, *traces*, *shots* and *lines*) as well as the progress of the transducer movement on an *x - y graph* and a vertical pointer *slide (z)*. The most recent trace will also be displayed. Once the survey is completed, the transducers move back to their original positions and a panel pops up stating that the survey was completed (Figure A.6).

## **A.5 The acquired data**

The acquired data are recorded in SEP format. Each survey has five files: mode file *project.ascii*, history file *project.H*, binary data file *project.H@*, header format file *project.H@@* and binary header file *project.H@@@* are stored under *~/Data/* directory.

## Appendix B

### SOURCE SIGNATURE AND ACOUSTIC FIELD OF PHYSICAL MODELING

In order to understand my physical model data, I need to characterize the wave field generated by ultrasonic transducers.

#### B.1 The transducer

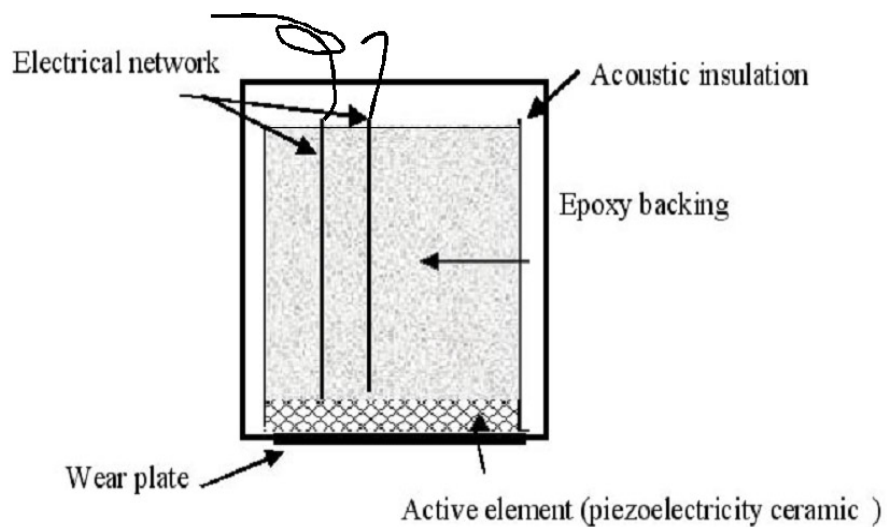


FIG. B.1. Schematic diagram shows the configuration of a contact transducer (Parametrics technical notes).

An ultrasound transducer is composed of an active piezoelectricity ceramic element, some backing material, a wear plate, an electrical network, and acoustic insulation (Figure B.1). The active element is the heart of a transducer and converts electrical energy into ultrasonic energy and vice versa. The backing is a highly attenuative, high-density impedance-matched material that absorbs the energy radiation from the back of the active element. The wear plate of a contact transducer serves as an acoustic transformer between the active element and experimental media such as water or other coupling medium. The central frequency and bandwidth are two important parameters in any data acquisition experiment. The transducer's frequency response depends on the piezoelectric thickness and the backing material. Wider bandwidth results in improved resolution and less ringing.

## **B.2 The signature**

Ultrasound emanated from a piezoelectric transducer is originated from the surface of the piezoelectric element. Since we usually apply a scale of 1:10000 in our physical modeling experiment, a transducer of 1 cm diameter size would correspond to a 100 m diameter spherical source in the real world. For a spherical transducer, the major impact is on source-receiver separation. For a contact transducer, the 'point source' approximation and radiation pattern break down.

Several authors have calculated the spatial impulse response for different shaped transducers by numerical modeling of the pulsed acoustic field distribution in time and space. Based on the Tupholme-Stepanishen method, Jensen and Svendsen (1992) calculated the radiation field by dividing the surface of the transducer into small rectangles and then summing their responses. In simulating a contact transducer, they assumed that the transducer surface is located in an infinite baffle, whose surface moves with a velocity perpendicular to the surface such that the pressure field in front of the transducer can be calculated by summing the component oscillations of the source. In the near field the wave motion (Figure B.2) is approximately that of a plane wave with multiple maxima and minima. The near field distance is a function of the transducer frequency, transducer diameter, and the sound velocity of the coupling material. For regions beyond the near field, the summation of the component oscillations of the source result in approximately spherical radiation outwards, such that the total wavefront has been transformed from planar to spherical.

Many factors influence the pattern of the acoustic field, not all of which can be taken into account analytically. In order to gain a good understanding of the behaviour of a particular transducer it is often necessary to resort to direct measurements. Direct measurements also allow us to verify that the transducers have not been damaged. Measuring the near field and far field wavelets excited by a pulse is also useful for

source deconvolution. In Figure B.3 the spherical transducer was used as both source and receiver in the measurement.

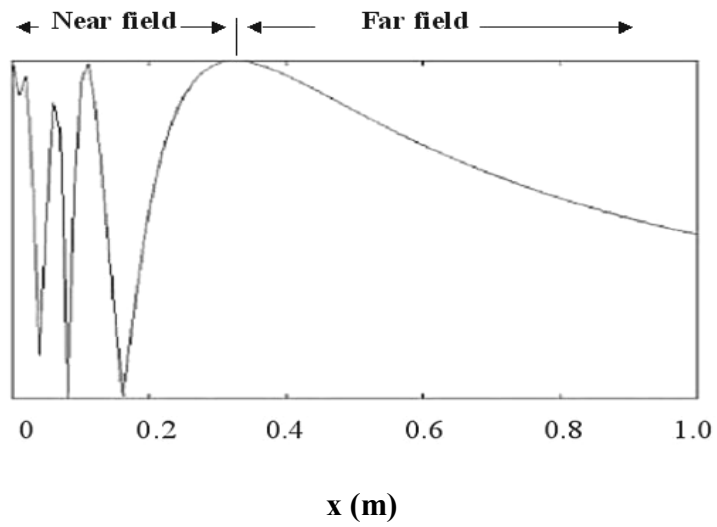


FIG. B.2. The field of a transducer is divided into two zones for a circular transducer of diameter 3 cm. The near field where pronounced interference effects give rise to multiple maxima and minima, and the far field where the total wavefront has been transformed from planar to spherical (Parametrics technical notes).

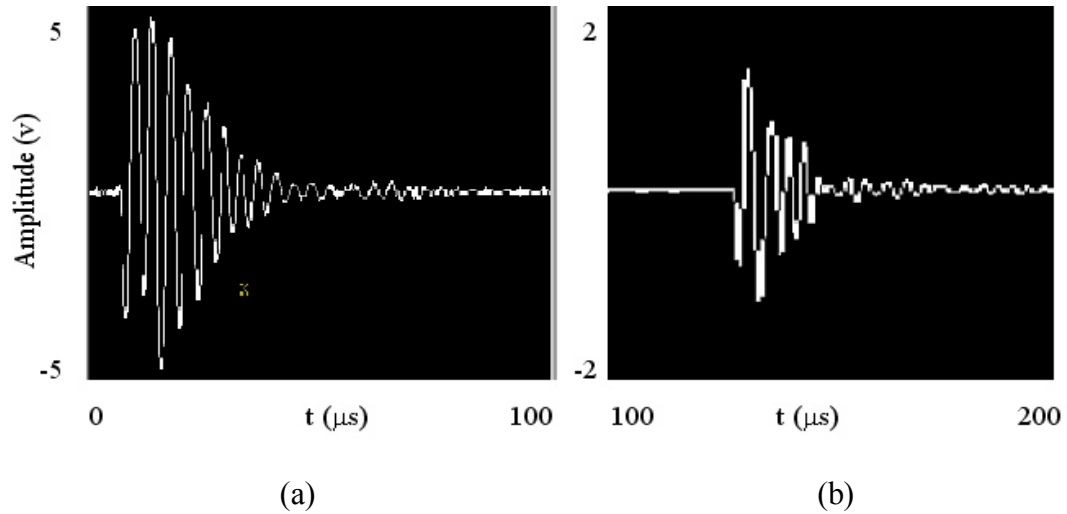


FIG. B.3. Near field wavelet (a), corresponding to source and receiver transducer separation of 1cm; and far field wavelet (b) corresponding to source and receiver transducer separation of 32 cm.

### B.3 Transducers directivity

The radiation of the contract transducer is beamed along the acoustic axis (centerline). Spherical transducers radiate nearly omni-directional signals, but still have some degree of variation. For AVO analysis, it is necessary to calibrarte amplitude as a function of angle from the source. Wardana (2001) provided a detailed description about the radiation pattern for those transducers.

#### B.4 Minimize ambient noise

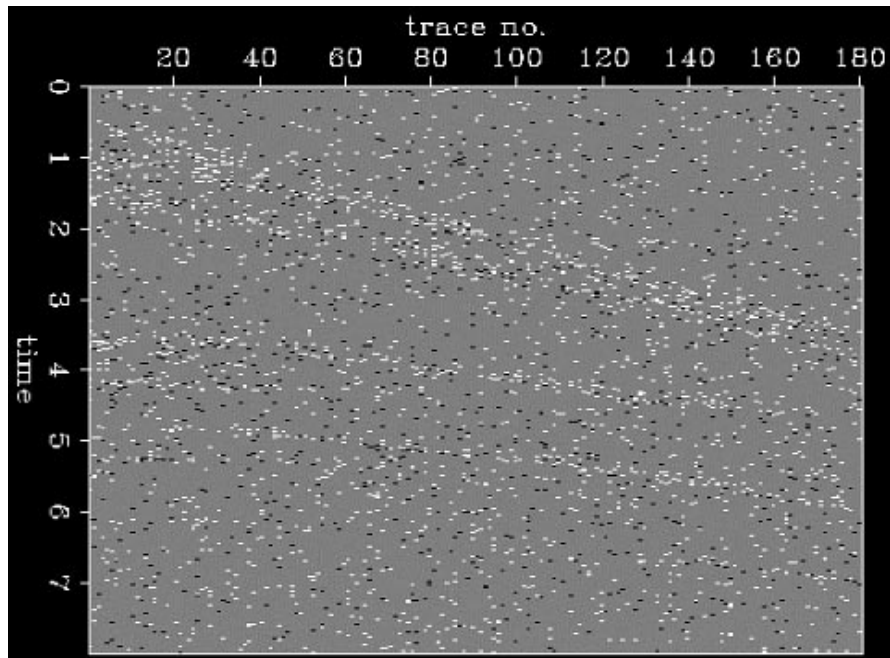


FIG. B.4. A common-shot gather without vertical stack. Signal is immersed in random noise.

Like field data acquisition, noises, especially cultural noises, affect the quality of data acquired. To measure the background noises, I conducted multiple environmental noise measurement at different times of a day and under different conditions. I found

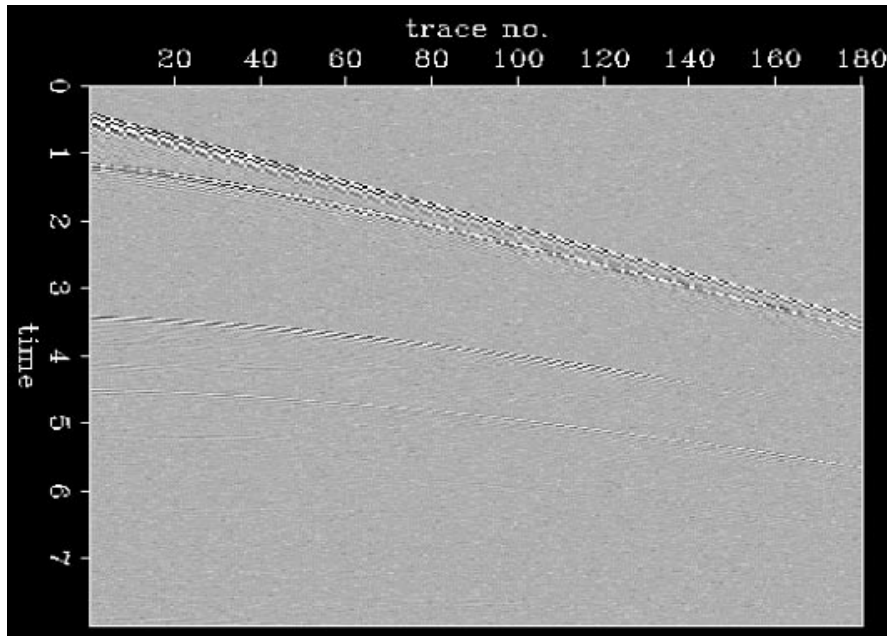


FIG. B.5. A common-shot gather after a vertically stacking of 10 times. The signal to noise ratio is improved.

that significant noise remained even when every source of potential noise inside the Lab (such as filters, air conditioners, etc) was turned off (Figure B.4). The noise is independent of time (morning, noon and evening). Vertical stacking the data helps. Stacking 10 times (Figure B. 5) is a must and stacking 20 times is better to enhance the signal to noise ratio. Since we are working at 300 KHz, I suspect the major noise comes from the electronic sources in the building.

## Appendix C

### METHODS TO IMPROVE DATA ACQUISITION QUALITY

#### C.1 'Mouse pad' to degrade the direct energy

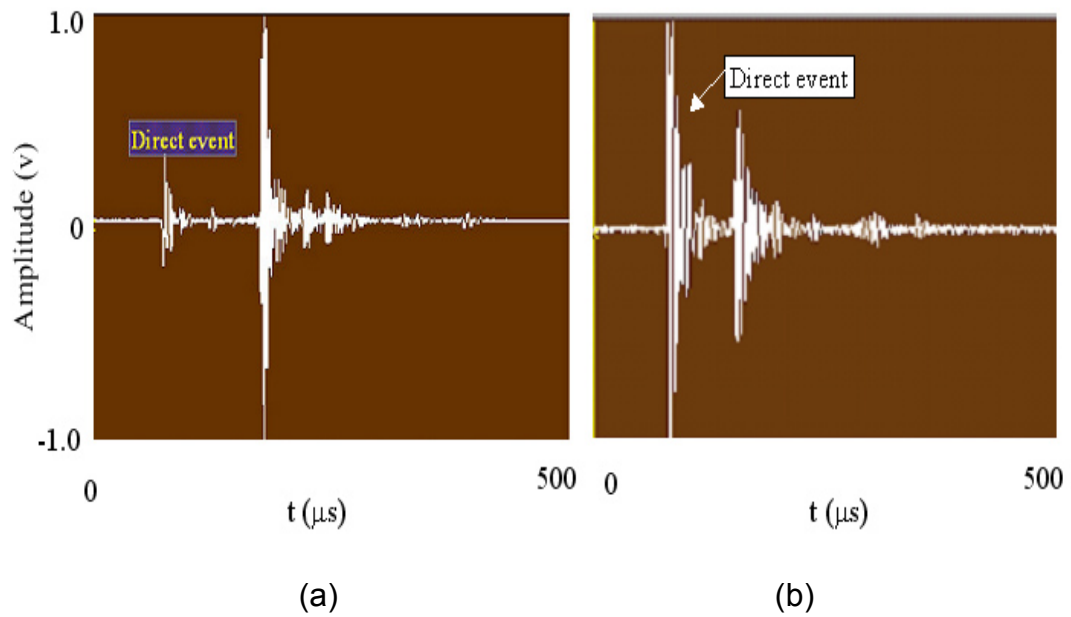


FIG. C.1. Signal measured (a) with and (b) without a mouse pad. The direct energy (Direct event) has been suppressed in (a).

To minimize the high amplitude direct arrival, I constructed a cone shape acoustic 'sponge' out of a rubber computer mouse pad. The shot gather collected by applying this method is shown in Figures C.1 (a). The direct energy (first event) has been suppressed. More energy was degraded in the near-offset than in the far-offset.

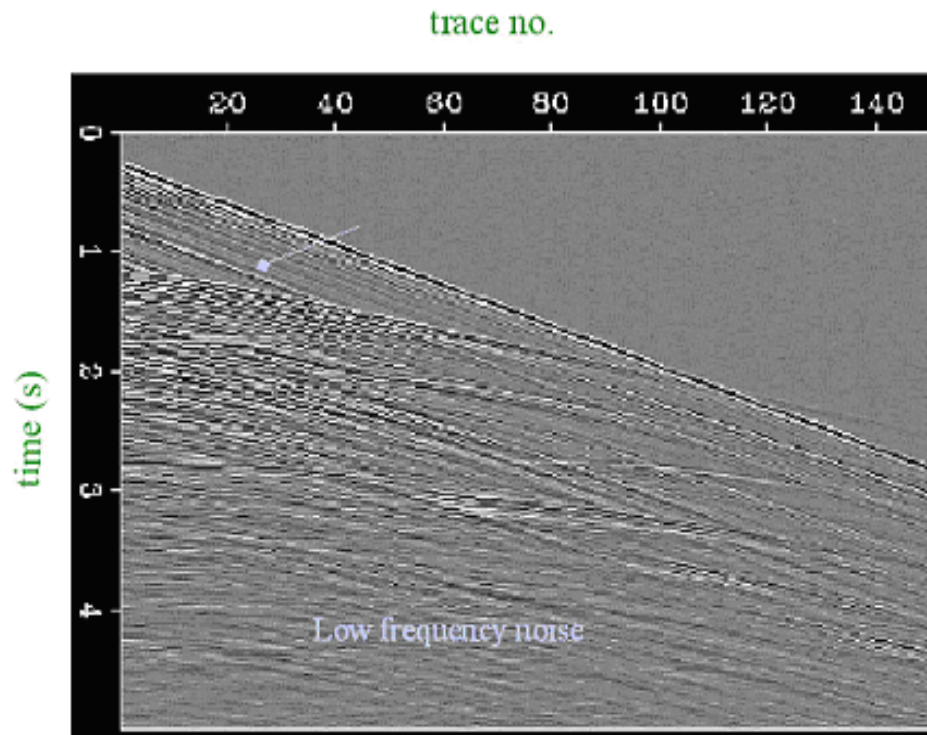


FIG. C.2. Mouse pad also creates artifacts while it degrading near-offset direct arrival energy.

Note that while the mouse pad attenuates the direct wave, it creates artifacts such as indicated by the arrow shown in Figure C.2. There also appears to be more low frequency background noise.

## C.2 Effect of source depth on spherical transducer

The source transducer was deployed close to the surface of the water (Figure C.3), assuming the transducers act as a point source that emits an omni-directional field. The upward travel energy is reflected at the free surface and forms a down going ghost. Since the reflection coefficient is nearly 1 at the free surface, the ghost's amplitude is nearly equal to the direct wave but with a delay. While one might think

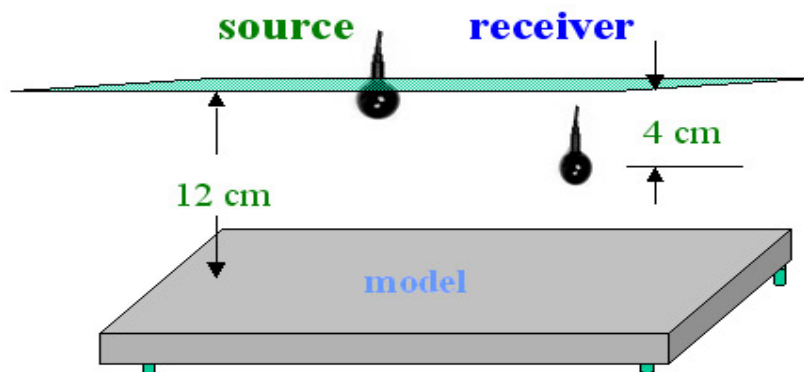


FIG. C.3. Setup for the acquisition shown in Figure C.4 and C.5.

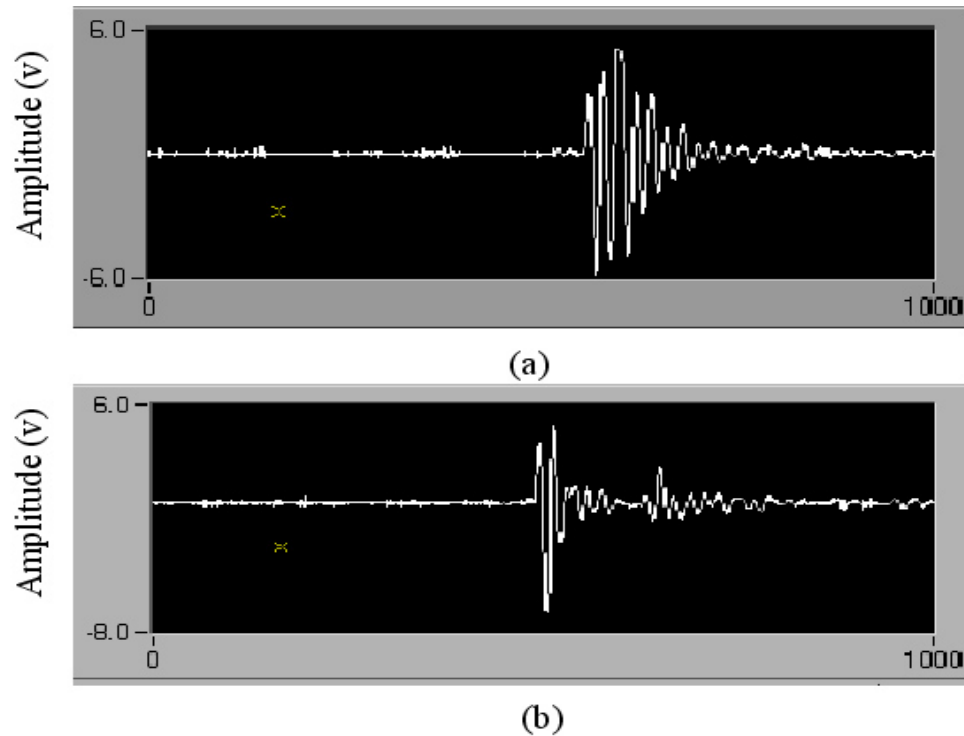


FIG. C.4. Source generated wave field with the transducer center placed at (a) 0 cm and (b) 4 cm below the surface. The transducer rings if it is not totally submerged.

that a shallow source might be modeled by placing the transducer's center at the surface, the lack of impedance matching above the water causes excessive ringing (Figure C.4, a). In contrast, since a compact transducer (or small pinduces) is backed by tungsten-doped epoxy, its wavelet is unaffected by the water depth. Figure C.5 shows a common-shot gather collected with the source was deployed at the depth of 4 cm, the ghosts as the arrow indicated is obvious.

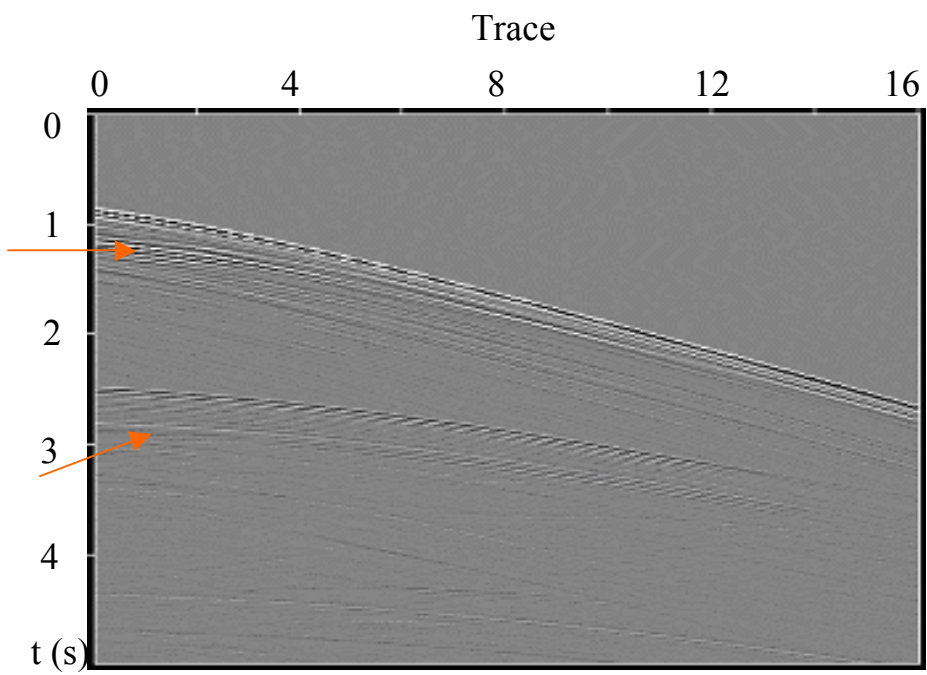


FIG. C.5. Common-shot gather collected with source depth of 4 cm. Arrows indicate source ghosts.